NTNU – Trondheim
Norwegian University of
Science and Technology

Hydrogen induced stress cracking of alloy 718

Effects of chemical composition and microstructure

Adrian Christian Haaland

Materials Science and Engineering
Submission date: June 2014
Supervisor: Roy Johnsen, IPM

Norwegian University of Science and Technology
Department of Engineering Design and Materials

Preface

This master thesis is submitted to the Norwegian University of Science and Technology as a requirement for the Master's degree program Material Technology at the institute of Material Science and Technology. This project has been a collaboration between NTNU, and ATI Metals who has financed this Master and supplied the Inconel-718 alloys tested. Professor Roy Johnsen has supervised the work presented in this master together with co-supervisor Postdoc Afrooz Barnoush at NTNU.

I would like to express my gratitude towards my supervisors for guiding me through my work. Professor Roy Johnsen has shared his competence and contributed to fruitful discussions, which have been a valuable input and guided me through my work. I would also like to thank Afrooz Barnoush for his input and help in planning and designing the experimental setups used in this master project. Furthermore, PhD. Jim Stian Olsen and Krista Amato have provided guidance in the project work preceding this master thesis, on which the tests in this master thesis were largely based on. I would also like to thank Ann Karin Kvernbråten at SINTEF for performing the hydrogen melt extraction analysis presented in this work. Last but not least, I would like to thank ATI Metals for the financial funding and for supplying the materials tested in this master thesis. Without them, none of the work presented would have been possible.

Decleration

I hereby declare that the work presented in this project is a result of my own individual work and in compliance with NTNU's rules and regulations.

Adrian Christian Haaland

June 13, 2014

Abstract

This master thesis have examined the effect of variations in composition and microstructure on the HISC susceptibility of Inconel-718. 6 different Inconel-718 variants with different compositions and heat treatments were examined. Tensile samples were pre-charged with hydrogen at $120°C$ in an $H_3PO_4/Glycerol$ electrolyte for 5 days, and subsequently subjected to stepwise constant-load tensile tests. The tensile tests were performed in synthetic saltwater with a negative polarization of -1050mA Ag/AgCl, corresponding to a galvanic coupling with aluminium or zinc in seawater. Hydrogen free samples were tested in air for comparison. An optical microscope was used to examine the sample surfaces during testing. Fracture surfaces were examined in SEM, and the samples were also examined for secondary cracks. All the Inconel-718 samples pre-charged with hydrogen showed a significant reduction in ductility and contained Inter Granular (IG) areas on the fracture surfaces. A decrease in fracture strength of approx. 5-10% of Yield Strength (YS) was seen in all the variants examined, but no significant trend between the Inconel-718 variants was detected here. Smaller grain sizes were correlated with an increasing ductility loss measured by loss of Reduction of Area (RA) and loss of Elongation (ϵ) prior to fracture. This was attributed to increased Grain Boundary (GB) diffusion of hydrogen during pre-charging, resulting from more GBs. A Hydrogen melt extraction analysis done by SINTEF confirmed the elevated hydrogen levels expected in these fine-grained Inconel-718 variants.

Sammendrag

Denne masteroppgaven har undersøkt effekten av sammensetning og mikrostruktur på graden av hydrogensprøhet i Inconel-718. 6 forskjellige varianter av Inconel-718 har blitt undersøkt i denne oppgaven. Strekkprøver ble for-ladet med hydrogen i en $H_3PO_4/Glycerol$ blanding ved 120°C i 5 dager, og ble deretter tested i syntetisk saltvann ved et negativt potensial på -1050mV Ag/AgCl, som tilsvarer en galvanisk kobling med aluminium eller sink i sjøvann. Testene ble gjort ihht. en stegvis konstant spenning test. Prøver uten hydrogen ble testet i luft og brukt som sammenlikning. Et lysmikroskop ble brukt til å observere prøveoverflatene under testing. Bruddflatene ble undersøkt i SEM, og prøveoverflatene ble undersøkt for sekundærsprekker. Alle Inconel-718 variantene som var for-ladet med hydrogen viste en tydelig reduksjon i duktilitet, og inneholdt områder av Intergranulært brudd på bruddflaten. En reduksjon i bruddstyrke på 5-10% ble observert i alle variantene, men ingen significant sammenheng med mikrostruktur eller sammensetning ble observert her. Det ble observert at duktilitetstapet målt som tap av Reduction of Area (RA) og Elongation (ϵ), økte med minkende kornstørrelse. Årsaken til dette antaes å være at Inconel-718 variantene med liten kornstørrelse hadde en større grad av korngrense diffusjon under for-ladingen, som følge av økt korngrenseareal. Dette ble bekreftet av smelte-ekstraksjon analysene gjort av SINTEF, som viste et høyere hydrogen innhold i prøvene med mindre kornstørrelse.

Contents

1 List of abbreviations and symbols

- A_{after} - Fracture area after testing
- A_{before} - Cross section area before tensile testing
- $Ag/AgCl$ - Silver/Silver Chloride reference electrode
- b - Tafel's slope
- BCC - Body Centered Cubic crystal structure
- CC - Cathodic Current
- CP - Cathodic Protection
- D - Grain Diameter
- $\overline{D}$ - Average grain size
- D_H - Steady state diffusivity of hydrogen in Inconel-718
- D_H^{highT} - High temperature diffusivity of hydrogen in Inconel-718
- D_H^{lowT} - Low temperature diffusivity of hydrogen in Inconel-718
- E - Electric potential
- $E_{Coupling}$ - The coupling potential of two dissimilar metals in galvanic contact
- E_{rev} - Reversible potential for an electrochemical half cell reaction
- ESR - Electro Slag Remelting
- FCC - Face Centered Cubic crystal structure
- FEM - Finite Element Method
- f_{GI} - Fraction of Grain Interior
- f_{GB} - Fraction of Grain Boundary area
- G - ASTM Grain size number

- GB - Grain Boundary
- HELP - Hydrogen Enhanced Localized Plasticity
- $Hg/HgSO_4$ - Mercury/Mercury Sulphate reference electrode
- HIP - Hot Isostatically Pressed
- HISC - Hydrogen Induced Atress Cracking
- HT/HP - High Temperature, High Pressure
- i - Current density
- i_0 - Exchange current density
- i_{corr} - Corrosion current density
- IG - Inter granular
- K_{Ic} - Fracture toughness
- K_{Ic}^0 - Fracture toughness of a single crystal
- K_{Ic}^{GI} - Local fracture toughness in the grain interior
- K_{Ic}^{GB} - Local fracture toughness in the grain boundary area
- LEFM - Linear Elastic Fracture Mechanics
- MVC - Micro Void Coalescence
- N_{ASTM} - Number of grains counted per square inch at 100x magnification
- $N_{Borderline}$ - Number of grains at the borderline of the area examined
- N_{Inside} - Number of grains inside the area examined
- OM - Optical Microscope
- PC - Poly Carbonate
- R - Universal gas constant
- RA - Reduction of Area

- RA_0 - Reduction of Area without hydrogen
- RA_H - Reduction of Area with hydrogen
- RA_{Loss} - Loss of Reduction of Area as a result of hydrogen
- SD - Standard Deviation
- SDSS - Super Duplex Stainless Steel
- SEM - Scanning Electron Microscope
- SSRT - Slow Strain Rate Test
- t^{highT} - High temperature diffusion time
- t^{lowT} - Low temperature diffusion time
- t_{GB} - Thickness of Grain Boundary zone
- T- Temperature
- TT - Transition Temperature
- TMP - Thermomechanical Processing
- UTS - Ultimate Tensile Strength
- VIM - Vacuum Induction Melting
- VAR - Vacuum Arc Remelting
- YS - Yield Strength
- ϵ - Elongation
- ϵ_0 - Elongation without hydrogen
- $\epsilon_{Eng.}$ - Engineering strain
- ϵ_H - Elongation with hydrogen
- ϵ_{Loss} - Loss of elongation as a result of hydrogen
- ϵ_{Max} - Maximum elongation of the load cell

- ϵ_{True} - True strain
- σ - Tensile stress
- $\sigma_{Eng.}$ - Engineering stress
- σ_f - Fracture stress
- σ_{True} - True stress

2 Background and inspiration for this Master thesis

2.1 Inconel-718 in the Oil and Gas industry

In the oil and gas industry, the Inconel-718 alloy is used extensively because of its superior mechanical properties and resistance to H_2S. The alloy is not considered resistant to corrosion in seawater and will need Cathodic Protection (CP). Today, Inconel-718 is tested against Hydrogen Induced Stress Cracking (HISC) and Sulphur Stress Cracking (SSC) according to B.8 in ISO 15156-3 [9]: Samples are coupled to carbon steel to achieve CP, and tested with 1 bar H_2S in NACE solution-A [28]. Samples are then loaded to the desired stress level and tested for 1 month. A minimum of 3 samples must be tested. If a sample does not fracture and the surface is free of cracks, then the sample has passed the test. If all three samples pass, the alloy is considered safe for use. Precipitation-hardened nickel alloys like Inconel-718 are also required to follow a specific heat treatment, in order to obtain the desired amount of precipitation hardening. The alloys hardness is tested, and in order to be used in Oil and Gas applications, a hardness below 35 Rockwell is required. This is done to avoid components with excessive precipitation, which is correlated with reduced ductility and increased HISC susceptibility [11, 35, 36, 59].

Despite the effectiveness of these tests, they don't account for the absorption of hydrogen which can take place during years of service, especially in High Temperature High Pressure (HT/HP) conditions. The possibility still exist that hydrogen gradually diffuses into the alloy during years of service. Previous studies have investigated the effect of hydrogen in Inconel-718 [12, 16, 23, 25, 35, 45], and they suggest that hydrogen is indeed able to cause a reduction in ductility and crack growth resistance when the concentration is high enough. Until recently, the slow hydrogen diffusion and the high inherent ductility in FCC materials have resulted in the assumption that Inconel-718 is immune to HISC. Austenitic nickel alloys like Inconel-718 are indeed much more resistant to HISC compared with their ferritic

stainless steel alternatives, in which hydrogen diffuses much faster. At shorter time frames (months), Inconel-718 would therefore appear to be immune to HISC. Recent failures [8] have now put this assumption into question, and lead to extensive research by the industry, with the goal of achieving a better understanding of the HISC properties in nickel-based superalloys. Although it has now become clear that Inconel-718 can be susceptible to HISC given enough hydrogen and time, there still exists a number of production routes and heat treatments available for producing this alloy [18, 20, 21, 39, 50]. The variations in impurity contents, inclusions, grain size and precipitate distributions resulting from production and heat-treatment, can potentially have a large effect on the HISC susceptibility. The aim of this master thesis is therefore to examine the effect of variations in chemical composition and microstructure (grain size and δ-particles) on the HISC susceptibility of Inconel-718.

2.2 Previous work and inspiration for this master thesis

The experiments performed in this master thesis builds upon the project work preceding this master thesis, and inspiration from previous research [30, 33, 41] examining the HISC properties of Super Duplex Stainless Steel (SDSS). One of the key inspirations here was the work done by Johnsen et. al [33], demonstrating the use of a step-wise constant load test for determining the critical HISC stress in SDSS. In a step-wise constant load test, a tensile sample subjected to CP is loaded to an initial stress, and the stress level is subsequently increased every day until fracture occurs. Johnsen et al. demonstrated that the step-wise constant load test resulted in the same fracture stress as the test where the sample was loaded directly to the final stress level.

The tensile test setup utilized in this master thesis was inspired by the results and experience gained from the preceding project work. In this project, the reduction in fracture strength in Inconel-718 as a result of hydrogen was examined. Samples were pre-charged in synthetic saltwater at $80°C$ at a potential of -1050 mV Ag/AgCl and subsequently subjected to tensile tests at room temperature in synthetic saltwater at -1050mV Ag/AgCl. It was shown that the reduction in fracture strength increased with the number of days of pre-charging, where the longest pre-charging period was 10 days. All the samples tested nevertheless fractured well above Yield Strength (YS), with the lowest fracture at 124% of YS. The high fracture strengths resulting fro these tests formed the basis for some of the starting stresses chosen for the step-wise constant load tests performed in this master thesis.

3 Background theory

3.1 Microstructure and properties of Inconel-718

Inconel-718 is part of a class of nickel superalloys characterized as precipitation hardened alloys. These alloys were originally developed for use in turbine engines and aerospace technology due to their high temperature creep resistance, high strength and good ductility. Being a precipitation hardened alloy, Inconel-718 achieves its superior mechanical properties through the fine γ' and γ'' precipitates. The precipitation of these particles depends on the composition (the Al + Ti/Nb ratio), but generally occurs in the 650 - 900$°C$ range. A Temperature Transformation Time (TTT) diagram [46] is displayed in figure 1, showing the isothermal precipitation times and temperatures for γ', γ'' and δ-particles in a wrought Inconel-718 alloy.

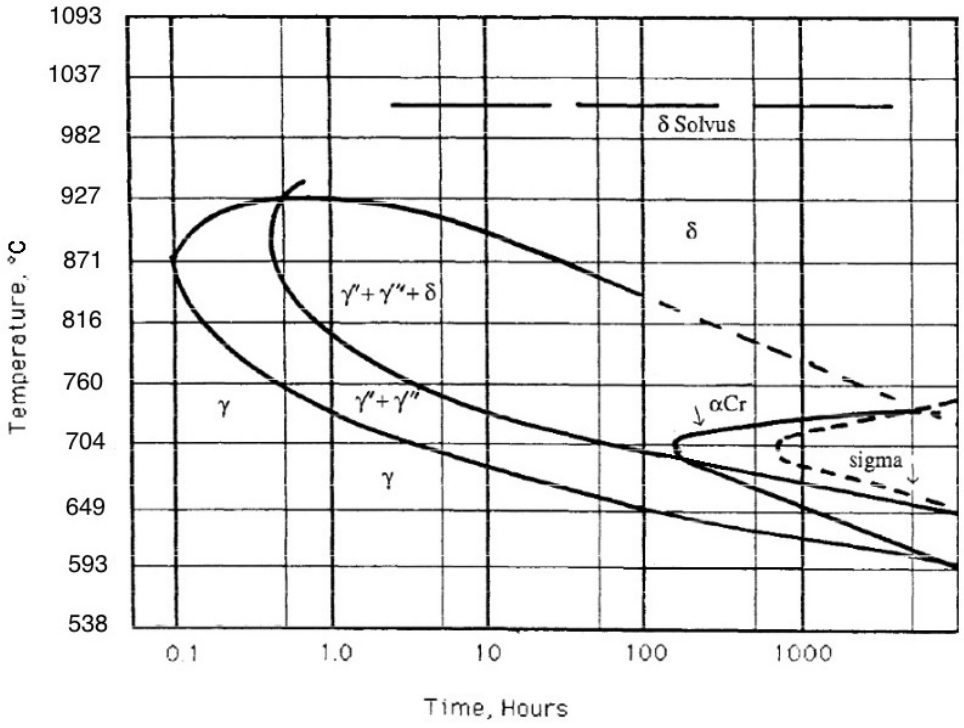

Figure 1: A TTT diagram from the article: "A current T-T-T diagram for wrought alloy 718" by A. Oradei [46]. The temperature denomination has been changed from $°F$ to $°C$, hence the odd y-axis numeration.

The γ' phase has the composition $Ni_3(Ti, Al)$ and a $L1_2$ crystal structure. These particle form as nano sized pseudo-spherical precipitates, which are coherent with the γ-matrix. The γ'' phase has the composition Ni_3Nb and a DO_{22} crystal structure. This phase also forms as nano-sized precipitates and has a coherency to the γ-matrix along two of its three principle axis. The slight misalignment along the c-axis causes the γ''-phase to precipitate as disk-shaped particles in order to minimize the larger surface energy along the c-axis. Both particles have a precipitation hardening effect, but γ'' is the dominant strengthening particle as it occupies a much larger volume faction than γ' in Inconel-718 [51]. A picture is included in figure 2 from the characterizations of Inconel-718 done by C. Slama [51]. This pictures show a TEM image obtained from a thin Inconel-718 foil, showing the disk shaped γ''-precipitates (Black) and the small pseudo-spherical γ'-precipitates (White) in the γ-matrix (Grey). After excessive ageing at 750-850$^\circ C$, or if heat treatment is performed in directly in the 900-1000$^\circ C$ range, δ-phase will start to form at the expense of γ''-particles. Both γ'' and δ have the composition Ni_3Nb. The δ phase has a orthorhombic crystal structure and is incoherent with the γ-matrix. If not controlled, the δ-particles will therefore tend to precipitate at grain boundaries (GBs), which has a detrimental effect on the mechanical properties. Through precipitation hardening, the Inconel-718 alloy is able to maintain its high yield strength (>800Mpa) and creep resistance up to temperatures as high as 650$^\circ C$. Being an austenitic alloy with many crystallographic slip systems, Inconel-718 also exhibits a large degree of ductility, with elongations prior to fracture in the range of 20-50%. These superior properties explains why Inconel-718 was originally developed and used in critical high temperature engine parts. Because its high nickel and chromium content, the Inconel-718 alloy also has a good corrosion resistance, particularly in H_2S containing environments. The combination of superior mechanical properties and good corrosion properties has resulted in use of Inconel-718 by the Oil and Gas industry for critical components exposed to harsh environments, such as low pH H_2S environments known as sour service and HT/HP conditions. The use of Inconel-718 is nevertheless limited by its high production cost.

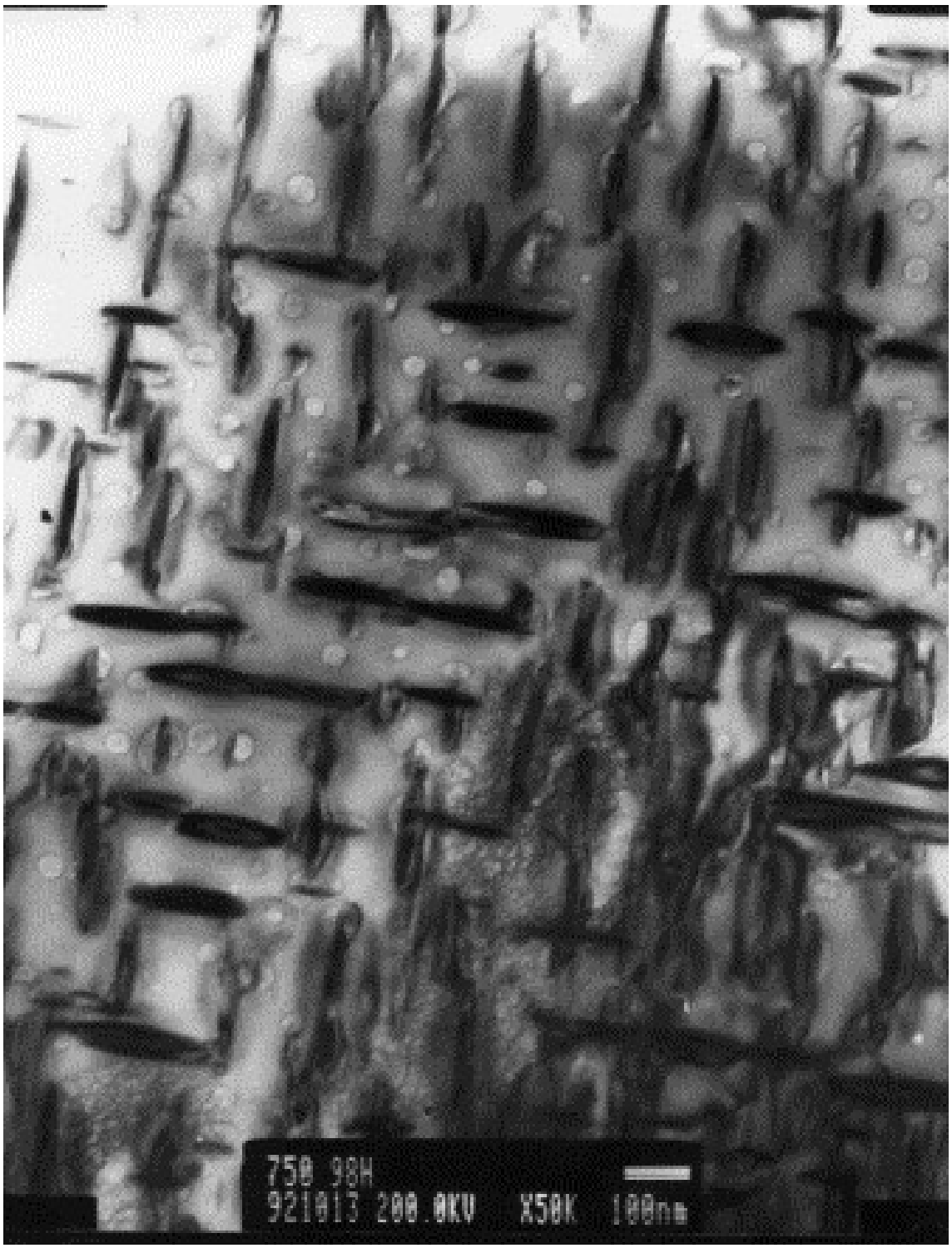

Figure 2: A TEM image from the article: "Structural characterization of aged inconel 718" by C. Slama [51]. The image shows the different precipitates formed in Inconel-718 during aging: γ' (White), γ'' (Black) and the γ-matrix (Grey background). The γ'' phase tends to nucleate at previous γ' particles.

3.2 An introduction to the production of Inconel-718

Inconel-718 is commonly melted using Vacuum Induction Melting (VIM), and cast as thick cylinders known as electrodes. These electrodes are then remelted using Vacuum Induction Remelting (VAR) or Electro Slag Remelting (ESR) [50]. The remelting step can be repeated 1 or more times, depending on the purity desired and the acceptable cost. The purpose of these remelting steps is to remove inclusions and to minimise the content of C, N, O and S, which have a negative effect on the mechanical properties [32]. The remelting steps also aims to reduce the amount of segregations (primarily Nb). These production techniques are size limited [39]. The combination of expensive alloying elements (Ni, Cr, Nb, Mo) and limited sizeability, makes Inconel-718 an expensive alloy to produce, and explains why the use of Inconel-718 is limited to special applications where other materials do not qualify.

After remelting, the Inconel-718 alloy follows a homogenization treatment. The homogenization temperature is set slightly below the eutectic melting point which, depending on the exact composition lies around $1200°C$. Homogenization reduces Nb segregations and redissolves the eutectic Laves phase, which is a brittle intermetallic phase that forms during solidification. The Laves phase has a hexagonal crystal structure and the composition $(Ni, Fe, Cr)_2(Nb, Mo, Ti)$, which is commonly simplified as Ni_2Nb because of the high Nb content in this phase. This phase reduces the ductility and impact toughness of Inconel-718, by acting as a preferred crack-propagation path along the GBs [7]. If the carbon concentration is not kept low, MC-carbides will also form during solidification. Course MC-particles are not easily removed by the homogenization treatment, which is one of the reasons why a low C concentration level is desired.

After homogenization the grain structure is often very course, which is not desirable with respect to strength and fracture toughness. This is improved during the subsequent Thermo Mechanical Processing (TMP). For Inconel-718 this process is also called δ-processing [2, 17, 20, 29, 34]. In this process the alloy is kept below the δ solvus-temperature during hot rolling, which causes large amounts of acilcular δ-particles to precipitate from the highly deformed microstructure. The continuously applied deformation causes these particles to break up, into smaller more globular-shaped particles. When the deformed microstructure starts to recrystallize, these globular δ-particles act as GB pinners, reducing grain growth through Zener drag [40]. This retards grain growth and result in a fine grain structure. The process requires strict control on deformation rate, temperature and time, in order to work as intended [20]. To little/late or to much/early δ-precipitation will result in inadequate GB pinning or depletion of Nb, respectively. The process can nevertheless be very effective in achieving small grain sizes. Recently, a modified versions of δ-processing have been developed and tested, resulting in extremely small, even nano sized grains in Inconel-718 [19, 34].

Fine grain sizes can also be produced through Hot Isostatical Pressing (HIP). In this production process, a fine metal powder is pressed together at an elevated temperature, yielding a fully dense material. The ability to produce complex geometries with a fine grain size and without δ-particles is a great advantage with respect to HISC, as these particles have been correlated with an increased ductility loss when hydrogen is present [11].

3.3 The effect of grain size on mechanical properties

It has long been known that the yield strength of a polycrystalline alloy can be increased by grain refinement. Hall [22] and Petch [44] simultaneously discovered that the yield strengths of polycrystalline alloys increased proportionately with $D^{-\frac{1}{2}}$, with D being the grain diameter. This relationship is known as the Hall-Petch effect.

A relationship between fracture toughness and grain size exists as well. Fan [13] examined several polycrystalline systems and found that the fracture toughness could be expressed as $K_{Ic} = K_{Ic}^0 + k_f \cdot D^{-1}$. An interesting theory was proposed in order to derive this expression, playing on the different dislocation behaviours in low and high stacking fault energy materials: Dislocations in the low stacking fault alloys like Cu ($40mJ/m^2$) and Cu-25at.%Zn ($7mJ/m^2$) dissociate readily, which results in wedge shaped dislocation pile-ups at the GBs. The stress fields exerted by these dislocations act as strong barriers for further dislocation movements along the original slip plane. This results is a more heterogeneous plastic deformation across the grains, which enhances the Micro Void Coalescence (MVC) [55] failure mechanism. The GB areas in low stacking fault material can therefore be regarded as having a locally lower fracture toughness K_{Ic}^{IG}, relative to the grain interior. The opposite is true for high stacking fault energy materials like Al ($200mJ/m^2$) and Ni ($150mJ/m^2$). These materials are not expected to have the same barriers against dislocation motion, and a more uniform plastic deformation occurs. As the GBs represents obstacle for dislocations which require extra energy to be overcome (for example through cross slip), the local fracture toughness in the GB area is higher, relative to the grain interior.

Fan [13] expressed the Fracture toughness of an alloy (K_{Ic}) as a linear, volume-fraction weighted sum of the grain interior fracture toughness (K_{Ic}^{GI}) and the GB fracture toughness (K_{Ic}^{GB}). The expression is shown in equation 1:

$$K_{Ic} = f_{GI} \cdot K_{Ic}^{GI} + f_{GB} \cdot K_{Ic}^{GB} \tag{1}$$

.

In this equation, f_{GI} and f_{GB} are the fractions of grain interior and GB area respectively. By approximating the volume-fraction of GB zone as $f_{GB} = \frac{2 \cdot t_{GB}}{D}$, where t_{GB} is the the GB zone thickness and D is the grain size, the previous expression becomes:

$$K_{Ic} = \frac{2t_{GB}}{D} \cdot K_{Ic}^{GB} + (1 - \frac{2t_{GB}}{D}) \cdot K_{Ic}^{GI} \tag{2}$$

Equation 2 can then be further simplified by substituting $k_f = 2t_{GB} \cdot (K_{Ic}^{GB} - K_{Ic}^{GI})$ and $K_{Ic}^{0} = K_{Ic}^{GI}$. Here, K_{Ic}^{0} is the fracture toughness of a single crystal and k_f will be a material constant. The result is shown in equation 3:

$$K_{Ic} = K_{Ic}^{0} + k_f \cdot D^{-1} \tag{3}$$

This derivation also gives meaning to the D^{-1} relationship observed by Fan [13]. The physical meaning of the coefficient k_f as the difference between the fracture toughness of the GB area relative to the grain interior means that alloys with positive k_f exhibit GB toughening as the grains get finer, while the alloys with negative k_f exhibit GB embrittlement as the grains get finer. Indeed, the high stacking fault materials examined by Fan [13] showed an increase in fracture toughness with decreasing grain size, while the low stacking fault materials showed a decrease in fracture toughness with decreasing grain size.

Because of the large amount of alloying elements present in Inconel-718, the stacking fault energy will be substantially lower than in pure nickel. The exact value is not known, but estimates based on the alloying elements present range from 50 to $75 mJ/m^2$ [15, 53]. The alloy therefore falls somewhere in between compared with

the alloys examined by Fan [13]. Whether the fracture toughness increases with finer grains is therefore not certain. The alloy will nevertheless have a positive effect of grain refinement on yield strength due to the Hall-Petch effect.

When hydrogen enters the metal however, hydrogen atoms will interacts with dislocations. This causes the dislocation mobility to increase and results in hydrogen enhanced localized plasticity (HELP), a mechanism which will be described in detail later on. The interesting thing to note in this context, is that if plastic deformation occurs more heterogeneous across the grains due to hydrogen, fine grained microstructures are expected to lose more fracture toughness as a result of hydrogen than course grained microstructures.

3.4 Hydrogen's interaction with dislocations

When hydrogen is present in a stressed metal, it diffuses to the dislocations present and interacts with the stress field present around these dislocations. The presence of a hydrogen atmosphere around dislocations lowers the repulsive force between them and causes the dislocation mobility to increase [5,47,52]. It has even been suggested that the interaction between dislocations can shift sign and become attractive at higher hydrogen concentrations, which may lead dislocation pileups to merge together forming cracks [5]. Hydrogen is also transported by dislocations when stress is applied [5,14]. In the case of Inconel-718 which has a low H-diffusivity, this means that once deformation occurs and dislocations move, hydrogen atoms can be transported much further by dislocation drag, than by diffusion alone. In the case of slow strain rate testing (SSRT) of samples containing hydrogen near the surface, this implies that the strain rate will effect the mechanical properties observed. At slow strain rates hydrogen is transported further into the component, increasing the effect of hydrogen embrittlement. When the strain rate increases and the dislocation speed reaches a critical speed however, the hydrogen atoms will no longer be able to follow the moving dislocation [56]. Decreased effect of hydrogen at higher strain rates was observed experimentally by Fournier [16]. In his study, Inconel-718 samples pre-charged with hydrogen were tested at strain rates of $5 \cdot 10^{-7}$, $5 \cdot 10^{-5}$ and $5 \cdot 10^{-3}$ s^{-1}. Almost no embrittlement resulted from hydrogen at $5 \cdot 10^{-3}$ s^{-1} while the SSRTs done at $5 \cdot 10^{-5}$ and $5 \cdot 10^{-7}$ showed respectively more and more embrittlement due to hydrogen. The loss of ductility observed at slow strain rates can be though to apply to cold creep in Inconel-718 as well, since cold creep is effectively a very slow plastic deformation. Since the diffusivity of hydrogen in Inconel-718 is very low, it is therefore likely that cold creep plays a central role in the hydrogen embrittlement of Inconel-718 components exposed to CP.

3.5 Different mechanisms for hydrogen embrittlement

Many mechanisms have evolved trying to explain the failure mechanism of HISC. Each of them can be demonstrated successfully in some material systems, but none of them apply to all the materials exposed to hydrogen embrittlement. The three most commonly cited theories today are the decohesion mechanism , the hydride film formation mechanism and the hydrogen enhanced localized plasticity (HELP) mechanism:

The hydride-film mechanism have been applied successful in some hydride forming materials (e.g. Zr, Ti, V and Nb). In these systems the intensified stress at a crack tip promotes the formation of a brittle hydride film. The crack then propagates through the hydride film and the process repeats until failure occurs [10,31,37]. Despite its limited success, the mechanism cannot be applied in alloys where hydrides don't form. Hydride film formation in Inconel-718 is therefore believed to be highly unlikely.

Then there is the decohesion mechanism [42, 43], in which hydrogen diffuses to the crack tip and reduces the cohesive strength of the alloy. This causes the threshold stress intensity for crack propagation to be reduced, which means that cracks in effect becomes sharper. This mechanism has been successfully demonstrated in ferritic steels, where previously arrested cracks began to propagate when the hydrogen pressure was increased [42]. Interestingly, a reduction in the critical threshold stress intensity in Inconel-718 with increasing hydrogen concentrations has also been observed in the case of Inconel-718 [25].

Most work done on hydrogen embrittlement in Inconel-718 suggests that hydrogen mainly effects the alloy according to the HELP mechanism. This mechanism is based on the fact that hydrogen interacts with dislocations and increases the dislocation mobility [5, 47, 52]. Because of the slow hydrogen diffusivity in Inconel-718,

hydrogen will preferably diffuse into the metal along GBs. Since hydrogen increases the dislocation mobility, it results in a localized plasticity along the GBs when the material is stressed above yield. The net result of this localization of plasticity at the GB's, is that the total elongation to fracture becomes smaller. The effect is also evident from the fracture surfaces resulting from this type of failure, as inter granular (IG) fractures will be present. Closer examinations of these fracture surfaces have shown intense deformation along the fracture surface, and its disputed wether the crack propagate in the vicinity of the GBs or along the GBs themselves [48].

Interestingly, increasing the number of low angle GBs at the cost of high angle GBs through grain boundary engineering, have shown to reduce HISC sensitivity [4]. This is because low angle GBs have lower free volume to accommodate hydrogen atoms. Hydrogen is also segregated at the interfaces of incoherent second phase particles such as MC-carbides or δ-particles [45]. These interfaces act as irreversible traps where hydrogen is segregated and causes localized deformation. If such particles forms at the GBs, it further intensifies the localized deformation caused by the presence of hydrogen. When δ-particles are present at the GBs, they will therefore further increase the embrittlement resulting from hydrogen [26, 35, 36]. The two sketches below illustrate the GB diffusion and the resulting localized plasticity:

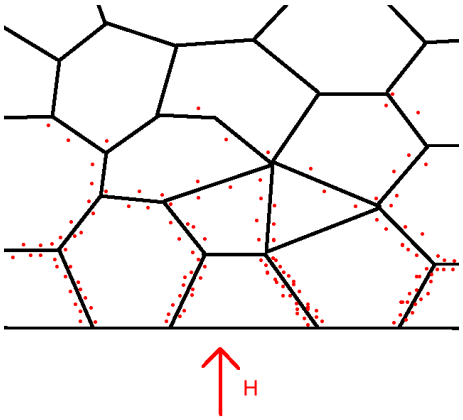

(a) A sketch showing hydrogen diffusion into the material through the GBs.

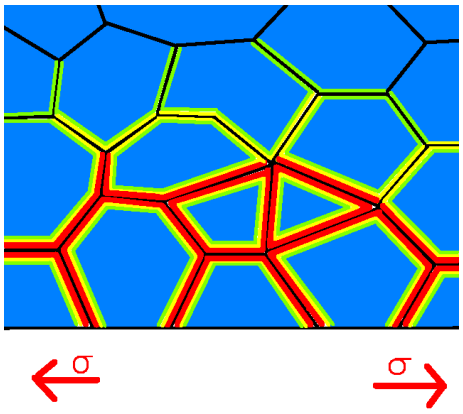

(b) A sketch showing the localized deformation resulting when the same material is stress above yield.

3.6 Hydrogen production from cathodic protection (CP)

When a chemically active metal is exposed to seawater, corrosion will start to occur. The corrosion reaction can be split up into electrochemical half cell reactions: Reduction reactions and an oxidation reaction. In seawater, the reduction reactions will consist of hydrogen evolution and reduction of dissolved oxygen. These half cell reactions are shown in equation 4 and 5. The amount of dissolved oxygen in seawater at subsea depths is limited and the resulting current from this reaction will therefore be very small. In the context of explaining the principles of CP, this reaction is therefore neglected. The dominant reduction reaction is then hydrogen evolution. The metal specie corroding will surrender one or more of its electrons (depending in its oxidation states) as it dissolves in seawater. This is the oxidation reaction, and its summarized in equation 6, where n is the oxidation state of the resulting ion. During corrosion, both these reactions happens simultaneously in a Redox-reaction. The electric charge is therefore conserved. The combined Redox-reaction is shown in equation 7.

$$2H_2O + 2e^- \rightarrow 2OH^- + H_2 \tag{4}$$

$$2H_2O + O_2 + 4e^- \rightarrow 4OH^- \tag{5}$$

$$M \rightarrow M^{n+} + ne^- \tag{6}$$

$$2H_2O + \frac{2}{n}M \rightarrow \frac{2}{n}M^{n+} + H_2 \tag{7}$$

The relationship between the reaction current and the electric potential of each half cell reaction can be expressed through Tafel's equation shown in equation 8. Here b is a constant called Tafel's slope, i_0 is the exchange current density and i is the current density. E is the electric potential. The electric potential is always a relative value and have to be specified against a reference electrode, like the Standard Hydrogen Electrode SHE, the Silver/SilverChloride electrode (Ag/AgCl) or the Standard Calomel Electrode (SCE). The exchange current density (i_0) can be though of as simultaneous oxidation and reduction current density of an electrochemical half cell reaction, when this reaction is at its equilibrium electric potential E_{rev}.

$$E = b \cdot log(\frac{i}{i_0}) \tag{8}$$

When the corrosion is allowed to occur freely, the potential and current density will be determined by the intersection of the Tafel curves from the two half cell reactions. This can be visualised in the Evans diagram shown in figure 4, where the tafel curves from both half cell reactions have been plotted together:

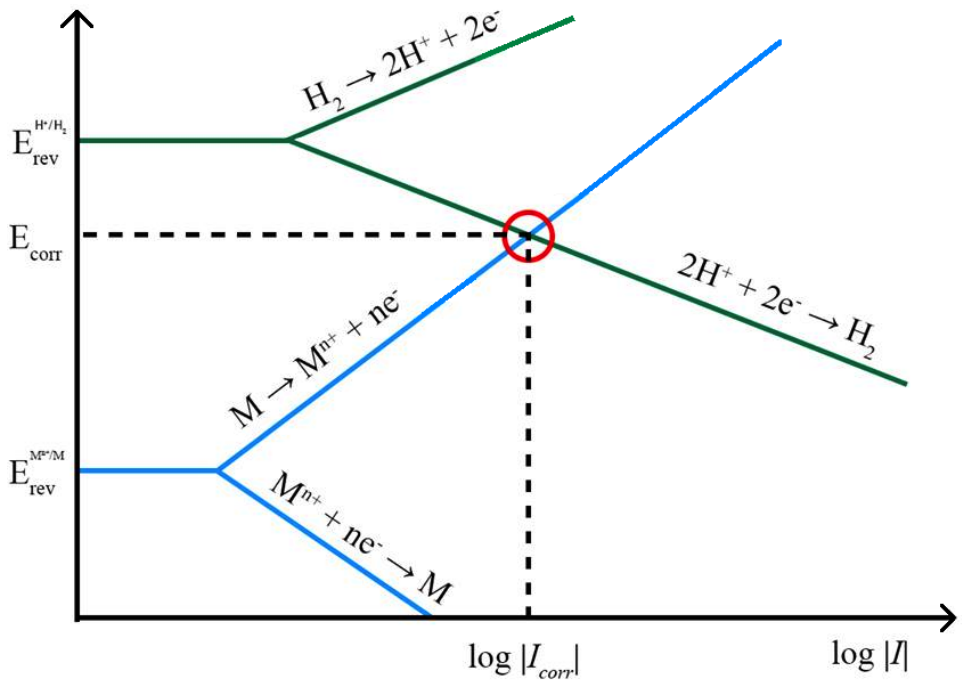

Figure 4: An Evans-diagram showing the corrosion current and potential resulting from hydrogen evolution and dissolving metal as a redox reaction.

When two dissimilar metals M and N are in electrical contact in the same electrolyte, the situation changes. Since two metals cannot have different potentials when they are in electrical contact, M and N will now attain a new galvanic potential called $E_{Coupling}$. The metal M is here the active metal, and N represents the more noble metal. The Evans diagram resulting from this coupling of M and N is shown in figure 5. Typically, the nobel metal N has a tafel curve corresponding to a higher hydrogen evolution current density than M. This means that at $E_{Coupling}$ hydrogen will be produced almost completely from the surface of N. It can also be seen that the corrosion current of M and N has shifted to $I_{corr}^{\overline{M}-N}$ and $I_{corr}^{\overline{N}-M}$ respectively. This means that the corrosion of N has decreased and the corrosion of M has increased. The increased corrosion of metal M, is called galvanic corrosion, and can be very serious if it occurs unintended.

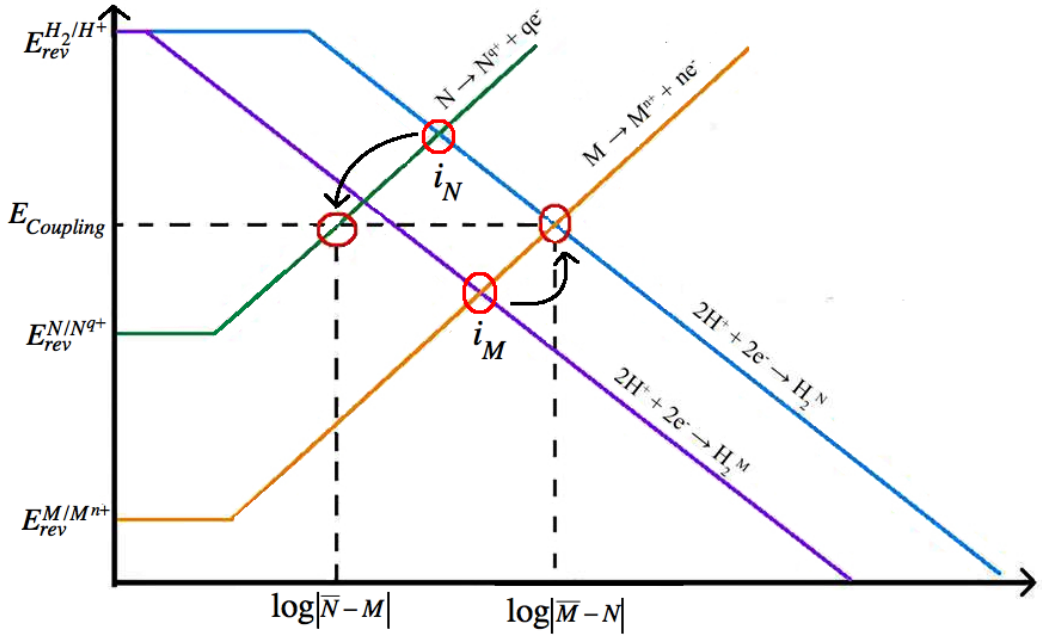

Figure 5: An Evans-diagram showing the corrosion currents of the noble metal N and the less noble metal M during galvanic coupling

The reduced corrosion in metal N coupled with M is the basic principle behind Cathodic Protection (CP). CP is widely used in offshore steel structures submerged in seawater, in order to protect the steel against corrosion. Zinc or aluminium anodes are commonly used. As illustrated in the previous example these sacrificial anodes will suffer from galvanic corrosion while the corrosion of the steel structure is reduced or even eliminated.

Inconel-718 is generally not regarded as seawater resistant by the Oil and Gas industry, and will need CP when exposed to seawater. Corrosion of Inconel-718 is then completely eliminated. When the sacrificial anodes corrode, hydrogen will evolve on the Inconel-718 surface. This is the main source of hydrogen in the subsea applications of Inconel-718. Hydrogen can also come from welding with wet filler materials. This source has however been largely eliminated by stricter welding procedures that require the filler material to be dried prior to welding.

3.7 Hydrogen diffusion in Inconel-718

Because of its FCC structure the Inconel-718 alloy has a high solubility and a low diffusivity with respect to hydrogen. W.M.Robertson [49] measured the solubility, permeability and diffusivity of hydrogen in Inconel-718 and 903. The diffusion of hydrogen was measured through a permeation experiment, where hydrogen diffuses through a thin metal foil of Inconel-718. The diffusion coefficient was then calculated when the diffusion through the foil had reached a steady state. The hydrogen diffusivity in homogenized Inconel-718 was determined as:

$$D = 1.07 \cdot 10^{-2} \exp(\frac{-11,900}{RT}) \frac{cm^2}{s} \tag{9}$$

Where R is measures in cal/mole. Precipitate-hardened samples were also tested in this study, and it was found that the diffusivity was surprisingly stabile across different heat-treatments. The solubility was however found to vary a lot. Solution annealed Inconel-718 showed a higher solubility, presumably because of the high hydrogen affinity of some of the strong hydride forming alloying elements present in solid solution (e.g. Nb and Ti). Hydrogen diffuses both through the grain lattice and along GBs. To which extent these two transport paths dominate the total diffusion in nickel-based alloys have been a subject of controversy. It is difficult to measure the GB and lattice diffusivities separately in an explicit manner, which have resulted in very few studies trying to measure these quantities. There are many different theories and opinions regarding this question, but they vary a lot. They all agree however, that the GB diffusion has to be bigger because of the excess free volume present at the GBs. Some experiments have been done with austenitic steel and pure nickel, but the results reported varies a lot. The GB diffusion of hydrogen have been reported everywhere from 60 [54] to 10^8 [6] times greater than the lattice diffusion, in the case of nickel and austenitic steel respectively. Some theoretical work have been done by Yao [57] on pure nickel, concluding that the GB diffusion

is not necessarily dominant in the total transport of hydrogen a multi crystalline microstructure. Because of this uncertainty, only the effective steady-state, total diffusivity of hydrogen will be considered in the simple diffusion model examined in this master thesis.

4 Theoretical work

4.1 Diffusion of hydrogen during pre-charging

In order to get a rough estimation of the distance which hydrogen is able to diffuse into a thin sample, a numerical model was developed in Matlab. In this model the diffusion was assumed to follow Fick's second law where the diffusion follows the partial differential equation:

$$\frac{dC}{dt} = D_H \cdot \frac{d^2C}{dx^2} \tag{10}$$

In this model the diffusivity of hydrogen is assumed to be independent of hydrogen concentration. The effects of the hydrogen trapping discussed previously, is also ignored. The diffusion constant used in the model above is therefore the steady-state diffusion coefficient measured by Robertson [49]. In the Matlab script a thin plate is considered, where hydrogen diffuses from both ends. The surface concentration on both sides of the thin plate is set to $c_0 = 70wppm$. This concentration corresponds to the solubility limit of hydrogen observed by Yao [58] in nickel. This value is used as reasonable approximation for the solubility of hydrogen in Inconel-718. The 1.4mm sample thickness is divided into 1000 data points, and a numerical 3-point Laplace operator (1,-2,1) is used to compute $(\frac{d^2C}{dx^2})$ as a convolution between the Laplace-operator and the concentration vector. The script uses temperature T($^\circ C$) and diffusion time(days) as input parameters and returns the final concentration profile through the plate after multiple time intervals up to the final pre-charging time. Because of the assumptions made to ignore hydrogen trapping, this model will overestimate the extent of hydrogen diffusion, as hydrogen atoms otherwise irreversibly trapped are assumed to diffuse freely into the sample. This can be adjusted for by using diffusion equations which account for trapping. These equations are complex and nevertheless needs to be fitted to experimental data. Since this is

beyond the scope of this master thesis, it will not be attempted here. Interactions between dislocations and hydrogen atoms are also ignored in this model, a mechanism which increases the hydrogen transport into the sample if stress is present. Because all the samples considered in this sample are pre-charged without any mechanical load, this is not considered to be a significant source of error in this context.

This model serves as a rough estimate of what could be expected in terms of how far from the surface the Inconel-718 samples can be expected to be embrittled. Previous experiments correlating hydrogen concentrations with corresponding fracture morphologies [24], have displayed completely IG fractures above 20 wppm H. In the case of the new pre-charging equipment used in this master thesis, this model was utilized to compare the hydrogen concentration profiles expected from the old and new pre-charging procedures. The old pre-charging setup comprised of pre-charging at $80°C$ for 10 days, while the new pre-charging procedure last for 5 days at $120°C$. The resulting profiles are displayed in figure 6a and 6b. The figures clearly show the improvement predicted when increasing the pre-charging temperature from 80 to $120°C$.

In order to verify the effectiveness of the new pre-charging method, a dummy sample was first pre-charged for 3 days at $120°C$ according to the new pre-charging equipment. The hydrogen content was then measured by SINTEF using a Hydrogen Melt Extraction Analysis, which measured a concentration of 21.3 wppm H. The model predicts an average concentration of 29.5 wppm after 3 days, which means that the model overestimated the total hydrogen concentration with 38% in this particular case. The model predicts an average concentration of 37.8 wppm H after 5 days of pre-charging at $120°C$, which with an overestimation factor of 1.38 corresponds to a real concentration of about 27.4 wppm H. The implicit assumption that the overestimation factor is constant is also a very rough approximation in this context since diffusion is not a linear process. The transition from ductile to brittle IG fracture is observed to occur from around 15-25 wppm H [24]. The simple Matlab

analysis performed therefore suggests that a significantly thicker surface zone will be embrittled from the new pre-charging equipment.

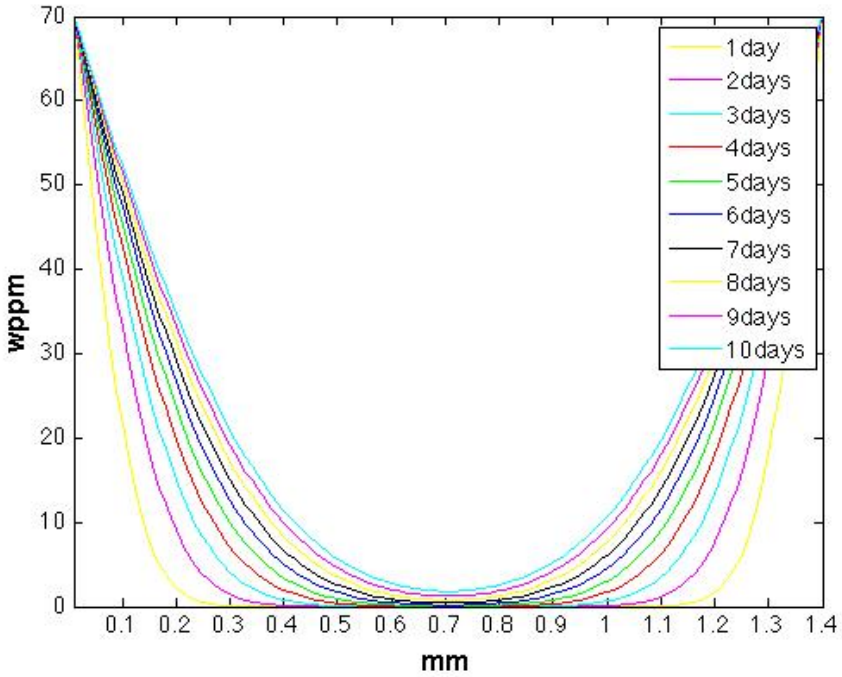

(a) Numerically estimated hydrogen concentration profiles in a 1.4mm thick sample, through 10 days of pre-charging at $80°C$

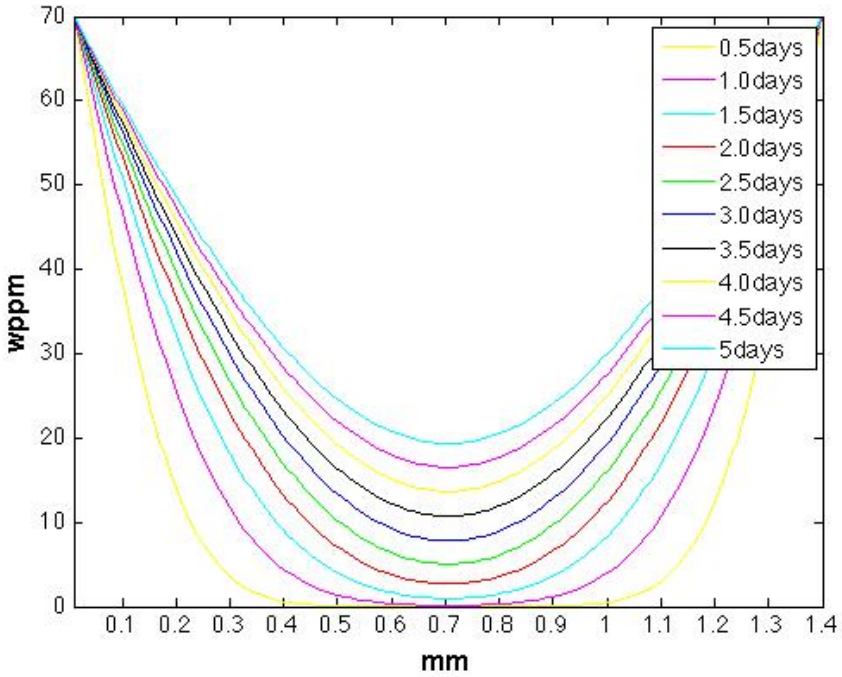

(b) Numerically estimated hydrogen concentration profiles in a 1.4mm thick sample, through 5 days of pre-charging at $120°C$

4.2 Some perspective on the accelerations involved in pre-charging

Pre-charging at $120°C$ offers a new method for accelerating the absorption of hydrogen that would otherwise take months or years to accomplish at room temperatures. It would however be useful to relate the amount of hydrogen resulting from pre-charging at $120°C$ to the amount of time necessary for the same amount of hydrogen to be absorbed at room temperature. In order to derive an expression for this relationship, some simplifications will have to be made. The relationship between hydrogen evolution kinetics and temperature is ignored. This can be partly justified, since the diffusion of hydrogen in Inconel-718 will be the limiting process. Dislocation-hydrogen interactions are also ignored, since the samples are not stressed during pre-charging. The final simplification is to ignore the irreversible trapping of hydrogen at the interfaces of secondary particles like MC-carbides. Because of the high activation energy associated with these trap sites, its likely that they will be irreversible both at room temperature and at $120°C$. The trapping sites will therefore contribute to lowering the overall diffusion at both temperatures, and their effect will at least partially cancel each other out in the ratio between two pre-charging times.

In this derivation, hydrogen absorption from one flat surface is considered. The surface concentration of hydrogen is assumed to be constant and Fick's second law is assumed to apply. This results is the well known analytical solution to Fick's second law:

$$\frac{c(x,t) - c_0}{c_s - c_0} = erfc(\frac{x}{2\sqrt{D_H \cdot t}}) \tag{11}$$

We wish to calculate the diffusion time at a lower temperature such that the depth of transition between ductile and IG fracture occurs at the same distance from the surface after pre-charging at both temperatures. If we insert the constant transition depth X_{trans} and the corresponding constant hydrogen concentration at this depth

C_{trans}, this results in both sides of the equation becoming constant. This means that at the transition depth: $D_H \cdot t = constant$. The equivalent room temperature time which would result in the same depth of brittle fracture as 5 days of pre-charging at $120°C$can then be estimated as:

$$t^{RT} = \frac{D_H^{120°C} \cdot t^{120°C}}{D_H^{RT}} \tag{12}$$

The equivalent room temperature time corresponding to pre-charging for 5 days at $120°C$ is calculated in equation 13. The diffusion expression used in this equation is the steady state diffusivity measured by Robertson [49].

$$t^{RT} = \frac{\exp(-11,900/1.9872 \cdot 393)}{\exp(-11,900/1.9872 \cdot 298)} \cdot 5\ days = 644\ days \tag{13}$$

This corresponds to almost two years! It should be emphasized that the numerous assumptions made in deriving this expression makes the answer a very course estimate at best. The answer is therefore only an estimate of the magnitude of the time acceleration involved, and should not be regarded as a precise tool. Dislocation drag will greatly increase the transport of hydrogen at both temperatures when stress is applied. Furthermore, the surface concentration is not necessarily constant across the two different temperatures, as the solubility of hydrogen is temperature dependent. In addition to this, surface layer and roughness may effect absorption of hydrogen into the metal. The calculations are nevertheless meant to add some perspective on the accelerations involved, and the potential benefit of using high temperature pre-charging as an accelerated test method.

4.3 Measuring error involved in the tensile stress data acquired

In measuring the gauge area of the tensile test samples, some measuring error occurrs. The maximum measuring error i both dimensions was estimated to 0.02mm based on measuring the same gauge many times at different places along the sample length. The area of a cross section is given by $W \cdot T$, where W is the width and T is the thickness. If we include the measuring errors ϵ_W and ϵ_T we get the expression:

$$A_{measured} = (W + \epsilon) \cdot (T + \epsilon) = WT + W\epsilon_T + T\epsilon_W + \epsilon_W\epsilon_T$$

$\epsilon_W\epsilon_T$ can then be neglected because its very small. Assuming $\epsilon_W = \epsilon_T$ we get:

$$A_{measured} = WT + \epsilon(T + W) = A_{real} + \epsilon(T + W)$$

The stress is given by force per area: $\sigma = \frac{P}{A}$. The relative error in stress can then be estimated as:

$$\frac{\epsilon_\sigma}{\sigma} = \frac{\frac{P}{A_{real}+\epsilon(W+T)} - \frac{P}{A_{real}}}{\frac{P}{A_{real}}} = \frac{A_{real}}{A_{real} + \epsilon(W + T)} - 1 \tag{14}$$

A typical gauge dimension of the Inconel-718 samples was $1.35mm \cdot 4.95mm$. Using these typical dimensions to calculate the gauge area and assuming + 0.02mm measuring error in both dimensions, we get a relative error in stress of:

$$\frac{\epsilon_\sigma}{\sigma} = \frac{1.35 \cdot 4.95}{1.35 \cdot 4.95 + 0.02 \cdot (1.35 + 4.95)} - 1 = -1.85\% \tag{15}$$

Note that in this example, the error was estimated when both errors were at their maximum in the same direction. Since the measuring errors on average are less then 0.02mm and can have opposite signs, the average relative error will be smaller. 1.85% is therefore a maximum error estimate, not a standard deviation.

4.4 FEM analysis of notched samples in Abaqus

Notched tensile test samples were also tested in this master thesis. A total of 6 notched samples where tested: One with and one without hydrogen from three different alloys. The alloys examined where 56LH-1-OP, P3A01-1900 and P3A01-1800. These alloys where chosen in order to compare the compositions and microstructures examined in this study. 56LH-1-OP and P3A01-1900 both have the same course and δ-free microstructure, but different compositions. P3A01-1900 and P3A01-1800 both have the same composition but different microstructures, the latter microstructure with fine grains scattered with δ-particles and the former with course grains and no δ-particles. The purpose of running the notched samples was to obtain better time-lapse videos of the crack propagation since the initiation point would be known. In the smooth samples, this proved difficult since secondary cracks initiated at a number of spots. A picture with dimensions is displayed in figure 7, showing the size and shape of the notched tensile test samples. The samples each contained two notches on each side of the sample gauge, both with a depth of 0.6mm and a tip radius of 0.3mm.

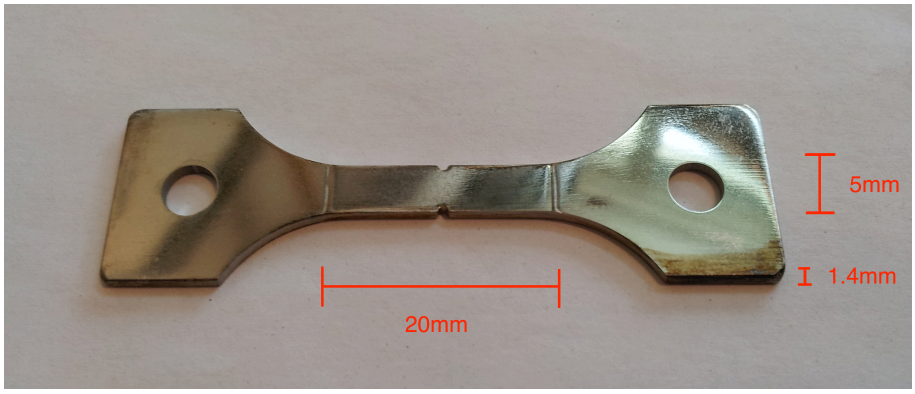

Figure 7: A photo showing a notched sample after sample preparation and pre-charging.

In order to design an appropriate loading schedule for these samples the stress strain behaviour of the notched geometry had to be determined. This was done using a standard static analysis in Abaqus. The notched gauge area of the samples was modelled as a 2D shell geometry in Abaqus, and plain strain was assumed to apply. This assumption will be reasonable if the sample is thin and flat, which it is. Since the outer width and thickness of the notched samples varied with a few hundredth of a mm, one model was created for each sample in order to account for this. For the material properties, an E-modulus of 210Gpa and a poisson coefficient of 0.3 were used for the elastic regime of the stress-strain curve. For the plastic regime a Ramberg - Osgood relationship given in equation 16 was assumed as an approximation. In this model, the YS, UTS and ϵ data given by ATI-metals where fitted to obtain K and n for each of the three alloys. Before the material data was entered into Abaqus, the engineering strain and engineering stress had to be converted into true stress and true strain. The relationship between these entities are displayed in equation 17 and 18.

$$\epsilon = \frac{\sigma}{E} + K \cdot (\frac{\sigma}{E})^n \tag{16}$$

$$\sigma_{True} = \sigma_{Eng.} \cdot (1 + \epsilon_{Eng.}) \tag{17}$$

$$\epsilon_{True} = ln(1 + \epsilon_{Eng.}) \tag{18}$$

A few things should be noted about the possible errors in the Abaqus model. When a significant portion of the sample cross section starts to become plastically deformed the poisson contractions will make the plain strain assumption invalid due to shear stresses occurring in the z-direction. The second and perhaps biggest error source in this model is absence of any failure mechanism. Since no damage mechanisms have been included in this simple Abaqus model, the material is assumed to remain perfectly cohesive throughout the deformation. This stands in contrast to the cracking and micro void nucleation that would occur in reality. The model will therefore overestimates the UTS of the sample. The purpose of this Abaqus analysis was nevertheless to determine the yield point for the notched samples, in order to assign appropriate initial loads. The overestimation of UTS was therefore not considered a relevant problem in this context.

A picture showing the 2D sketch in Abaqus is shown in figure 8. The test done in Abaqus consisted of pulling the sample 4mm in 100 increments. At each increment the reaction load is recorded, and subsequently used to generate a Load - Displacement plot for the sample. These plots will then work as an estimate for the YS of the notched sample, and will be used to assign an appropriate starting load slightly above YS. The resulting Load - Displacement curves are shown in figure 9. Images of the stress field at two different loads are also included in figure 10. The visual stress fields show an intense stress concentration around the notch which extends in a circular area between the two notches. This area of plastic deformation could also be observed during testing, due to he poisson contraction in the deformed areas. A picture is included in figure 11 showing the pattern observed during testing. The patterns are strikingly similar.

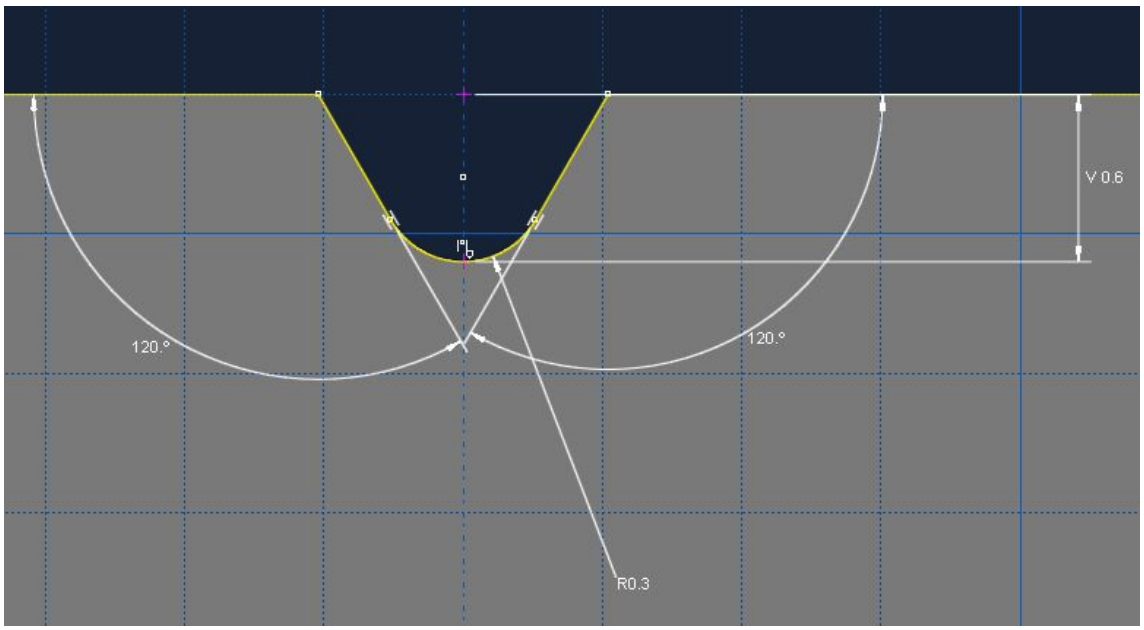

Figure 8: A sketch showing the notch geometry and tip radius. The notch has a depth of 0.6mm and a tip radius of 0.3mm

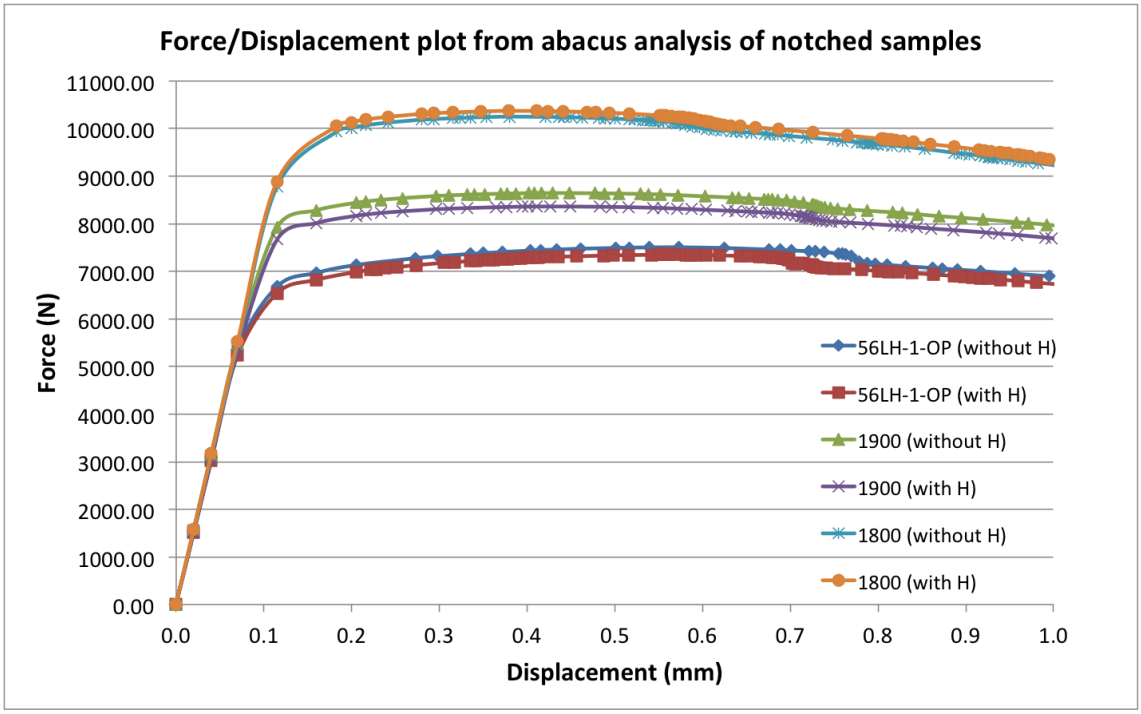

Figure 9: Force-Displacement behaviors predicted by the Abaqus model. The sample with and with out pre-charging have slightly different dimensions, resulting from the sample preparation step. This has been factored in in the analysis thereby the slight misalignment between the two samples from each alloy.

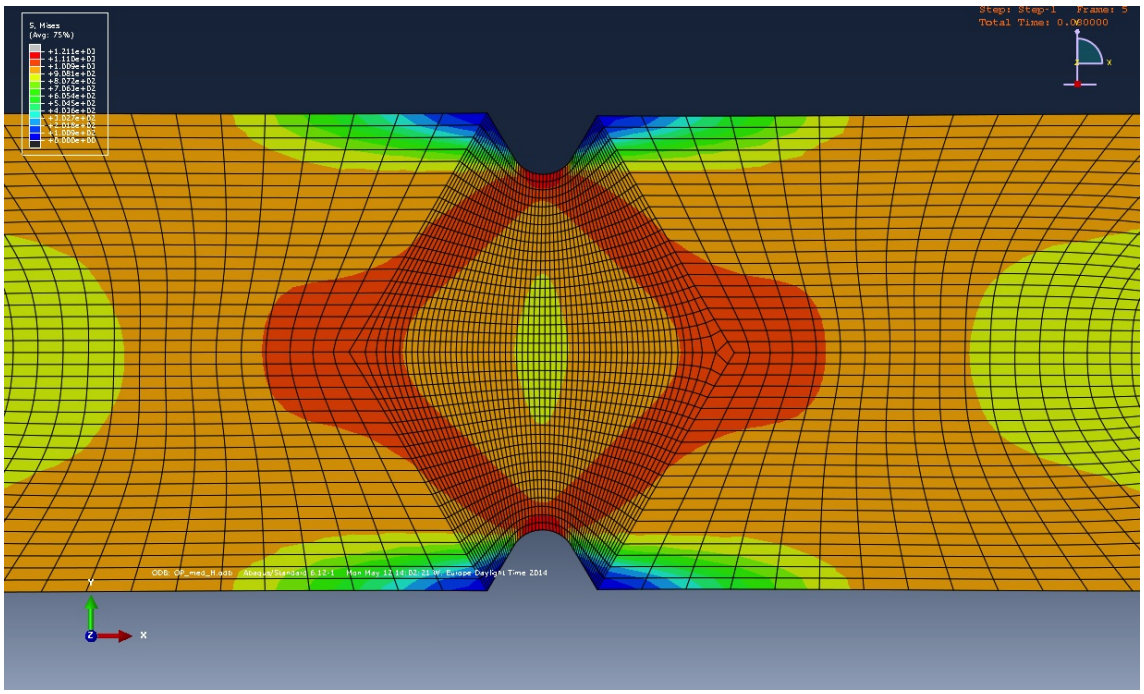

Figure 10: A visualisation of the stress field produced during. The image corresponds to one of the 56LH-1-OP samples at a 0.32mm displacement.

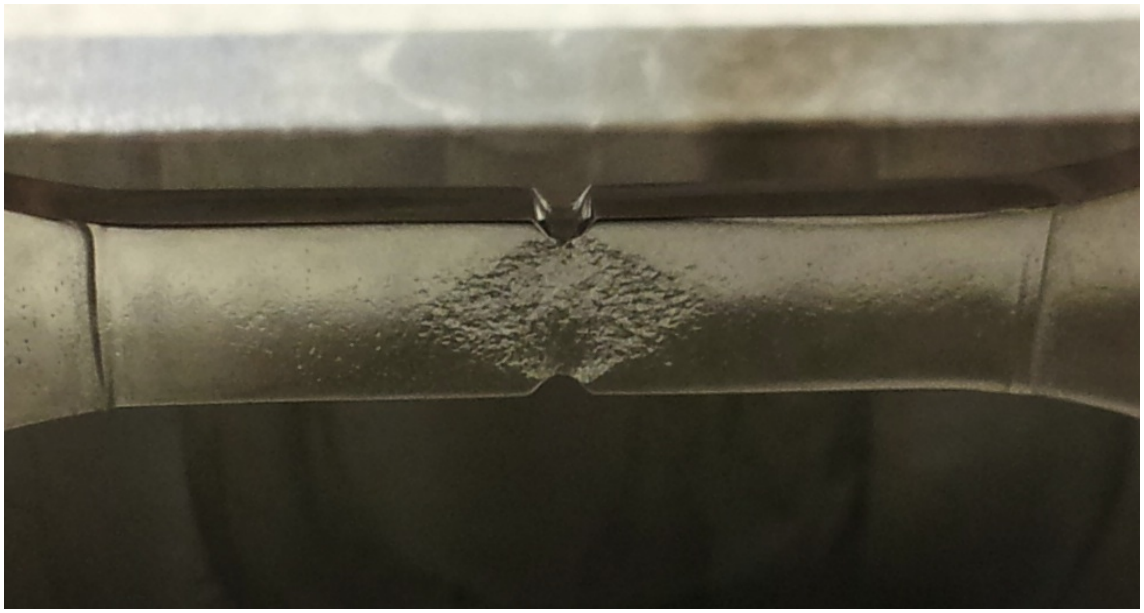

Figure 11: The deformed notch area observed during testing. The picture was taken from the hydrogen free reference sample of 56LH-1-OP at a displacement of 0.32mm

5 Experimental

5.1 Compositions and microstructures examined

A total of 6 different alloys were examined in this study: Two compositions combined with three microstructures. The two compositions consisted of a standard commercial composition named 56LH-1-OP and a High Nb low C/N variant of Inconel-718 called P3A01. The two compositions are summerized in table 2 and 3. The P3A01 alloy was produced as a 300lb cast electrode, which were remelted using VAR and cast as a 8" ingot. This ingot was homogenized at 1190 $°C$. The standard composition ingot was taken from a commercial billet. This billet started as a 10000lb 21" diameter VIM cast, which was then remelted using VAR and cast into a 24" diameter billet. The standard composition ingot was also also homogenized, although the exact homogenization treatment was kept secret for commercial reasons. Ingots from both compositions were then TMP'ed on order to yield three different microstructures for each composition, and subsequently aged. The compositions and microstructures are summarized in table 1. The P3A01-1850A variant was intended to achieve a course microstructure, similar to the 56LH-1-Piece-1 alloy. This had been achieved the last time the test material was produced, but failed to materialize when the ingot size was scaled up from the laboratory scale test used last time. P3A01-1850A and P3A01-1800 therefore have an almost identical microstructure. All the 6 variants were nevertheless included in all steps of this master thesis. Pictures of the 6 ingot materials received are displayed in figure 12a - 12f. Their respective microstructures are shown in figure 13a - 13f.

Table 1: Alloy variants

Alloy	Composition	Microstructure	YS	UTS
56LH-1-OP	Standard grade	Course grains, δ-free	911Mpa	1218Mpa
56LH-1 Piece-1	Standard grade	Course grains, globular δ-particles	823Mpa	1159Mpa
56LH-1 Piece-2	Standard grade	Medium grains, globular δ-particles	1163Mpa	1391Mpa
P3A01-1800	Low C/N and high Nb	Course grains, δ-free	1109Mpa	1341Mpa
P3A01-1850A	Low C/N and high Nb	Fine grains, globular δ-particles	1293Mpa	1498Mpa
P3A01-1900	Low C/N and high Nb	Fine grains, globular δ-particles	1356Mpa	1576Mpa

Table 2: Alloy compositions (wt%)

Alloy	Al	Co	Cr	Fe	Mo	Nb	Ni	Si	Ti
56LH-1	0.52	0.05	17.62	19.14	2.87	4.98	53.77	0.07	0.95
P3A01	0.53	0.01	17.64	18.64	2.88	5.35	53.91	0.02	1.00

Table 3: Trace elements (wt%)

Alloy	C	S	P	O	N	B
56LH-1	0.018	<0.0003	0.008	NA	NA	0.004
P3A01	0.004	0.0006	0.009	<0.0005	0.0029	0.005

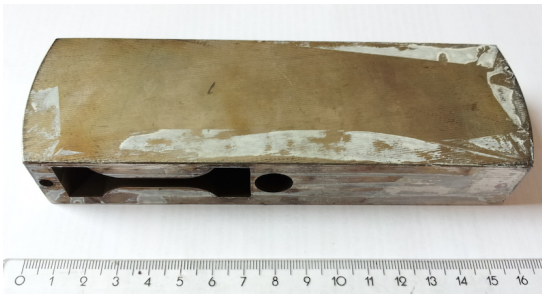

(a) The 56LH-1-OP Ingot received from ATI-metals

(b) The P3A01-1900 Ingot received from ATI-metals

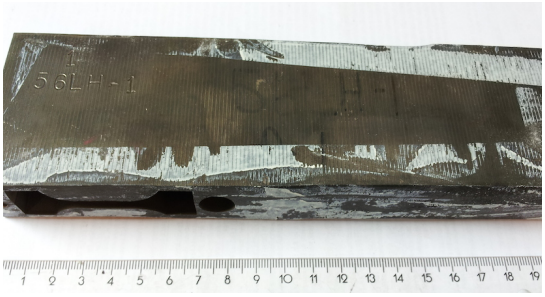

(c) The 56LH-1-Piece-1 Ingot received from ATI-metals

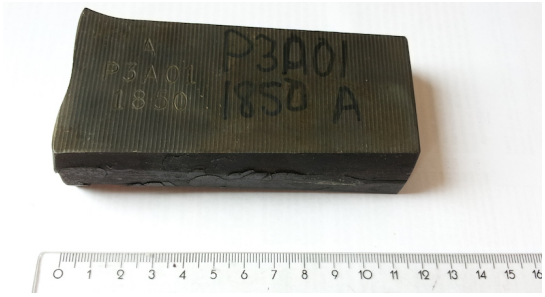

(d) The P3A01-1850A Ingot received from ATI-metals

(e) The 56LH-1-Piece-2 Ingot received from ATI-metals

(f) The P3A01-1800 Ingot received from ATI-metals

Figure 12: Ingots received by ATI-metals. Some of the ingots contain holes after samples have been but out.

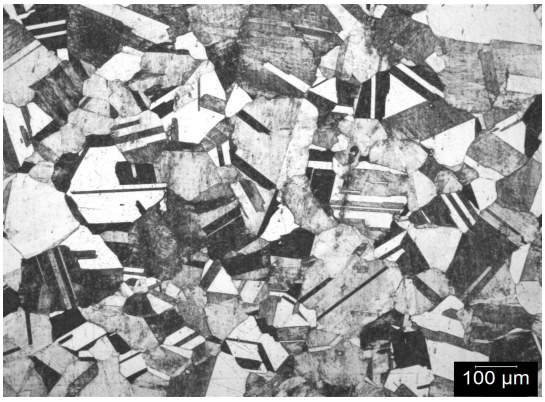

(a) 56LH-1-OP: Standard alloy composition. Course grains with no δ-particles.

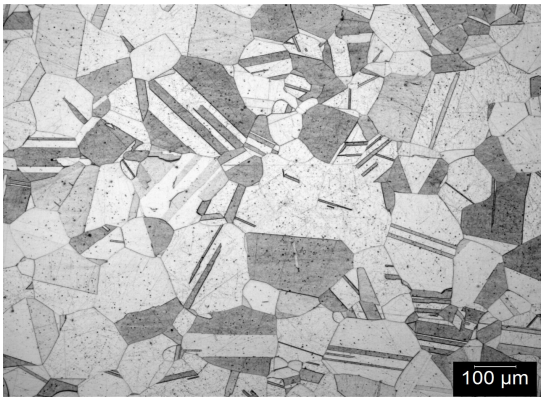

(b) P3A01-1900: Low C/N, high Nb content. Course grains with globular δ-particles.

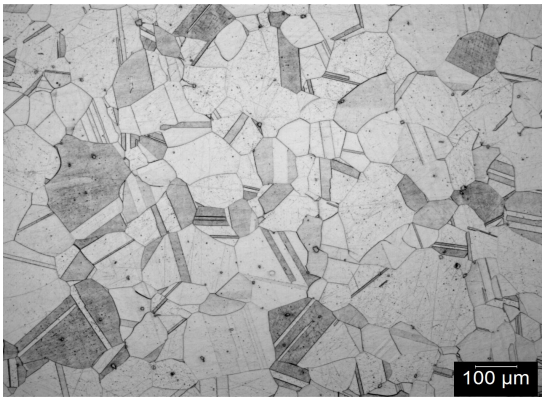

(c) 56LH-1-Piece-1: Standard alloy composition. Course grains with globular δ-particles.

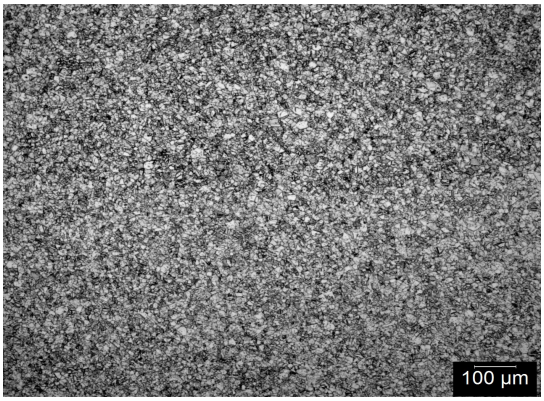

(d) P3A01-1850: Low C/N, high Nb content. Fine grains with globular δ-particles.

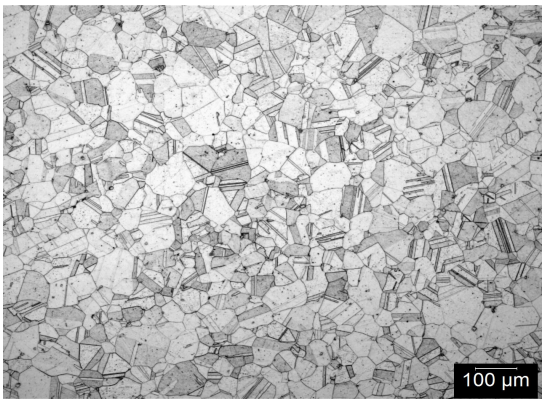

(e) 56LH-1-Piece-2: Standard alloy composition. Fine grains with globular δ-particles.

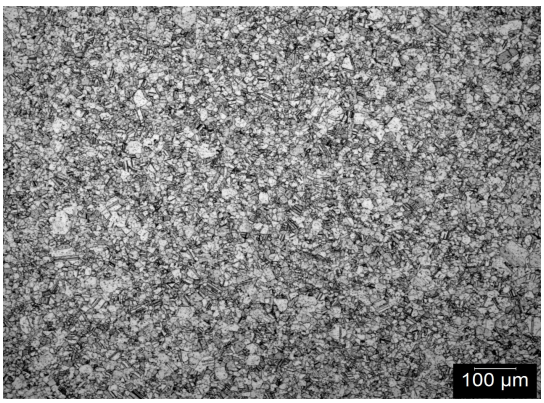

(f) P3A01-1800: Low C/N, high Nb content. Fine grains with globular δ-particles.

Figure 13: Microstructure in the 6 Inconel-718 variants

5.2 Sample preparation

5.2.1 Smooth tensile test samples

Tensile test samples were cut from the ingots in the direction such that the length of the gauge was parallel to the rolling direction of the ingot. The samples were cut out using spark erosion, which was done by NOMEK AS. Once the tensile samples had been received, they were grinder by progressively finer SiC papers on all sides, to remove the brass contaminant and the oxidation products from the spark erosion process. After grinding, the samples were mechanically polished with 6, 3 and finally 1 μm diamond suspensions. Between each step the samples were subjected to ultrasonic cleaning in an ethanol. Afterwards, the samples were electropolished on one side of the gauge. This was done in order to remove surface deformations and to get a smooth surface which could be examined in the microscope used in the tensile tests. A picture is shown in figure 14, showing a tensile test sample before and after sample preparation.

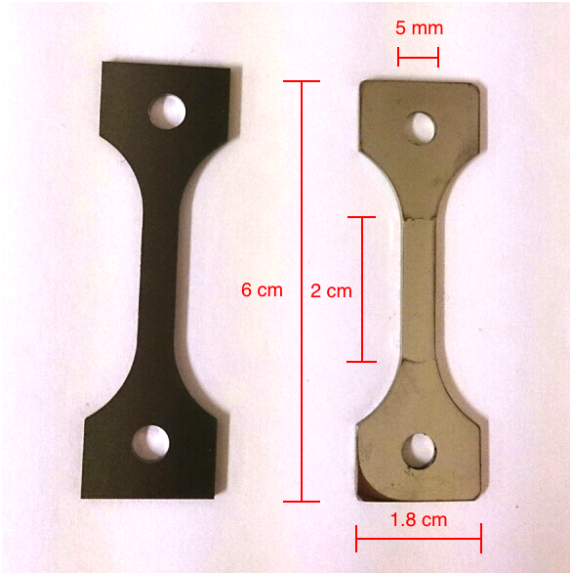

Figure 14: A picture showing a smooth tensile test sample before and after grinding, polishing and electropolishing

5.2.2 Notched tensile test samples

The notched samples were mechanically grinder and polished according to the same steps as the smooth samples. The notch area was also grinded with 1200 grit SiC paper by hand to remove the surface contaminants present there. The notched samples were electropolished on both sides. This was done to prevent crack initiation on rougher "back-side" of the gauge, which would be unobservable during testing. A picture is shown in figure 15, showing a notched sample after sample preparation.

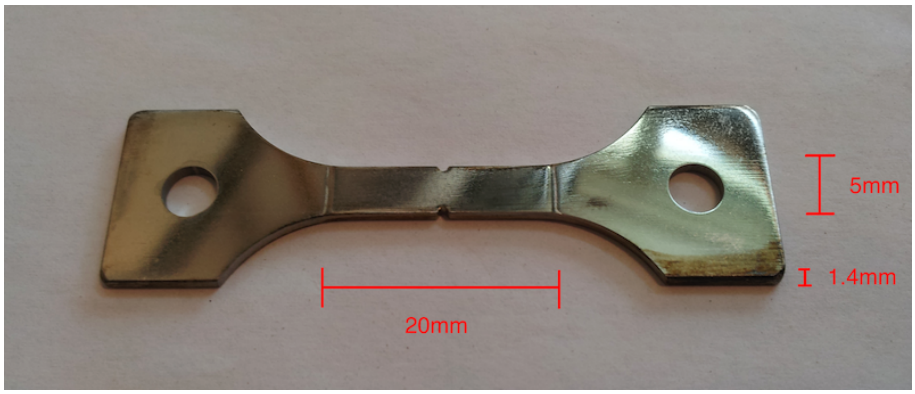

Figure 15: A picture showing a notched tensile test sample before and after grinding, polishing and electropolishing

5.2.3 Samples prepared for observations in the optical microscope

Some cylindrical samples were also cut from the ingots. These samples were intended for micro structural imaging in the optical microscope (OM). The OM samples were mechanically grinded and polished according to the same steps as tensile samples. Instead of electropolishing however, these samples were anodized for 30s at 3V in a 10 vol% Oxalic Acid solution. This resulted in a dark oxide layer on the samples, which gave contrast to the microstructures when the samples were observed in the OM. Pictures of an OM sample after polishing and anodizing is shown in figure 16.

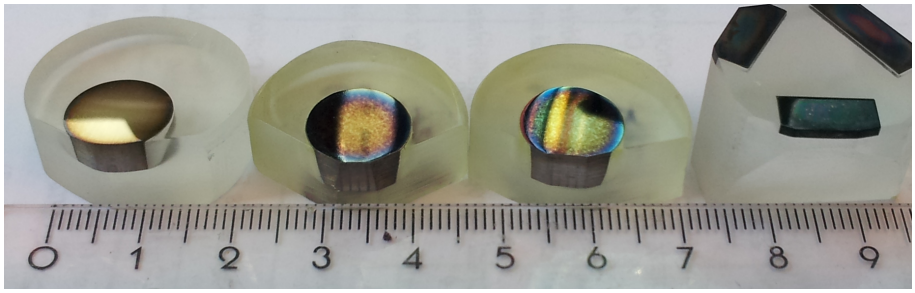

Figure 16: A picture showing the OM samples after anodizing. From the left: 56LH-1-OP, 56LH-1-Piece-1 and P3A01-1900. In the round sample holder 56LH-1-Piece-2, P3A01-1850A and P3A01-1800.

5.3 Pre-charging equipment developed

The pre-charging done in this thesis was done using a 2:1 mixture of Glycerol/Ortho-Phosphoric Acid as electrolyte instead of synthetic seawater. The motive for this was to achieve an accelerated pre-charging by raising the temperature above $100°C$. Pictures showing the pre-charging setup are shown in figure 17 and 18. The setup allows for multiple parallels of pre-charging to be carried out at the same time. In each parallel, 4 samples, which were connected with platinum wires are submerged in a 250ml glass bulb filled with Glycerol/Ortho-Phosphoric Acid. Two Pt counter electrodes, one from each side of the samples were used in order to obtain a more

uniform cathodic current (CC) on both sides of the samples. All the parts involved in the pre-charging chambers were made out of pyrex glass or plastic. No metal parts other than platinum wires were used. This was done to avoid corrosion and contamination due to corrosion products, a problem encountered in the preceding project work. In the project work, metal screws inside the pre-charging chamber corroded and left residues on the samples. The pre-charging chambers were connected to $Hg/HgSO_4$ reference electrodes through plastic tubes filled with Glycerol/Ortho-Phosphoric Acid. The reference electrodes contained a membrane to shield the inside sulphate solution from the outside glycerol solution. The pre-charging chambers were partially submerged in a bath heating oil, which was heated to 120 $°C$ and controlled using a heating element connected to an electronic thermostat. The pre-charging was done using electronic $Gamary^{TM}$ potensiostats, which logged the CC every 30s. All samples were pre-charged at -1500mV $Hg/HgSO_4$, which corresponds to -1050mV AgAgCl. In order to verify that this new setup worked to its intensions, an Inconel-718 dummy sample was pre-charged for 3.5 days, and subjected to a hydrogen melt extraction analysis performed by SINTEF. The hydrogen concentration of the sample was measured to 21.33 wppm H, which corresponds to a substantial degree of hydrogen embrittlement in Inconel-718 [25]. All samples were therefore pre-charged for 5 days at these conditions to ensure adequate hydrogen. After pre-charging for 5 days, samples are removed from the chambers and washed in ethanol, before being stored in a freezer at -19$°C$ until testing.

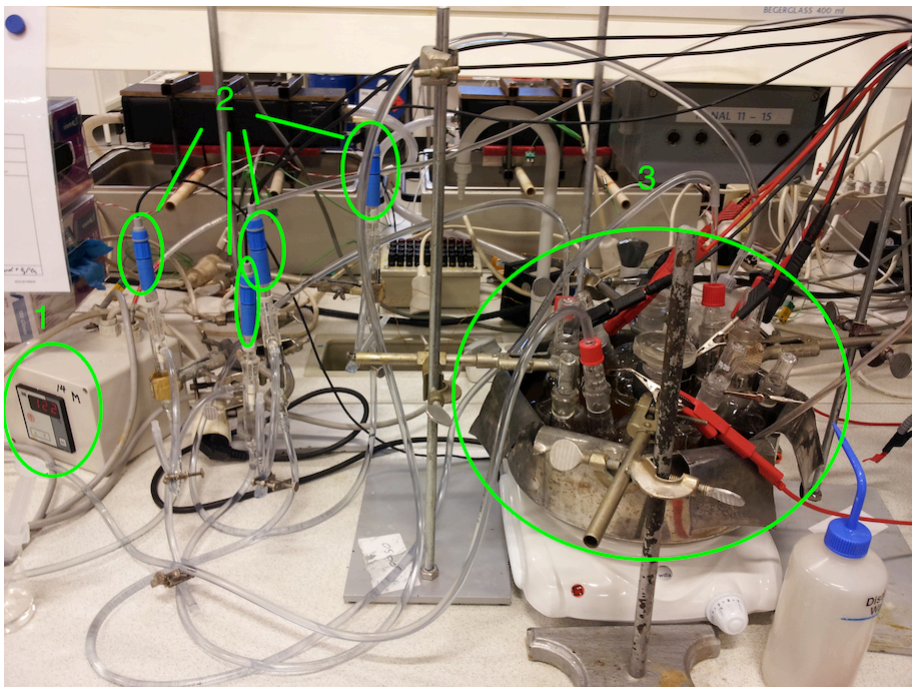

Figure 17: An overview image of the pre-charging setup used. The Thermostat is located to the left in the picture (1), the $Hg/HgSO_4$ reference electrodes in the middle (2) and the heating oil reservoir containing multiple pre-charging parallels is located to the right (3).

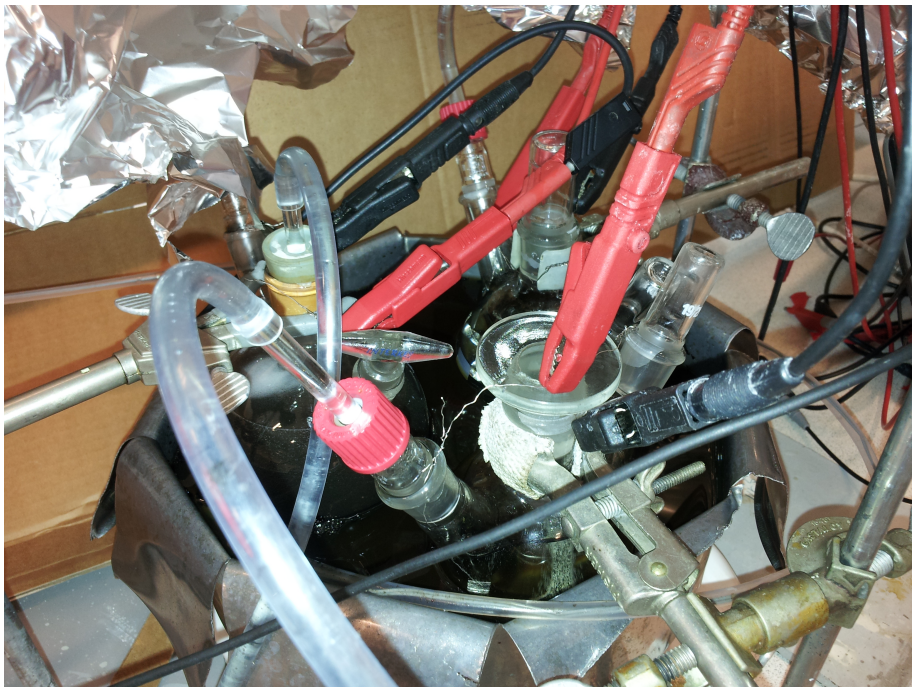

Figure 18: A close up picture showing the different parallel pre-charging chambers immersed in the heating oil reservoir.

5.4 Tensile test equipment

The tensile test equipment used to test the pre-charged Inconel-718 samples involved three $ME - systeme^{TM}$ load cells, each with a capacity of a 1 Ton equivalent load. These machines were cranked by hand using a torchmeter and were mounted to the desk workspace with vices. Two-part electrolyte chambers were developed in the project work preceding this master thesis. These electrolyte chambers allow exposure to synthetic seawater and potensiostatic polarization during testing. A picture is included in figure 19 and 20 showing the tensile equipment during testing. The electrolyte chambers parts were made out of Poly Carbonate (CP) with stainless steel screws holding the two pieces together. The stainless steel screws and the metal parts of the tensile machine itself were not galvanically coupled with the samples during testing. During testing a standard Ag/AgCl reference electrode is used together with a platinum counter electrode placed behind the sample gauge in order to achieve a -1050mV Ag/AgCl polarization. This simulates the CP protection potential of Aluminium or Zinc in saltwater. The purpose of CP during testing was to resupply the hydrogen at the surface during testing. Design sketches of the PC electrolyte chamber design are given in the appendix. The front side of the PC electrolyte chambers were polished to a transparent finish, allowing the sample to be observed during testing. A $DinoLite^{TM}$ microscope mounted on a XYZ - micro movement stage allowed the sample surface to be accurately scanned and focused on during testing. The microscope was capable of obtaining photos, videos and constructing time-lapse videoes by taking pictures at fixed time intervals.

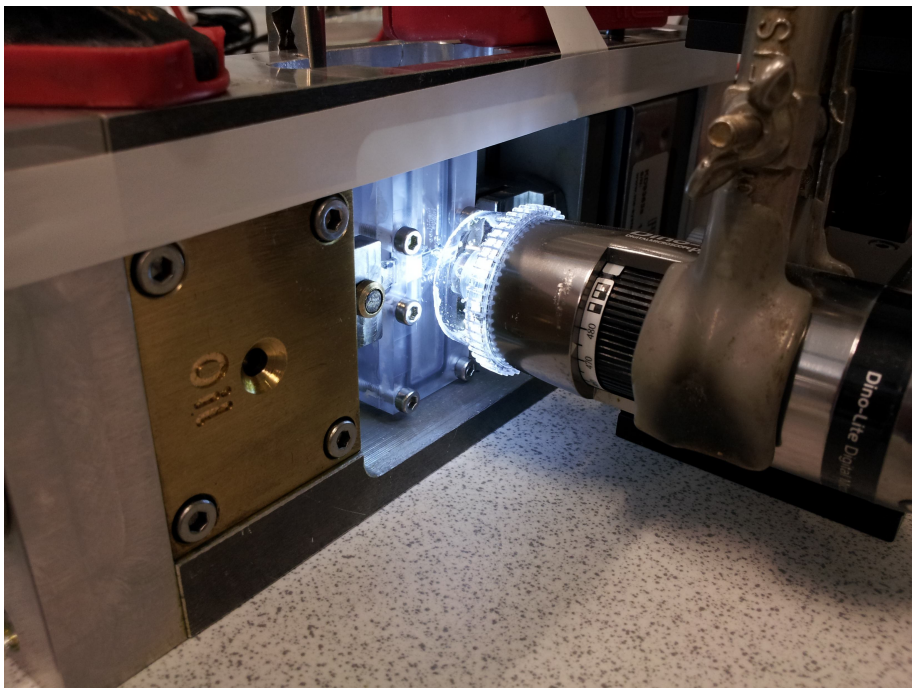

Figure 19: A picture showing the tensile test setup during testing. The electrolyte chamber is filled with synthetic saltwater and the sample is polarzed to -1050mV Ag/AgCl. An optical microscope is used to monitor the microstructure during testing.

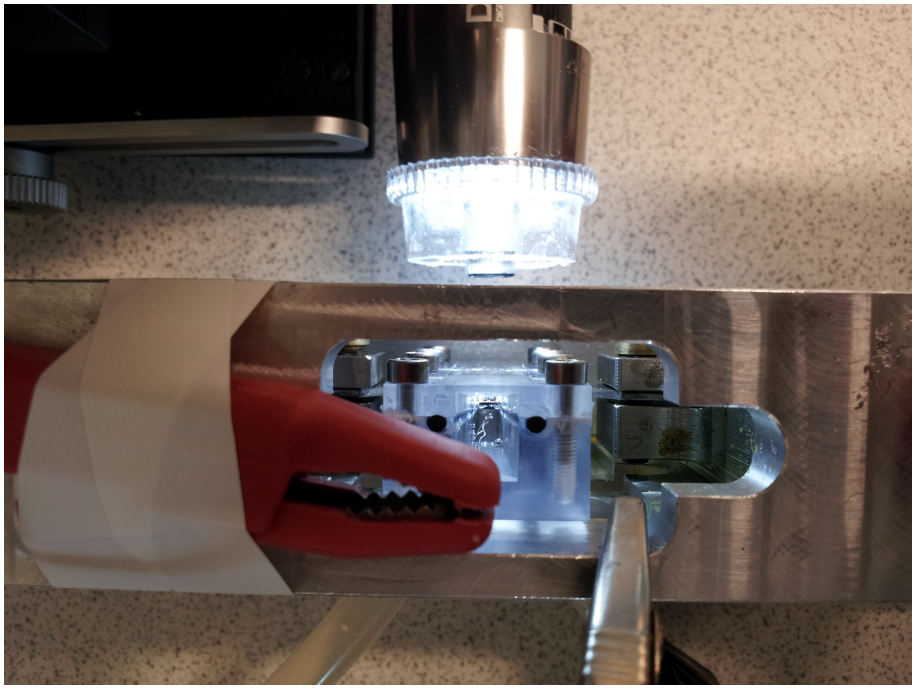

Figure 20: I picture showing the same equipment form the top. The counter electrode is placed behind the sample, and the reference electrode is connected through the nozzles on the backside of the electrolyte chamber.

5.5 Tensile test procedures

From each of the alloy variants, 4 sample with pre-charging are tested. In addition, 2 reference samples without hydrogen pre-charging are tested in air. Before testing the cross sections are measured. The samples are then cleaned thoroughly in ethanol and distilled water and placed inside the electrolyte chamber in the load cell. The chamber is then closed, tightened, filled with synthetic saltwater, and a potensiostatic polarization of -1050 mV Ag/AgCl is applied.

The stepwise constant load utilized in this master thesis originates from previous HISC testing done on Super Duplex Stainless Steel (SDSS) at NTNU and SINTEF [1, 30, 33]. Johnsen et. al [33], showed that in the case of SDSS, step-wise constant loading and direct loading to the final stress resulted in the the same critical stress for HISC. Little work have been done on constant load HISC testing of Inconel-718. This test method was nevertheless assumed to be applicable for Inconel-718 as well. The pre-charged 56LH-1-OP and P3A01-1900 samples tested in the project work fractured at 132% and 125% of YS respectively. Since these samples were pre-charged at $80°C$ at -1050 mV Ag/AgCl in synthetic salt water, the initial load in this study was set slightly lower, at 116% and 108% for the 56LH-1-OP and P3A01-1900 alloys respectively. This was done since the new pre-charging equipment is expected to result in more hydrogen and potentially lower fracture strengths. The initial load for the rest of the alloy variants tested were based on considerations of the YS to UTS range in each respective alloy, and comparing them to those of 56LH-1-OP and P3A01-1900. The initial starting loads are summarized in table 4 and 5. One samples from alloy 56LH-1-OP (Sample-1), P3A01-1900(Sample-1), and P3A01-1850A(Sample-1) were loaded with a different initial load, other things the same. The alloys were picked based on variations in microstructure (P3A01-1900 vs. P3A01-1850A) and composition (56LH-1-OP vs. P3A01-1900). The reason for testing using a different initial load, was to give an indication wether the independence of direct vs. step-wise load was indeed a suitable assumption for Inconel-718.

After loading at the initial stress level for 4 hours, the load is increased every hour by 4% of YS, until fracture occurs. The fracture stress recorded includes the last load increase when the samples fractured during the load increase (marked as 00min in the results). It should be emphasized that the stress values obtained should therefore be regarded as "fracture stress values" and not as "safe-up-to-stress" values.

At each stress level there will be cold creep. This is a time and stress dependent relaxation, which results in plastic strain. The amount of cold creep increases as the stress level gets higher. In order for the stress levels recorded to be as correct as possible, this cold creep was adjusted during testing to keep the engineering stress as constant as possible. As the creep can be very high at the higher stress levels approaching the fracture stress, the creep and following creep adjustment will result in fluctuations in the stress-data curves collected at these stress levels.

Table 4: Initial starting loads and loading procedures for the smooth tensile samples

Alloy variant	Initial load	Subsequent loading schedule
56LH-1-OP	116% of YS, 4hours	4% of YS every hour
56LH-1-Piece-1	116% of YS, 4 hours	4% of YS every hour
56LH-1-Piece-2	108% of YS, 4 hours	4% of YS every hour
P3A01-1900	108% of YS, 4 hours	4% of YS every hour
P3A01-1850A	108% of YS, 4 hours	4% of YS every hour
P3A01-1800	100% of YS, 4 hours	4% of YS every hour

Table 5: Initial starting loads and loading procedures for the notched samples

Alloy variant	Initial load	Subsequent loading schedule
56LH-1-OP	116% of YS	4% of YS every hour until crack initiate
P3A01-1900	108% of YS	4% of YS every hour until crack initiate
P3A01-1800	108% of YS	4% of YS every hour until crack initiate

5.6 SEM observations

After the tensile tests, the samples are observed and studied in SEM. A Zeiss Ultra^{TM} 55, Field-Emission SEM was used for this. All pictures were taken using secondary electron imaging, which means that the pictures formed only consist of topography contrast. An aperture of $30\mu m$ was used together with high current mode. The working distance varied with the height of the samples, but was typically in the range 15-25mm. The acceleration voltage was by default set to 20kV. Since no magnifications larger then 15000 was needed, no effort was made to optimise these parameters, and hence most of them are default values.

Fracture surfaces are examined, and the fracture modes found are identified. Of special interest here is the extent of IG fracture, since this is evidence of hydrogen embrittlement in Inconel-718. Low magnification (50-200X) overview pictures and higher magnification (100-5000X) images of the different fracture modes were taken from all samples. This constitutes more than 200 SEM images, so only a fraction of them will be presented in this thesis. In addition to the fracture surfaces examined, the samples are also examined for secondary cracks. The extent of secondary cracking will be compared between the pre-charged samples and the equivalent hydrogen free samples.

5.7 Hydrogen melt extraction analysis

When each tensile test with a pre-charged sample had been completed, one of the two fracture pieces resulting would be stored in the freezer. After all the tensile tests were completed, one sample from each alloy variant was sent for Hydrogen Melt Extraction Analysis at SINTEF.

In this analysis a small piece approximately 0.5g is cut from the sample. This piece is then placed in a graphite crucible and heated to $1550°C$. Hydrogen and CO_2 are then released from the sample. These gases in addition to dust is picked up by the carrier gas which in this case is Nitrogen. A dust trap, oxidizing agents and a molecular sieve removes dust and CO_2, such that only Hydrogen and Nitrogon are left. The thermal conductivity of the gas flow and a reference gas flow is measured, and the difference between these conductivities produces a signal corresponding to the hydrogen content. The total hydrogen content in the sample can then be calculated from the time integral of the signal. In this analysis the hydrogen content is calculated with an accuracy of 0.001 wppm.

6 Results

6.1 Examination of microstructures in the Optical Microscope

In addition to the microstructure pictures supplied by ATI, new pictures were taken in order to confirm the microstructures received. The OM pictures taken were obtained using a $Leica^{TM} - FEM4F$ optical microscope connected to a camera and a computer. The microstructure images are displayed in figure 21a-21f. The images obtained from the P3A01-1800 and P3A01-1850A alloys where taken at 100X magnification due to their fine microstructure, and are showed in color because the GBs were not visible in their respective gray scale images. The other microstructures were imaged at 10X. These microstructures are displayed as gray scale images for consistency, since the color and contrast varied between the alloys due to variations in the thickness of the anodizing layers. The 56LH-1-OP alloy imaged in figure 21a show some occasional course δ particles, possibly particles formed during casting which survived the homogenization step. This alloy is otherwise δ free and the grain size is relatively course. The 56LH-1-Piece-1 and Piece-2 alloys shown in figure 21c and 21e both contain globular δ particles, which are seen as white spots in the images. The grain size is somewhat finer in the Piece-2 alloy than in the Piece-1 alloy. The P3A01-1900 shown in figure 21b, show a course grain size and is completely δ-free. The P3A01-1850 and 1800 alloys displayed in figure 21d and 21f both show a very fine grain size which can be seen from the calibration scales in the images. Both microstructures contains numerous δ-particles both at the GBs and in the grain interiors. These particles are to be expected, since the precipitation of δ-particles are necessary in the TMP used to achieve these ultra fine grain sizes. The δ-particles are seen in the picture as white spots. In summary, all these microstructure were in accordance with the microstructure images received from ATI-metals.

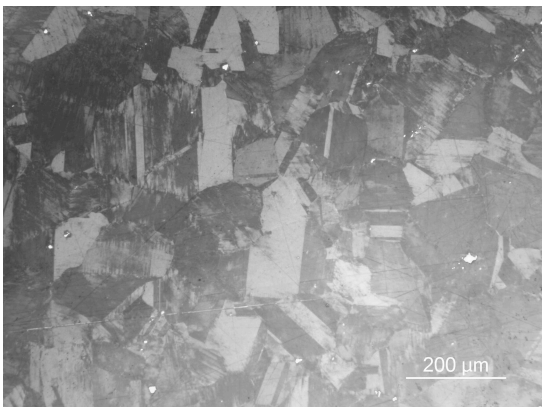

(a) 56LH-1-OP: Standard alloy composition. Course grain size, occasional δ-particles (white).

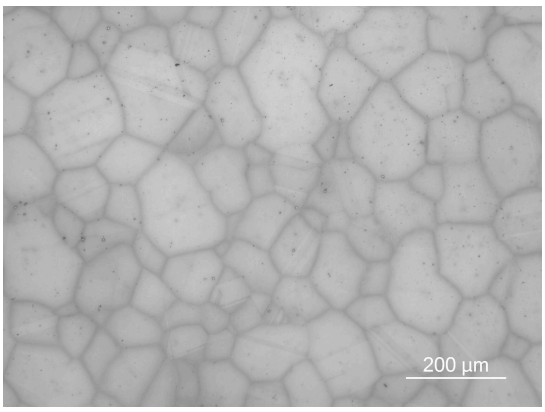

(b) P3A01-1900: Low C/N, high Nb composition. Course grain size, no δ-particles were observed.

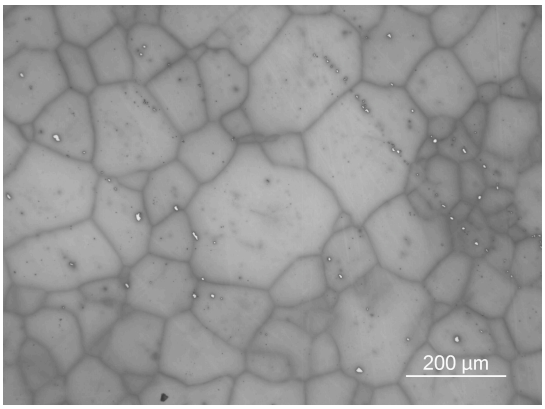

(c) 56LH-1-Piece-1: Standard alloy composition. Course grain size, with globular δ-particles (white).

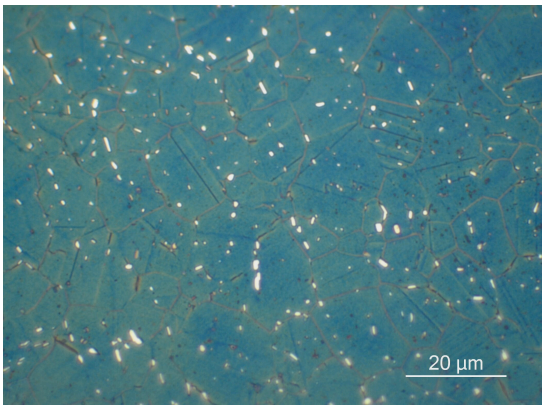

(d) P3A01-1850: Low C/N, high Nb composition. Fine grain size, with globular δ-particles (white).

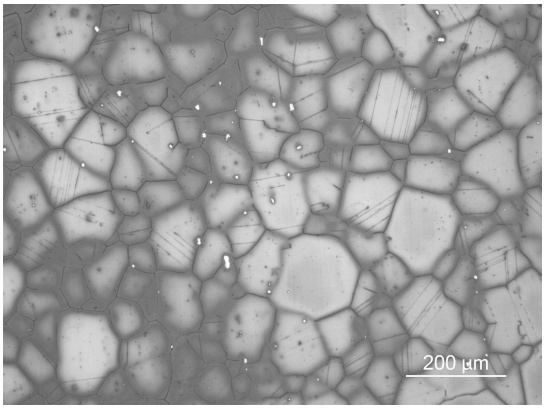

(e) 56LH-1-Piece-2: Standard alloy composition. Medium grain size, with globular δ-particles (white).

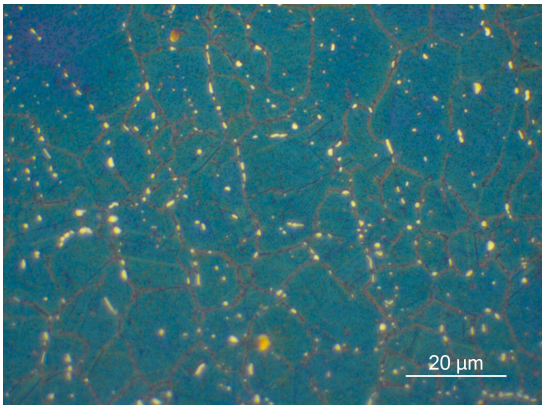

(f) P3A01-1800: Low C/N, high Nb composition. Fine grain size, with globular δ-particles (white).

6.2 Estimation of grain size based on the OM pictures obtained

Based on the microstructure images obtained from the OM samples, the average grain size in each microstructure was calculated according to the plane section method described in ASTM 112e [27]. In this procedure, the number of grains in an image is counted. Grains inside the image are counted as whole grains and grains on the borderline are counted as half grains. Twins are not regarded as grains. The calibration scale given in an image is then used to calculate the true area of the imaged microstructure A_{sample}, which is then divided by the number of grains to yield the average area per grain. The square root of this area is then regarded as the average grain diameter, which implies that all grains are assumed to be squares. This is not the case in reality, but is accepted as a reasonable approximation, as the grains take on various shapes and geometries. The calculation is summarized in formula 19:

$$\overline{D} = \sqrt{\frac{A_{sample}}{N_{inside} + \frac{N_{borderline}}{2}}} \tag{19}$$

Where N_{inside} is number of grains inside the area imaged, $N_{borderline}$ is the number of gains on the edge and A_{sample} is the real image area calculated from the image dimensions and the calibration scale included in the image. This calculation is then repeated for 3 different images from the same alloy. The resulting grain size is then chosen as the average of these. Using this average value the ASTM number G is defined as:

$$N_{ASTM} = 2^{G-1} \tag{20}$$

This shows that the ASTM number G is a logarithmic measure where one number larger means twice as small grains. The number N_{ASTM} is defined as the number

of grains counted per square inch at 100X. The number of grains per square inch at 100x can be calculated according to equation 21:

$$N_{ASTM} = \frac{2.54^2 \cdot 10000^2 \cdot}{100^2 \cdot \overline{D}^2} \tag{21}$$

Where 2.54 is cm/Inch, 10000 is the number of μm/cm and the number 100 accounts for 100X magnification. The grain sizes measured, the average grain sizes and the ASTM numbers calculated is summarized in table 6:

Table 6: Grain sizes calculated according to ASTM 112e.

Alloy	1	2	3	Average grain size	ASTM number
56LH-1-OP	$110.8\mu m$	$93.9\mu m$	$127.2\mu m$	$110.6\mu m$	3.4
56LH-1-Piece-1	$101.4\mu m$	$94.3\mu m$	$96.0\mu m$	$97.2\mu m$	3.8
56LH-1-Piece-2	$78.9\mu m$	$72.6\mu m$	$77.9\mu m$	$76.5\mu m$	4.5
P3A01-1900	$98.6\mu m$	$94.6\mu m$	$91.8\mu m$	$95.0\mu m$	3.8
P3A01-1850A	$11.8\mu m$	$11.3\mu m$	$11.3\mu m$	$11.5\mu m$	9.9
P3A01-1800	$11.8\mu m$	$9.2\mu m$	$11.7\mu m$	$10.9\mu m$	10.0

6.3 Smooth samples: Stress - Time plots

During tensile testing the load cell force was logged every 10s. These data series were used to generate Stress - Time log plots from all the tensile tests. The Stress - time plots are displayed in figure 22 - 33. The y - axis on each plot displays the tensile stress level during testing, and the x - axis show the time in hours. The loading steps were described in the previous Experimental section. As the stress level reach higher levels, extensive creep typically occurs. The adjustment of the creep can be seen as the fluctuations in stress level at each stress level. The fracture stress recorded from each test was defined as the stress level at which the sample was being adjusted to, including the load increase step up to this stress level. This, of course overestimates the fracture strength as many of the samples fractured during a load increase step. Since the overestimation happens for both the pre-charged and hydrogen free sample, a comparison between the two can nevertheless still be done.

Some notes should be included about the plots presented: Sample 4 in figure 22, sample 2 in figure 24 and sample 4 in figure 28 have been removed due to problems with the potensiostatic setup in these in-situ tests. In these tests, the contact with the reference electrode was lost during testing, which resulted in extensive corrosion due to an anodic current supplied by the potensiostat. The loading signal recorded for one of the P3A01-1850A reference samples shown in figure 31 was also lost due to a software crash on one of the computers used. These problems are noted in the figure texts. Only one reference sample from the P3A01-1900 alloy was tested due to a short supply of samples machined from this alloy. This occurred when 4 samples from this alloy were destroyed during pre-charging, following an unexpected Windows update executed by the computer which controlled the potensiostat. A reference sample from this alloy was however tested in the project work preceding this master thesis. This reference sample fractured at 128% of YS, and was included in the fracture strengths summary to add some confidence to the reference fracture strength in this alloy.

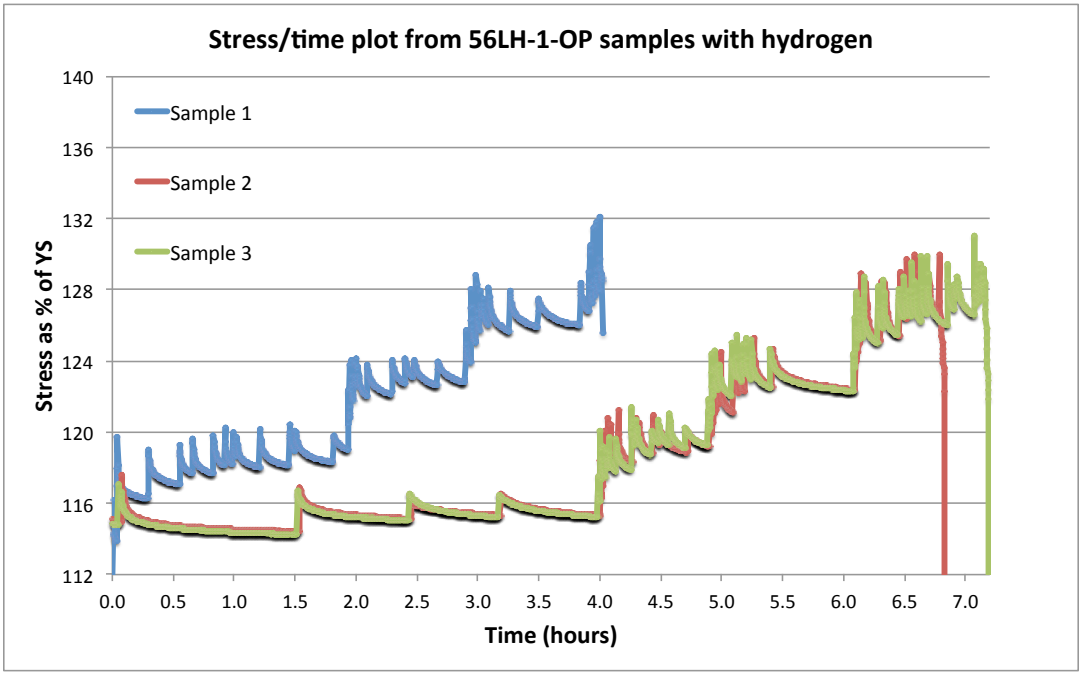

Figure 22: Stress - time plot from the 56LH-1-OP samples pre-charged with hydrogen. Sample 1 was started at 120% of YS, while the other samples were started at 116% of YS. Sample 4 was mistakenly overloaded at the start of the experiment and has been removed.

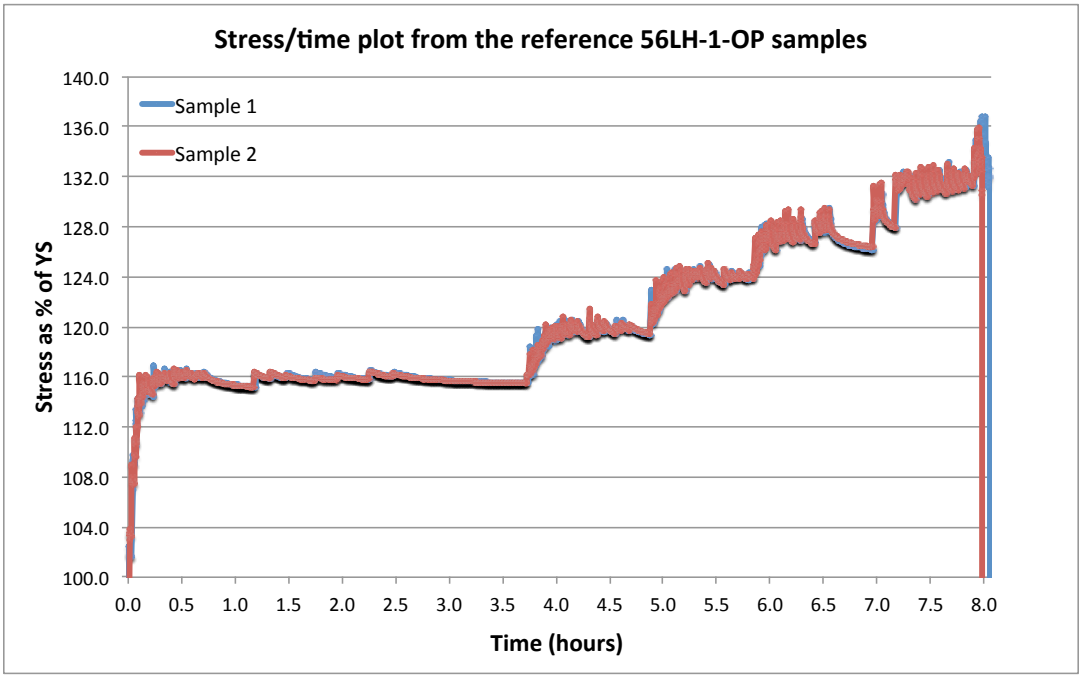

Figure 23: Stress - time plot from the 56LH-1-OP reference samples.

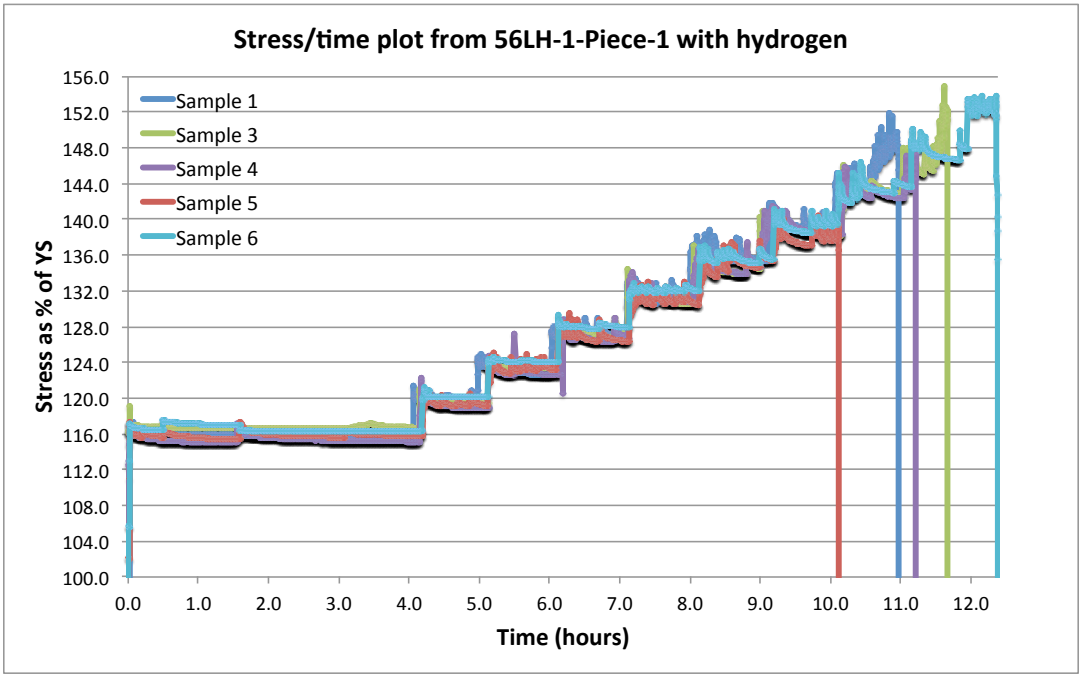

Figure 24: Stress - time plot from the 56LH-1-Piece-1 samples pre-charged with hydrogen. Sample 2 have been removed due to corrosion damage occurring when the reference electrode lost contact. Two extra samples were pre-charged and tested to validate the high fracture strengths recorded.

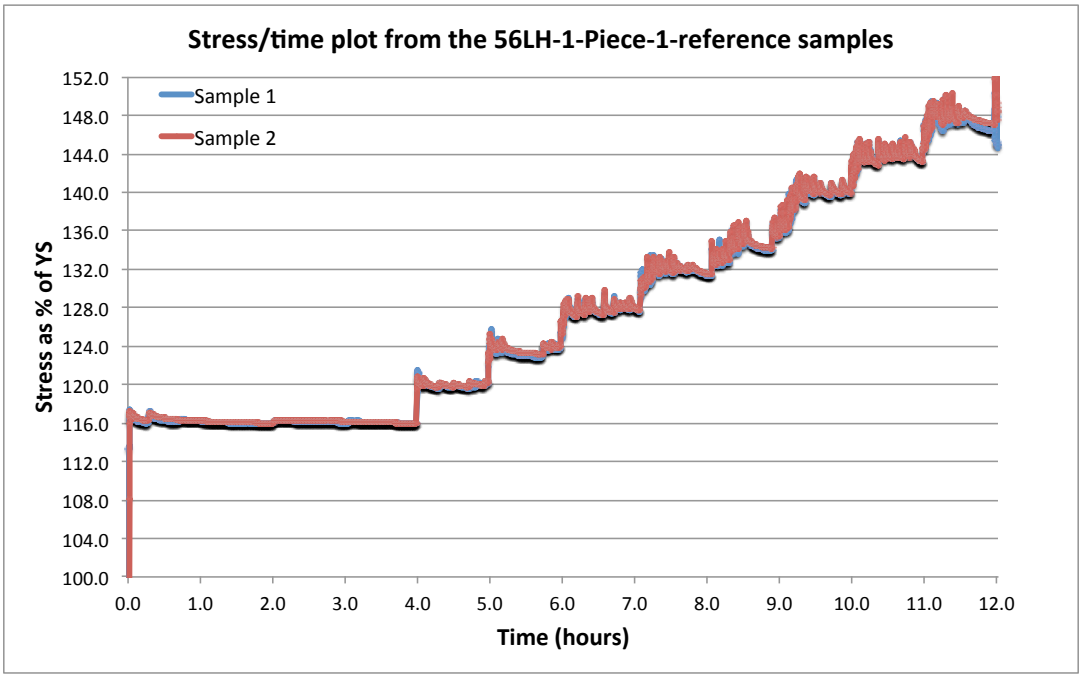

Figure 25: Stress - time plot from the 56LH-1-Piece-1 reference samples. Both samples reached ϵ_{max} at 152% and did not fracture. Both samples are however believed to have been close to fracture because of the extensive necking observed in both samples.

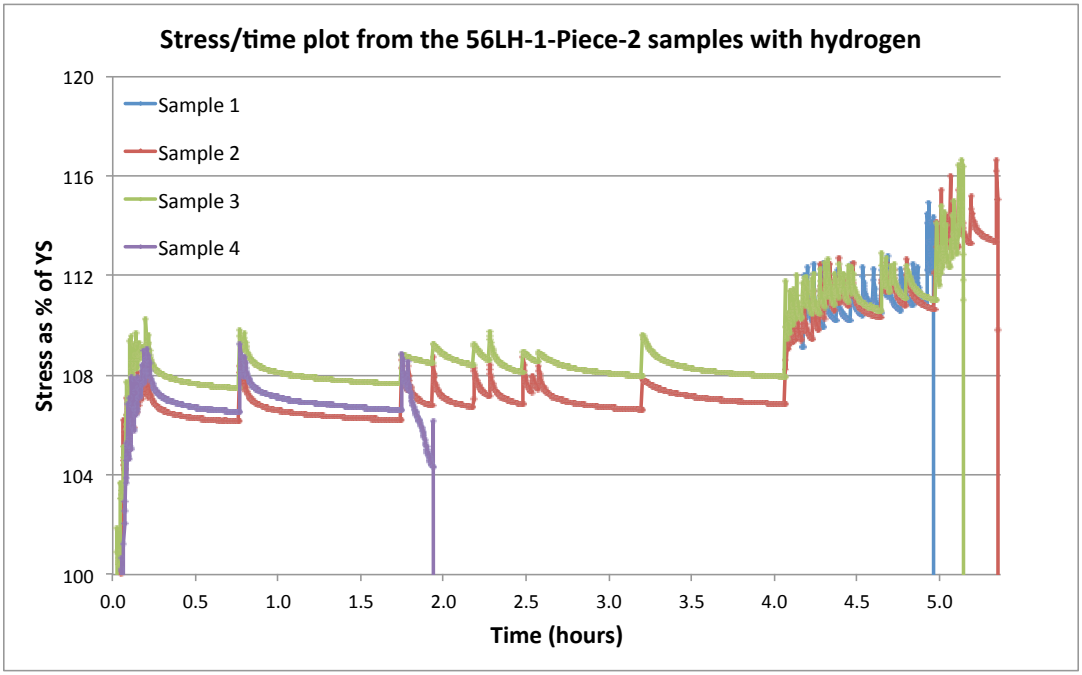

Figure 26: Stress - time plot from the 56LH-1-Piece-2 samples pre-charged with hydrogen. The premature fracture observed in sample 4 was particularly strange, given the consistancy seen in sample 1-3. The hypothesis is that some sort of internal defect have been present in sample 4.

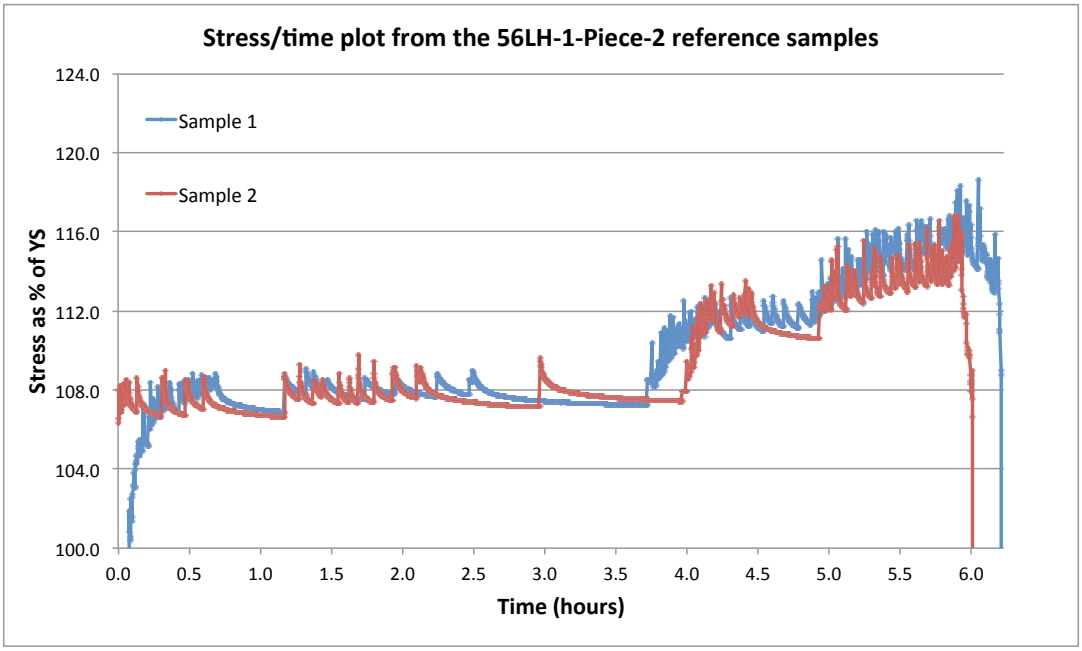

Figure 27: Stress - time plot from the 56LH-1-Piece-2 reference samples.

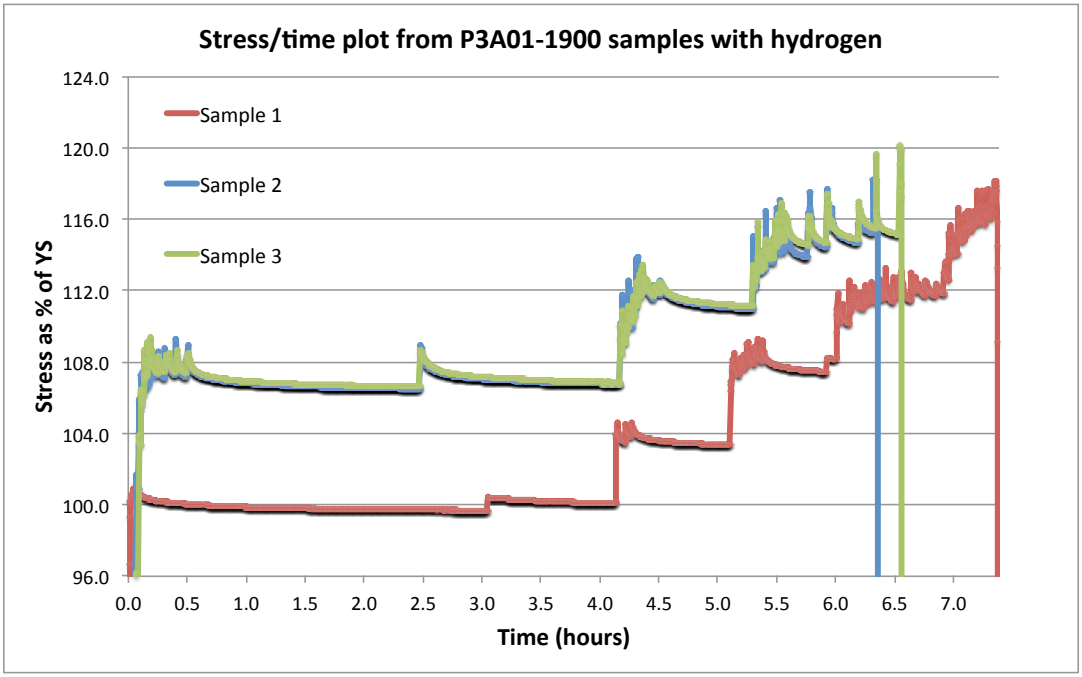

Figure 28: Stress - time plot from the P3A01-1900 samples pre-charged with hydrogen. Sample 1 was started at 100% of YS and sample 2-3 were started at 108% of YS. Sample 4 has been removed due to corrosion damage occurring when the reference electrode lost contact.

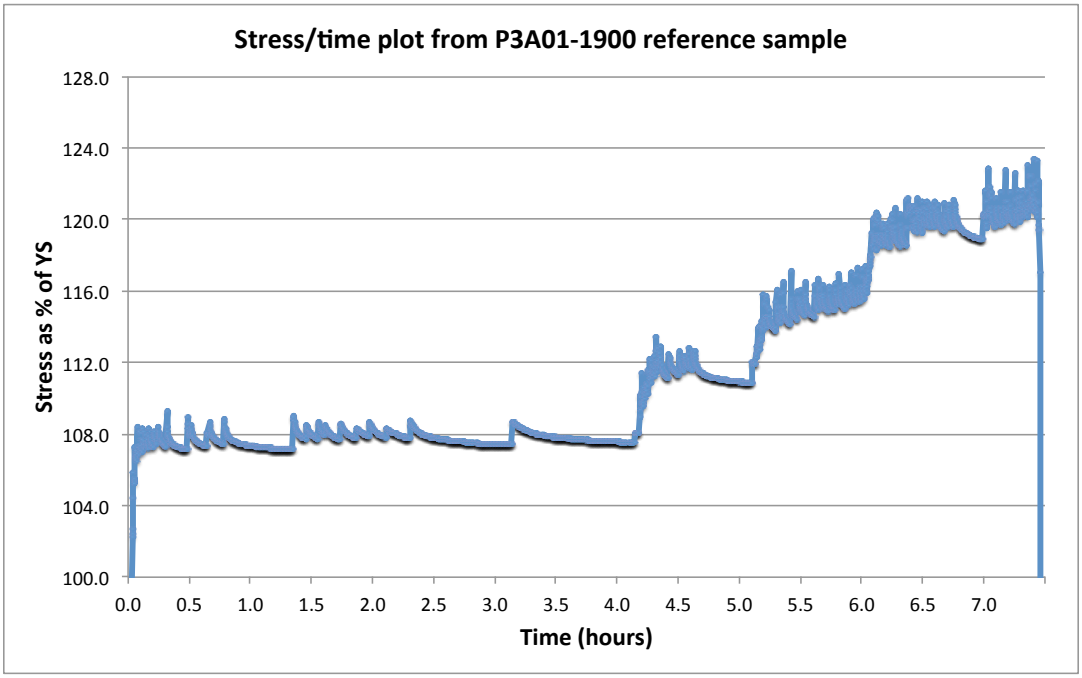

Figure 29: Stress - time plot from the P3A01-1900 reference sample tested. Only one sample was tested in this master thesis due to a shortage of P3A01-1900 samples for reference testing.

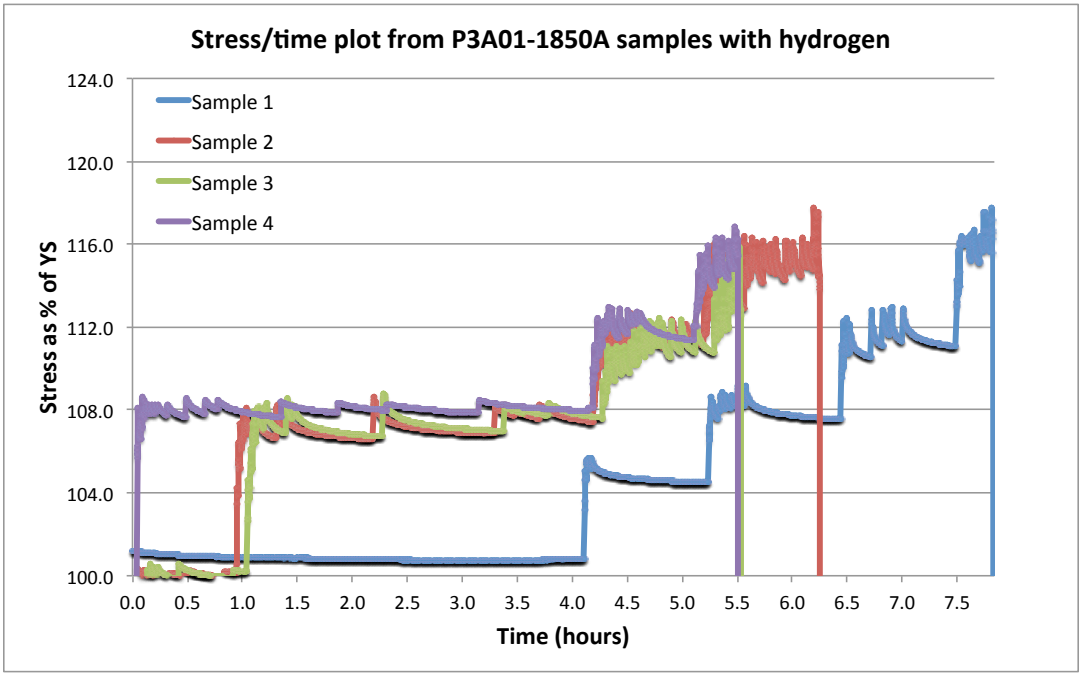

Figure 30: Stress - time plot from the P3A01-1850A samples pre-charged with hydrogen. Sample 1 was started at an initial stress of 100% of YS, while sample 2-4 was tested with an initial stress of 108% of YS. Sample 2 and 3 were mistakenly loaded to 100% of YS the first hour. This was corrected to 108% of YS for the remaining 3 hours of the initial period.

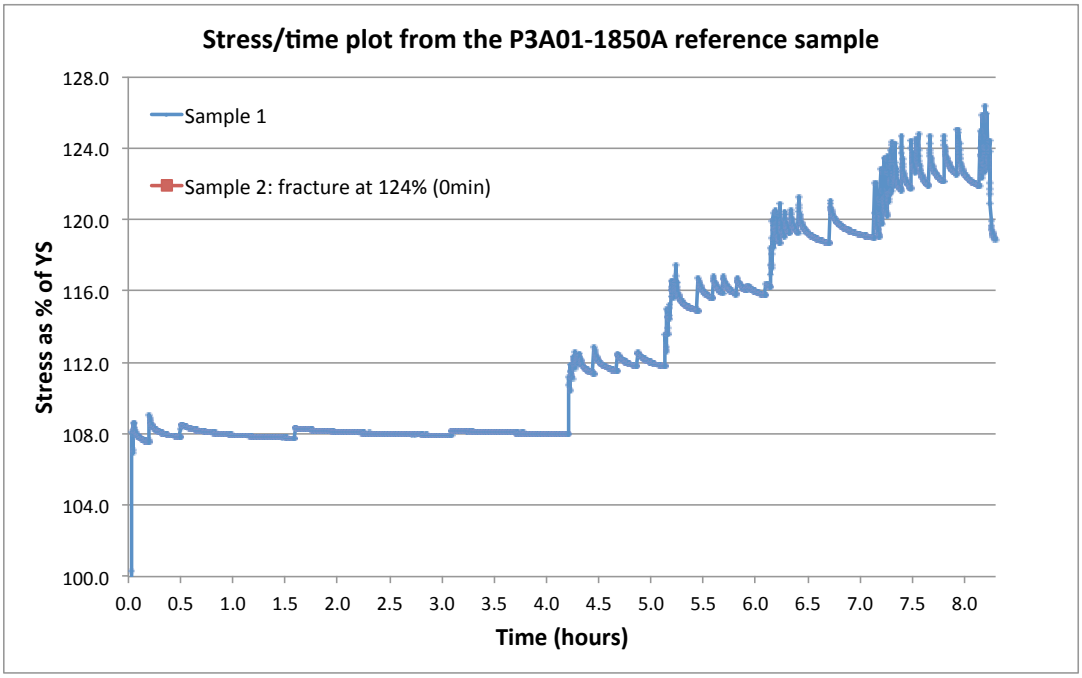

Figure 31: Stress - time plot from the P3A01-1850A reference samples tested. The load signal from sample-2 was lost due to a software crash on the computer. Sample-2 nevertheless fractured when being loaded from 120% to 124% of YS.

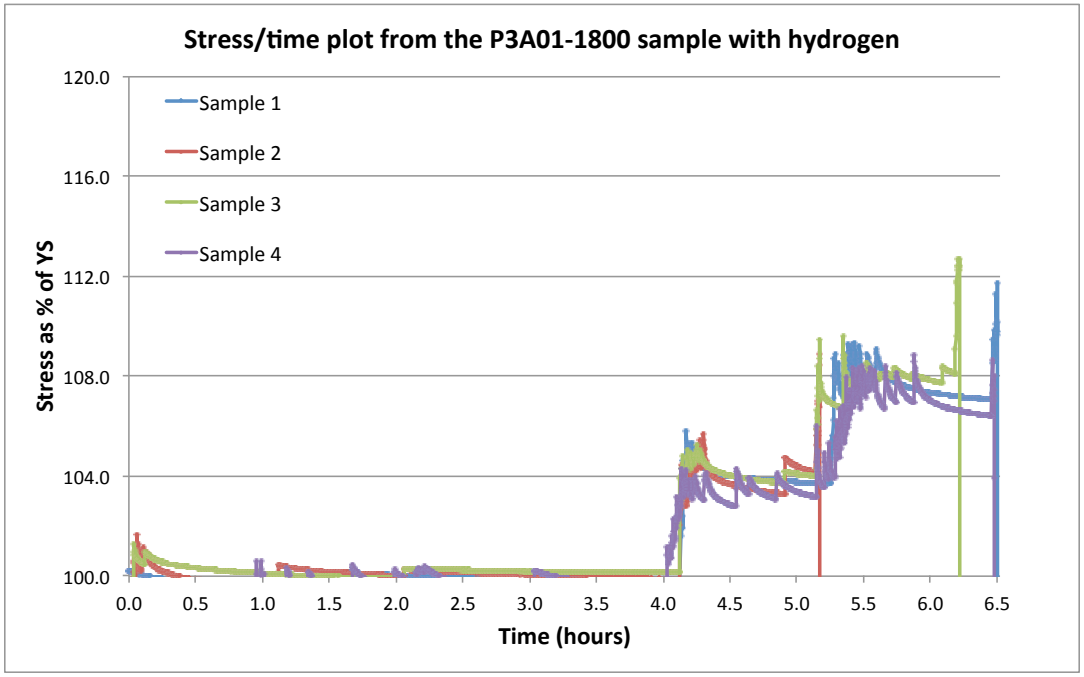

Figure 32: Stress - time plot from the P3A01-1800 samples pre-charged with hydrogen.

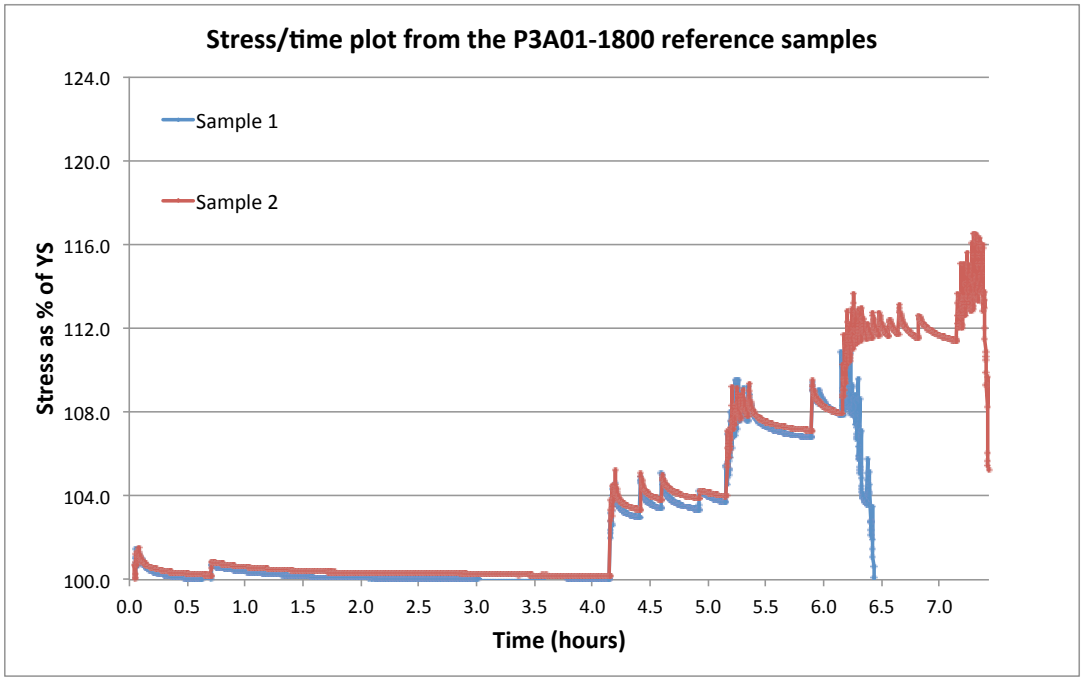

Figure 33: Stress - time plot from the P3A01-1800 reference samples. Its uncertain wether the difference between the fracture stresses in sample-1 and sample-2 is the result of scatter, or if sample-1 contained an internal defect.

6.4 Smooth samples: Tensile fracture strengths

The fracture stresses recorded from the tensile tests are summerized in table 7 and 8. Minutes to fracture are noted in the parenthesis displayed in the tables. (00) means that a sample fractured during the load increase up to the stress level displayed. Samples marked with " - " have been removed since they were destroyed when the reference electrode lost contact. As noted earlier, two extra samples from the 56LH-1-Piece-1 alloy were tested to confirm the high fracture stresses recorded in sample 1 - 4. In all the alloys examined, the pre-charged samples on average fractured at a lower stress compared to the reference samples. The Standard deviation (SD) also appears to be larger amongst the pre-charged samples.

Table 7: Fracture stresses recorded from the hydrogen free reference samples, expressed as % of YS. Minutes to fracture are noted in the parenthesis.

Sample	56LH-1-OP	56LH-1-Piece-1	56LH-1-Piece-2	P3A01-1900	P3A01-1850A	P3A01-1800
1	136% (00)	$\geq$152%[1]	124% (60)	124% (00)	124% (52)	112% (00)
2	136% (00)	$\geq$152%[1]	120% (00)	128%[2]	124% (00)	116% (55)
Average	**136%**	**$\geq$152%[1]**	**122%**	**126%**	**124%**	**114%**
SD	**0.0%**	**0.0%**	**2.8%**	**2.8%**	**0.0%**	**2.8%**

Table 8: Fracture stresses recorded from pre-charged samples expressed as % of YS. Minutes to fracture are noted in the parenthesis.

Sample	56LH-1-OP	56LH-1-Piece-1	56LH-1-Piece-2	P3A01-1900	P3A01-1850A	P3A01-1800
1	132% (11)	148% (26)	112% (58)	116% (17)	116% (21)	112% (02)
2	128% (22)	-	116% (20)	120% (00)	120% (00)	108% (00)
3	132% (07)	152% (05)	116% (15)	120% (00)	116% (00)	112% (01)
4	-	148% (00)	108% (120)	-	116% (24)	112% (00)
5		140% (50)				
6		152% (26)				
Average	**130.7%**	**148.0%**	**113.0%**	**118.7%**	**117.0%**	**111.0%**
SD	**2.3%**	**2.3%**	**3.8%**	**2.3%**	**2.0%**	**2.0%**

[1]The 56LH-1-Piece-1 reference samples reached the maximum elongation allowed by the load cell: ϵ_{max}
[2]This P3A01-1900 reference sample was included from the project work.

The losses in fracture strengths expressed as % of YS are summarized in table 9. It can be seen that the loss of fracture strength is rather moderate, at around 5 - 9 % of YS. This is still a significant loss though. No pre-charged samples fractured below YS. Furthermore, no significant trend across the different microstructures and compositions can be seen, given that there is a 2-3% standard deviation.

One of the pre-charged samples from 56LH-1-Piece-2 and one of the reference samples from P3A01-1800 fractured prematurely at a much lower stress levels than their respective peers. These values distort the values of fracture strength losses measured from these series, and results in a high loss of 9% YS for 56LH-1-Piece-2 and a low loss of 3% YS for P3A01-1800. Given that a high scatter in fracture strengths is unexpected especially in the reference samples, it is not unlikely that at least one of these values may have been the result of some sort of defect in the sample. If these premature fractures were indeed the result of internal defects of some sorts, it is clear that these values should have been excluded. Table 10 show the losses in fracture strengths if these two samples were excluded. It is seen that all the alloy variants now exhibit a rather uniform loss of around 5 -7 % of YS. Although the 5 - 7% loss of fracture strength is significant, there is still no significant trend across the microstructures and compositions. Both table 9 and 10 indicate that the fracture strength loss seen in relation to hydrogen embrittlement is only weakly if not independent of composition and microstructure in Inconel-718.

Table 9: Average loss of fracture stress seen in the pre-charged samples relative to the hydrogen free samples. The losses are expressed as % of YS loss for each alloy.

	56LH-1-OP	56LH-1-Piece-1	56LH-1-Piece-2	P3A01-1900	P3A01-1850A	P3A01-1800
Loss	**5.3 %**	**$\geq$ 4.0%**	**9.0%**	**7.3%**	**7.0%**	**3.0%**

Table 10: Average loss of fracture stress, where 56LH-1-Piece-2(Pre-charged-sample-4) and P3A01-1800(Reference-sample-1) have been excluded

	56LH-1-OP	56LH-1-Piece-1	56LH-1-Piece-2	P3A01-1900	P3A01-1850A	P3A01-1800
Loss	**5.3 %**	**$\geq$ 4.0%**	**7.3%**	**7.3%**	**7.0%**	**5.0%**

6.5 Loss of Reduction of Area

All the sample cross sections were measured before and after tensile testing. After fracture the fracture areas were still roughly rectangular, which meant that the fracture areas could be measured with reasonable accuracy by measuring the length and width of the fractured surface. The percent wise reduction of area (RA) was then calculated according to equation 22:

$$RA = 100 \cdot \frac{A_{before} - A_{after}}{A_{before}} \tag{22}$$

Where A_{before} and A_{after} are the cross section areas measured before and after the tensile test. This procedure was repeated both for the tensile test samples with hydrogen pre-charging, and those without. The percent wise loss of RA in the pre-charged samples caused by hydrogen was calculated according to equation 23:

$$RA_{loss} = 100 \cdot \frac{RA_0 - RA_H}{RA_0} \tag{23}$$

Where RA_0 and RA_H are the average RA values calculated for the tensile test samples without and with hydrogen respectively. This number can then be used as an indicator of the relative loss in ductility associated with hydrogen pre-charging. The RA_{loss} calculations are summarized in table 11, 12 and 13.

Table 11: RA_0 values measured from the samples without hydrogen pre-charging

Sample	56LH-1-OP	56LH-1-Piece-1	56LH-1-Piece-2	P3A01-1900	P3A01-1850A	P3A01-1800
1	29.5%	≥32.6%[1]	34.2%	31.0%	31.8%	33.9%
2	27.1%	≥30.1%[1]	35.0%	-	34.9%	38.5%
Average RA_0	**28.3%**	**≥31.4%**[1]	**34.6%**	**31.0%**	**33.4%**	**31.2%**
SD	**1.7%**	**1.7%**	**0.6%**	**-**	**2.2%**	**3.9%**

[1]The reference samples from 56LH-1-PIece-1 reached the maximum elongation of the load cell ϵ_{max} and did not fracture.

Table 12: RA_H values measured from the samples with hydrogen pre-charging

Sample	56LH-1-OP	56LH-1-Piece-1	56LH-1-Piece-2	P3A01-1900	P3A01-1850A	P3A01-1800
1	23.3%	17.3%	16.4%	21.8%	7.1%	3.3%
2	18.4%	-	9.6%	22.7%	16.0%	8.8%
3	20.9%	21.5%	11.5%	21.7%	17.6%	4.5%
4	-	28.1%	9.7%	-	10.1%	13.1%
5		18.0%				
6		14.5%				
Average RA_H	**20.9%**	**19.9%**	**11.8%**	**22.1%**	**12.7%**	**7.4%**
SD	**2.5%**	**5.2%**	**3.2%**	**0.6%**	**4.9%**	**4.5%**

Table 13: RA_{loss} values calculated from the average RA_0 and RA_H values

	56LH-1-OP	56LH-1-Piece-1	56LH-1-Piece-2	P3A01-1900	P3A01-1850A	P3A01-1800
RA_{loss} values	**26.3%**	**$\geq$36.6%**	**65.9%**	**28.9%**	**62.0%**	**76.3%**

It is seen that all the alloy variants exhibit a large relative loss of reduction of area when hydrogen was present. Some alloys even lost as much as 70% of RA. Furthermore, its noted that finer grain sizes seen in the 56LH-1-Piece-2, P3A01-1850A and P3A01-1800 variants seems to be correlated with larger loss of RA. This may indicate that finer grains make the Inconel-718 alloy more susceptible to hydrogen embrittlement, perhaps through increased GB diffusion. A scatter plot is included in figure 34, showing the RA values measured from the pre-charged and hydrogen free samples. The maximum and minimum values measured are indicated by the error bars. This plot shows that although there is a large scatter amongst some of the alloy variants, the correlation between fine grains and large RA_{loss} still persists. The RA_{loss} values calculated have been plotted in figure 35. The grain sizes in the alloy variants have been included as well, illustrateing the trend.

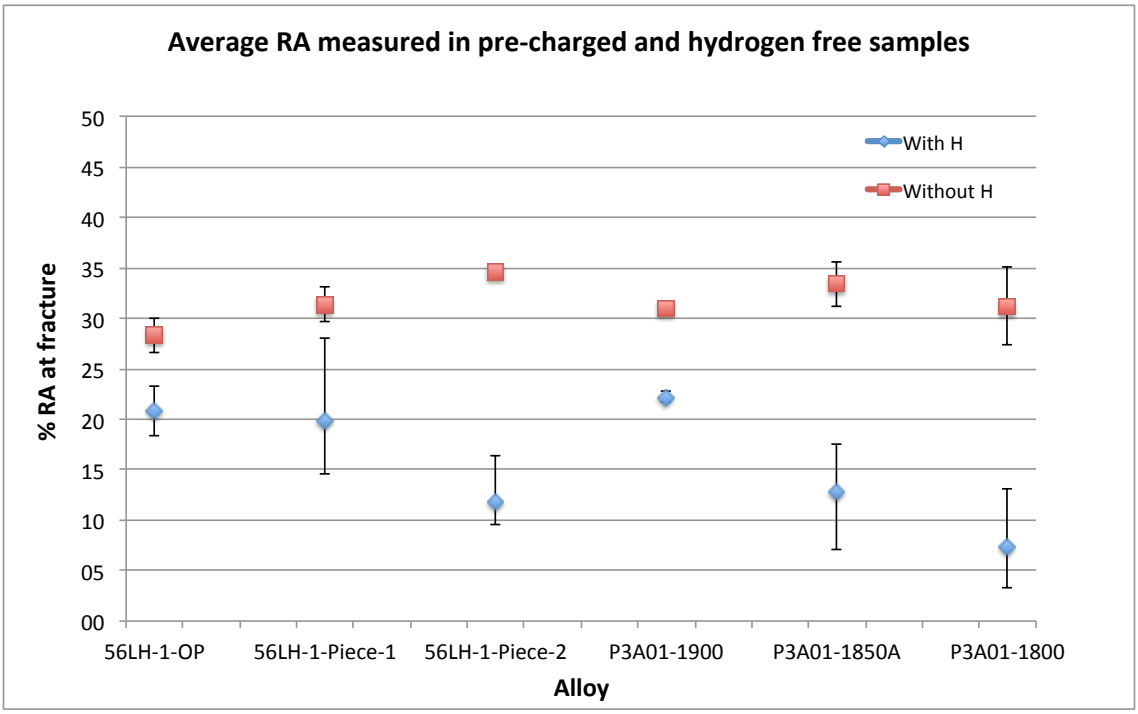

Figure 34: A scatter plot comparing the RA for all the alloys with and without hydrogen. The values plotted are averages, with min and max values indicated by the error bars.

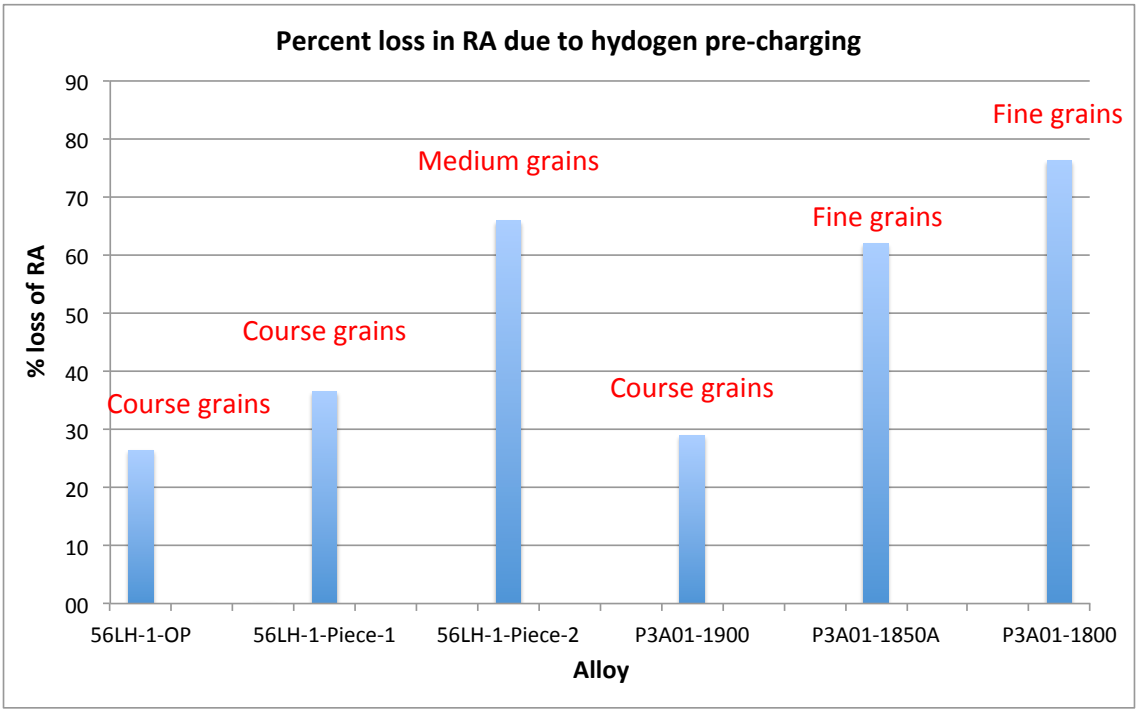

Figure 35: A comparison between the different alloys showing percentage loss of RA due to hydrogen pre-charging.

6.6 Loss of Elongation (ϵ)

The elongation in all the samples were measured as well. This was done by measuring the gauge length before testing, and the gauge length of the two fractured pieces after fracture. The two pieces were measured on the same side and from the same point on the fracture surfaces. The elongation is calculated according to equation 24.

$$\epsilon = \frac{L_{part-1} + L_{part-2} - L_0}{L_0} \tag{24}$$

The percent wise loss of elongation due to hydrogen pre-charging can then calculated according to equation 25.

$$\epsilon_{loss} = 100 \cdot \frac{\epsilon_0 - \epsilon_H}{\epsilon_0} \tag{25}$$

The elongation calculations are summarized in table 14, 15 and 16. A large loss of elongation (ϵ_{loss}) can be seen across all the alloy variants tested. The ϵ_{loss} values seem to be correlated with the grain sizes in the variants as well. This is the same trend that was observed for the RA values. The 56LH-1-Piece-2, P3A01-1850A and P3A01-1800 which have the finest grain sizes, exhibit losses of 65.9%, 62.0% and 76.3% respectively. There appears to be higher standard deviations in the elongation measurements compared to the RA measurements. This may be caused by different measuring errors associated with the two types of ductility measurements. A scatter plot from the elongations measured is shown in figure 36, where the error bars indicate the minimum and maximum values measured in each series. The loss of elongation is displayed in figure 37. The grain sizes have been noted in the figure, illustrating the trend of higher ductility loss in smaller grained variants.

Table 14: ϵ_0 values measured for the samples without hydrogen pre-charging

Sample	56LH-1-OP	56LH-1-Piece-1	56LH-1-Piece-2	P3A01-1900	P3A01-1850A	P3A01-1800
1	30.1%	29.5%	24.0%	29.9%	16.0%	18.3%
2	29.9%	29.3%	25.3%	-	20.0%	19.0%
Average ϵ_0	**30.0%**	**29.4%**	**24.6%**	**29.9%**	**18.0%**	**18.7%**
SD	**0.1%**	**0.1%**	**0.9%**	**-**	**2.9%**	**0.5%**

Table 15: ϵ_H values measured for the samples with hydrogen pre-charging

Sample	56LH-1-OP	56LH-1-Piece-1	56LH-1-Piece-2	P3A01-1900	P3A01-1850A	P3A01-1800
1	15.8%	13.4%	11.2%	14.5%	5.8%	2.2%
2	15.6%	14.0%	9.6%	16.3%	12.4%	4.5%
3	14.9%	8.4%	8.9%	15.8%	11.1%	4.2%
4	-	28.1%	4.3%	-	3.9%	8.3%
5		16.2%				
6		11.5%				
Average ϵ_H	**15.4%**	**17.6%**	**8.5%**	**15.5%**	**8.3%**	**4.8%**
SD	**0.5%**	**6.3%**	**3.0%**	**0.9%**	**4.1%**	**2.5%**

Table 16: ϵ_{loss} values calculated from the average RA_0 and RA_H values

	56LH-1-OP	56LH-1-Piece-1	56LH-1-Piece-2	P3A01-1900	P3A01-1850A	P3A01-1800
ϵ_{loss} values	**26.3%**	**40.1%**	**65.9%**	**28.9%**	**62.0%**	**76.3%**

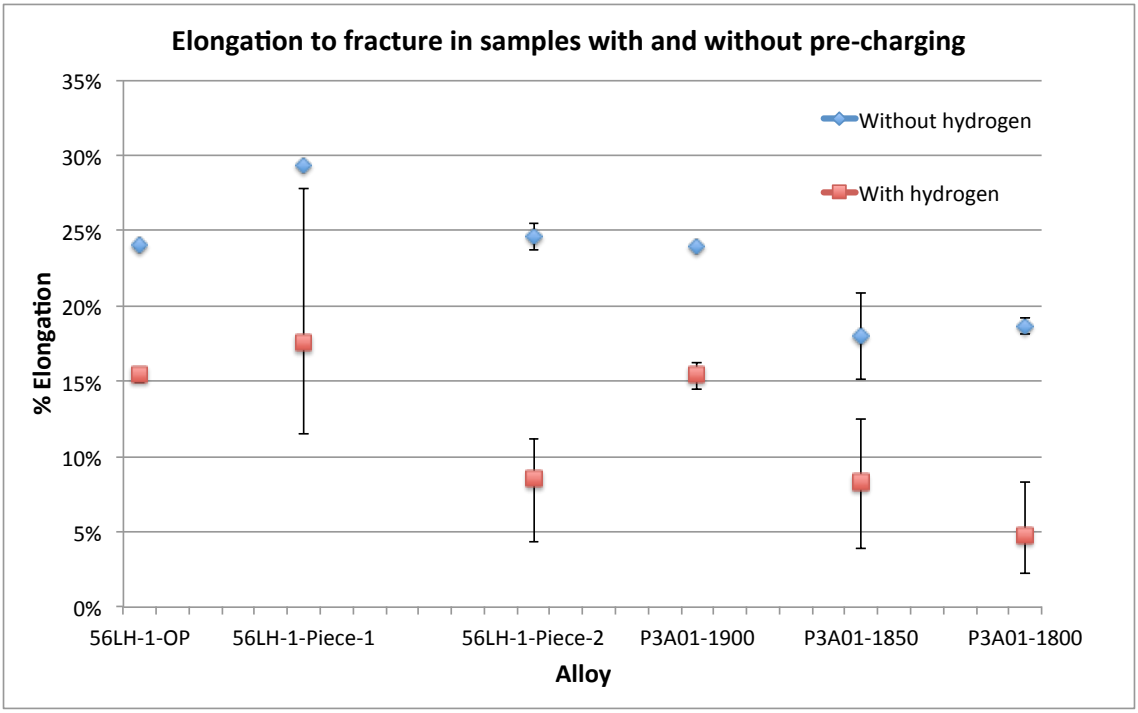

Figure 36: A scatter plot comparing the elongation to fracture for all the alloys with and without hydrogen. The values plotted are averages, with min and max values indicated by the error bars.

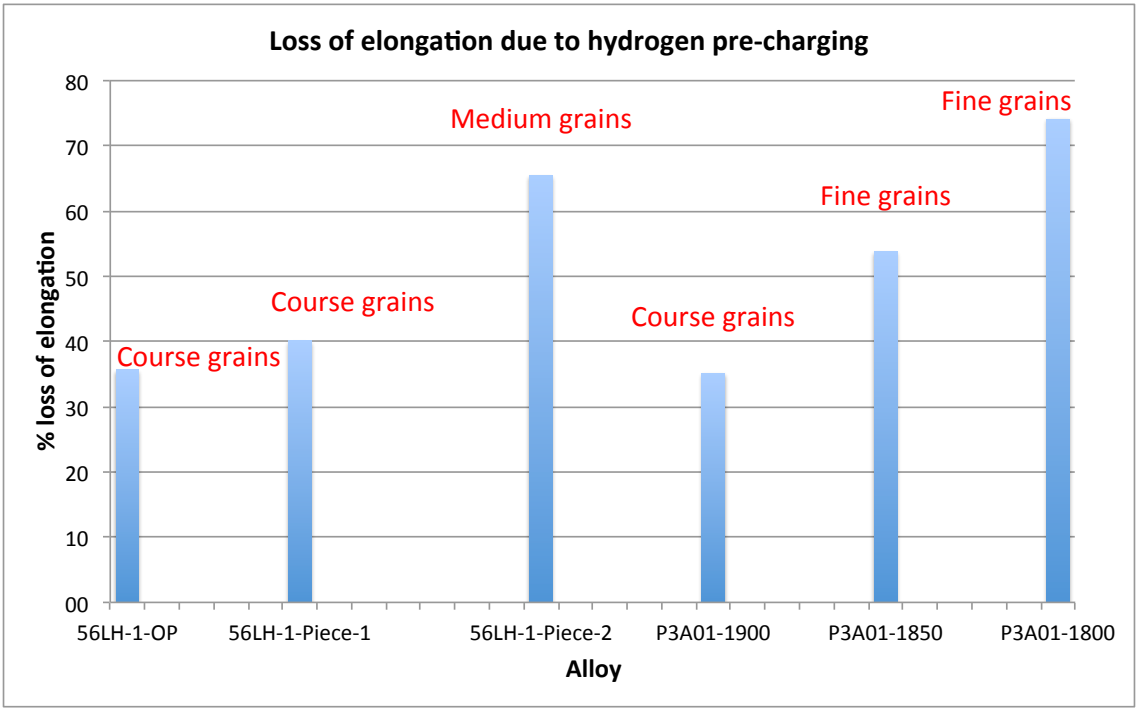

Figure 37: A comparison between the different alloys showing percentage loss of elongation (ϵ_{loss}) due to hydrogen pre-charging.

6.7 Notched samples - Tensile results

The stress - time plots from the notched samples are shown in figure 38 and 39. The purpose of these tests was to obtain time-lapse videos of the initiation and propagation of the critical crack under CP in synthetic saltwater. The long constant load segments of the stress-time plots are therefore the result of the effort to film a crack propagating at a constant load. The time-lapse videos obtained are included in the electronic attachments submitted together with this master thesis. In both the 56LH-1-OP sample and the P3A01-1900 sample, the critical crack was filmed from initiation to failure. Hydrogen bubbles were seen evolving from the main crack and nearby secondary cracks, as new active surface areas were exposed. In the initial period of the time-lapse movies, the main crack also seemed to propagate preferentially at the GBs. In the latter more rapid stage of crack propagation this changed, and trans granular crack propagation was seen as well. The P3A01-1800 sample fractured before the critical crack could be identified. The movie from this sample is nevertheless included in the electronic attachments as well. The tensile fracture strengths recorded from the notched tensile tests are summarized in table 17, where the fracture stresses are given as % of YS. All the stresses are given as engineering stresses, calculated across the reduced area at the notch.

Table 17: Tensile fracture strengths recorded from the notched samples, presented as % of YS

	56LH-1-OP	P3A01-1900	P3A01-1800
Without H	142%	132%	128 %
With H	128%	122%	116%

A few points should be noted from the fracture strengths recorded. The first is that the unaffected fracture strengths measured in the reference samples are much higher than in the smooth reference samples tested previously. Proposed explanations for this are:

- The size effect: The deformed area in the notch is much smaller than the entire gauge length deformed in the smooth samples. This results in a lower statistical risk of strength limiting defects in the notched samples.
- A notch with 0.6mm depth and a tip radius of 0.3mm is not very sharp. This means that the reduction in fracture stress caused by the stress intensification is small.
- The larger cross sections on both sides of the notch resist and limit the poisson contraction in the notch. This means that the cross section at the notch will contract less than it otherwise had if the entire gauge length had the same cross section as the notch. The difference between engineering and true stress therefore becomes less and a higher engineering fracture stress is recorded as a result.

The loss of fracture strengths calculated from the notched samples are also larger. This happens as the pre-charged samples fractured at the same stress as the pre-charged smooth samples, while the reference samples exhibited a higher fracture strength relative to the smooth samples. Some proposed explanations for this are:

- The reduced elongation and RA occuring in pre-charged samples, leaves less room for the effect of the poisson contraction restriction caused by the surrounding cross sections. This prevents the pre-charged samples from achieving the same degree of "notch-strengthening" as the reference notched samples.
- The presence of a stress intensifier results in an increased transportation of hydrogen to the crack tip, due to the presence of a stress gradient. This may result a larger reduction of fracture strength in the notched samples, compared with the pre-charged smooth samples. Since the notch is not particularly sharp, its not certain if this is a significant effect or not.

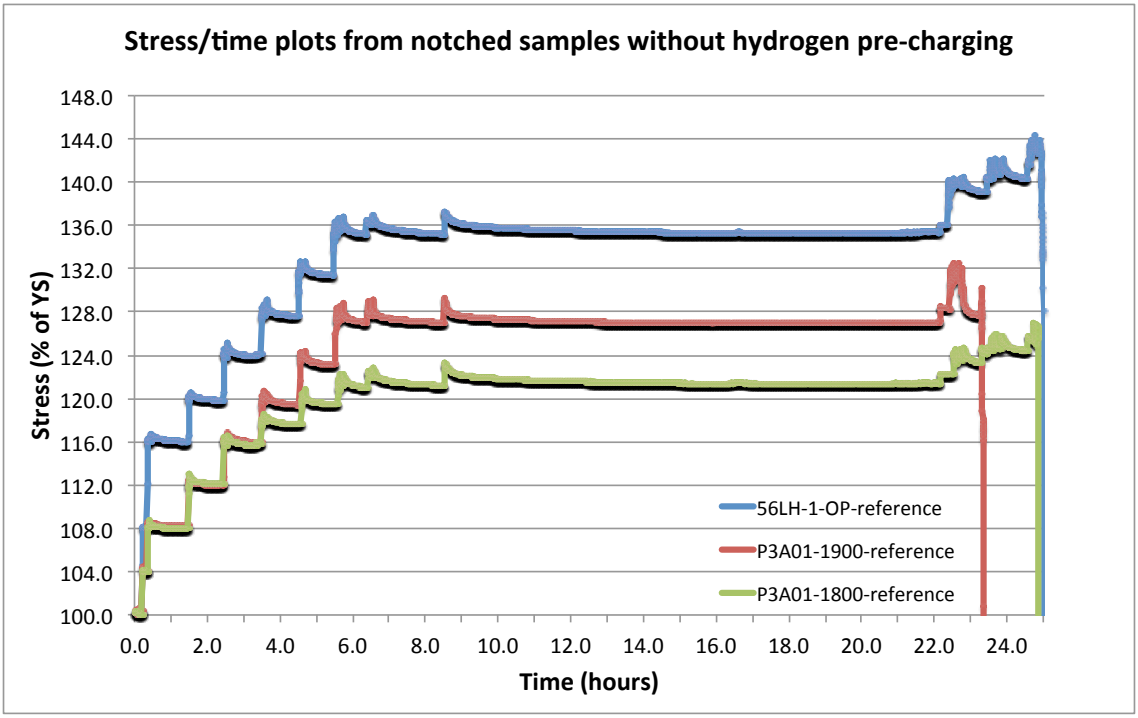

Figure 38: Stress time plots from the tensile tests performed on notched samples without hydrogen pre-charging.

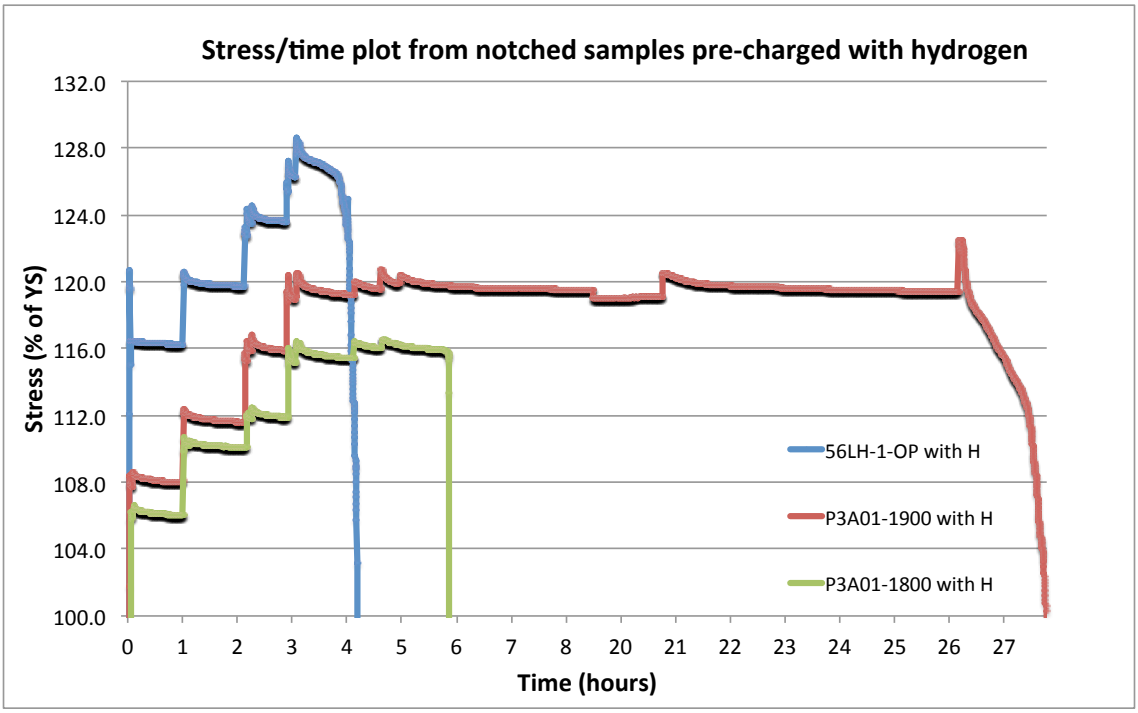

Figure 39: Stress time plots from the tensile tests performed on notched samples with hydrogen pre-charging.

6.8 Other tensile results

Sample-4 from the 56LH-1-OP alloy was accidentally loaded far above the intended initial load during the initial loading step. A stress - time plot from this test is displayed in figure 40. The overload happened as result of a calculation error in estimating the load corresponding to the right stress level intended. The stress applied during this overload was even higher than the fracture strengths measured from the other pre-charged samples from this alloy (stress peak at 140% of YS vs. fracture at approx. 128% for the remaining samples). The test was nevertheless completed and fracture occurred when the sample reached 144% of YS.

Despite the accidental and uncontrolled nature of this test, the resulting stress strain curves give rise to some interesting indications with respect to both hydrogen embrittlement and creep in Inconel-718:

The first thing that is observed from the graph is that no creep followed after the stress was corrected. This results from the strain hardening occurring during the overloading step, which effectively results in an increase of of the tensile yield stress according to the Bauschinger effect [3]. As cold creep occurs predominately above the yield stress, this prevents creep from occurring until the previous loading peak is approached again. This is seen in figure 40 as creep first starts to reemerge when the sample reach 140% of YS. Creep have been concluded to be a prerequisite for HISC to evolve in SDSS [30,41]. The drastically increased fracture strength obtained after this accidental overload raises the question of wether this might be the case for Inconel-718 as well. In should be emphasized that further research is needed to confirm this, as the accidental overload test is no definitive proof in itself.

However, should future testing show that work hardening prevents hydrogen embrittlement of Inconel-718 through the elimination of creep, it will open up the possibility of new preventive measures against hydrogen embrittlement in Inconel-718. One such measure could be to overload components slightly before service, the effect of which is called "shakedown". Again, it should be emphasized that the results derived from this test should only be regarded as an indication, and that further research is needed to document the proposed effect.

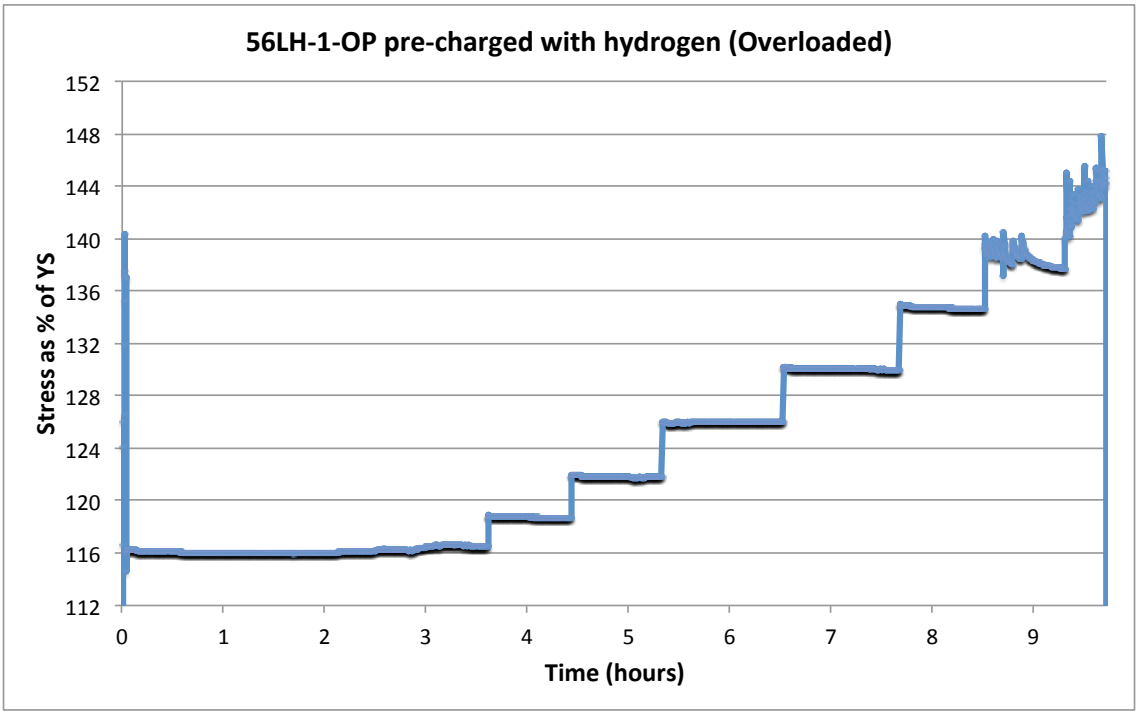

Figure 40: Stress - time plot from 56LH-1-OP pre-charged with hydrogen and overloaded at start.

6.9 Cathodic current measurements during tensile testing

During the in-situ tensile testing, the Cathodic Current (CC) was monitored and logged electronically by the $Gamary^{TM}$ software on the computer. The intension for these CC measurements was to correlate initiations of cracks on the sample surface with peaks in the CC resulting from exposure of new active metal surfaces in the cracks. At first this seemed promising. Figure 41 shows the CC curve obtained from the two first hours of tensile testing of alloy P3A01-1900 pre-charged with hydrogen (Sample-2). At first it was though that the most significant peaks observed (marked with red circles) in the CC were related to the initiation of new cracks. At this stress however (108% of YS), no cracks were observed. Closer examination of the experimental setup however, revealed that these peaks in the CC were instead related to the re-injection of new electrolyte following a leakage in the electrolyte chamber. The large CC peaks observed, where therefore caused by the increase in convection resulting from these refilling procedures. To demonstrate this, electrolyte was injected deliberately next to the sample surface, which resulted in the large peak seen in the end of the graph (marked with green).

Further effort was therefore made to avoid leakage and to prevent the need for refilling the electrolyte. This was done by using a plastic film wrapped around the sample areas in contact with the PC chamber, which proved partly effective. Most of the tensile tests avoided leakage, while leakage still persisted in others. At larger strains, following significant poisson contraction of the sample cross sections, most tensile tests encountered some leakage. This was particularly challenging to the CC observations, as the leakage of electrolyte was often associated with a jump in CC. This happens when the sample areas previously in contact with the PC chamber, become exposed to the electrolyte. Figure 42 show a CC curve resulting from one of the tests where no leakage occurred. Following the same logic, efforts were made to link these peaks to crack initiations. These peaks (red) turned out to be the resulting convection caused when larger hydrogen bubbles initially stuck on the sample sur-

face, grew larger and gave way. This resulted in dragging of the electrolyte around the bubbles. As seen from figure 42, these effects are fairly periodically, which is to be expected when bubbles continuously build up and give away from the same hydrogen evolution sites on the sample. The CC increase seen in the start of the graph is associated with the initial load-up of the sample to its first initial starting load (green). After these false peaks had been accounted for, only a steady state CC with some minor fluctuation was left. It was therefore concluded that the CC increase associated with a crack initiation was to small to be detected in the experimental setup used.

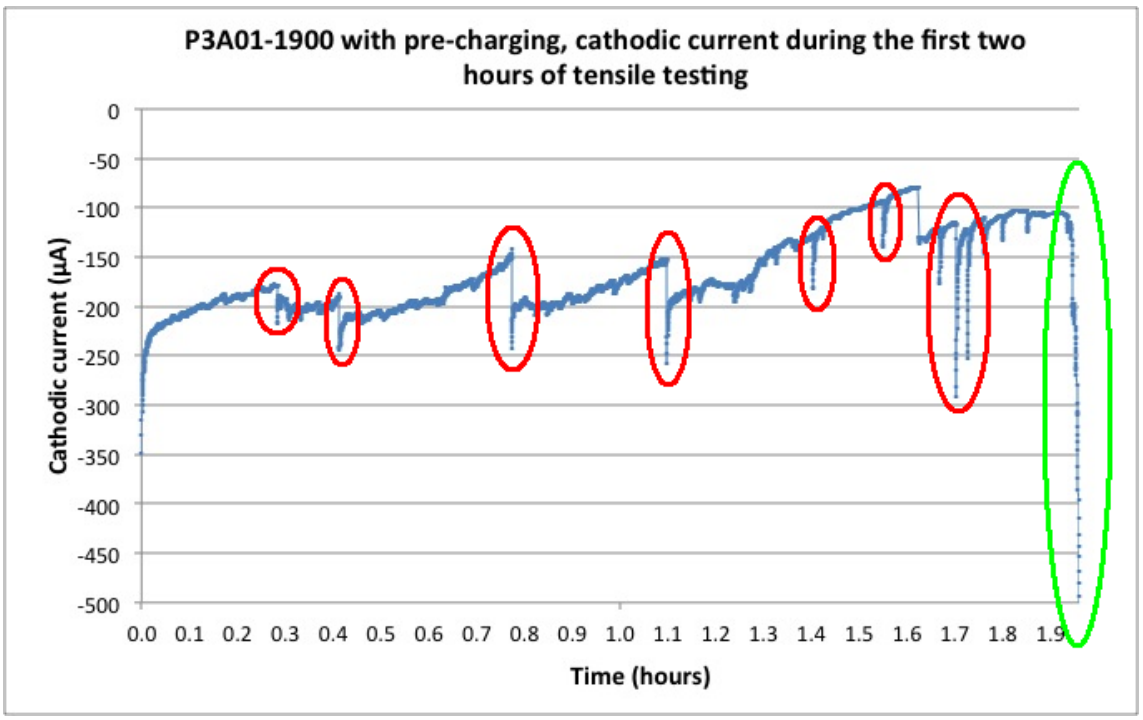

Figure 41: A plot showing the cathodic current recorded during the two initial hours of tensile testing of P3A01-1900 with pre-charging (Sample-2). Leakage and refillings are marked with red.

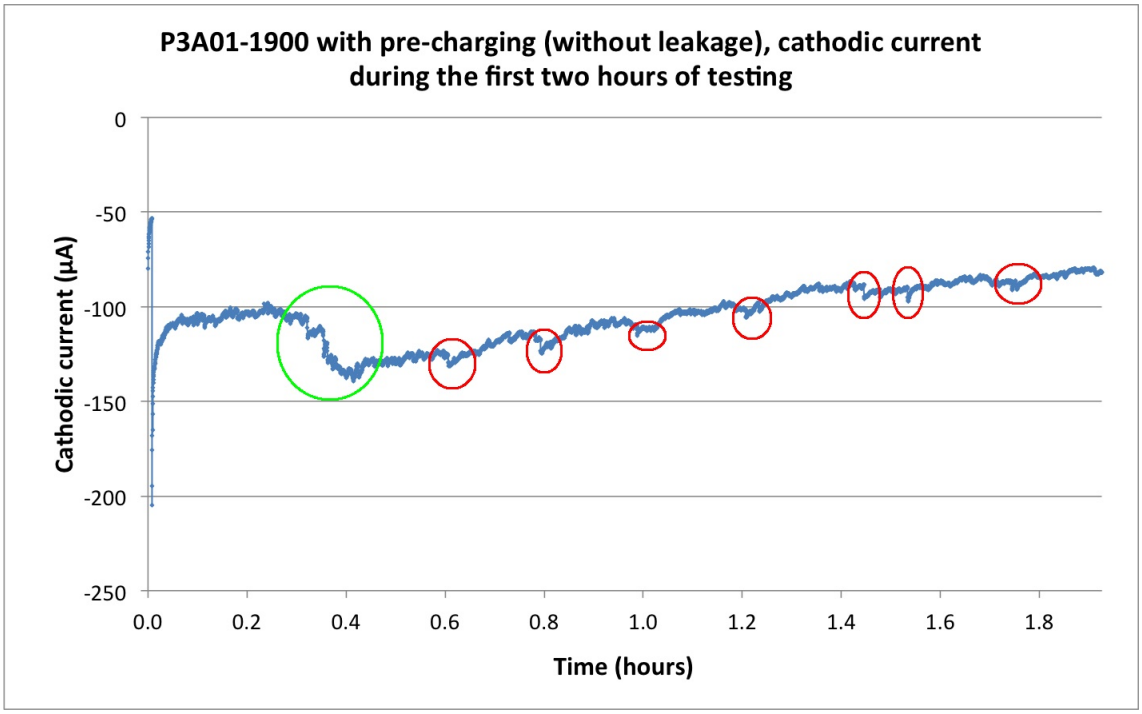

Figure 42: A plot showing the cathodic current recorded during the two initial hours of tensile testing of P3A01-1900 with pre-charging (Sample-1). No leakage occurred. Large bubble releases are marked with red.

6.10 In situ optical microscope images obtained during tensile testing

The microstructure in the samples were photographed in-situ using an optical microscope (OM). These images are aimed at showing the cracking behaviour and hydrogen evolution taking place at each stress level. Images were taken both from the pre-charged samples tested in seawater with CP, and from the reference samples tested in air. Some videos were also taken during the tensile tests. These are included in the electronic attachment submitted together with this master thesis. The pictures taken from the pre-charged samples were taken through the transparent PC chamber wall and the saltwater electrolyte. The brightness in some of these pictures is therefore somewhat dark. The pictures taken from the reference samples in air will therefore seem a little brighter in comparison. It should be noted that the extra light reflection and glare seen in the reference samples are the result of the medium which the sample surfaces were photographed through and not the amount of deformation on the sample.

6.10.1 56LH-1-OP

The images obtained from the pre-charged and hydrogen free samples from alloy 56LH-1-OP are shown in figure 43a - 43f and 44a - 44a respectively. Figure 43e shows a newly initiated crack at 124% of YS. After initiation, hydrogen evolution was observed to evolve from the crack. Figure 43f shows the same crack when the stress level has been increased to 132% of YS. It can be seen that the crack has grown into a much larger secondary crack. Cracks of visible size like the one shown in figure 43e, often initiated at the stress levels around 120% and 124% of YS. Hydrogen bubbles evolving were always observed from freshly initiated cracks.

The images in figure 44a - 44f show the images obtained from the reference samples tested in air. The reference samples from the 56LH-1-OP alloy fractured at 136% of YS, roughly 5% higher than the average fracture stress in the pre-charged samples. The interesting thing to note from figure 44a - 44f is that the initiation of cracks first started at 132% - 136% of YS. This is close to the fracture stress and indicates that only a very limited amount of secondary cracking occurs prior no fracture when hydrogen is absent.

The presence of hydrogen is therefore seen to result in the initiation of multiple secondary cracks at a stress level well below fracture stress. The cracks initiated in the pre-charged samples were for the most part IG cracks. In all the cracks initiated in saltwater with CP, hydrogen bubbles were seen evolving from the crack opening.

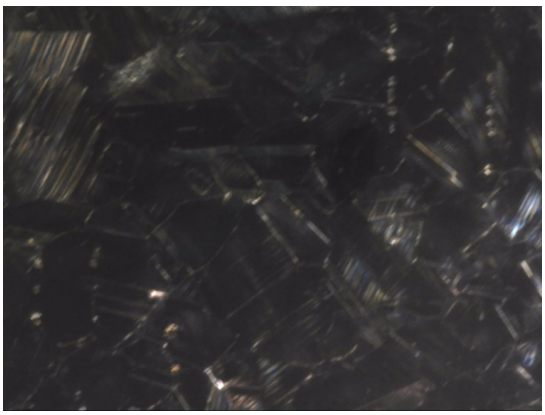

(a) 56LH-1-OP: Pre-charged sample at -1050 mV Ag/AgCl in saltwater at 116% of YS

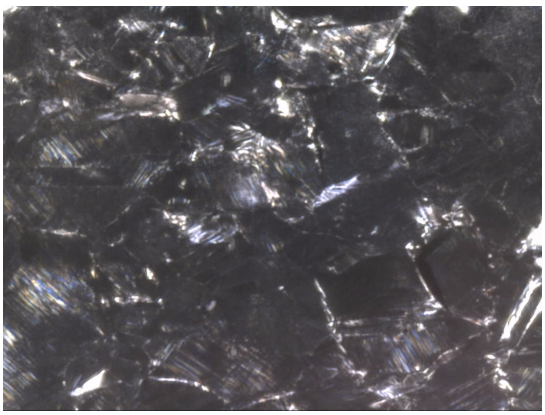

(b) 56LH-1-OP: Pre-charged sample at -1050 mV Ag/AgCl in saltwater at 128% of YS

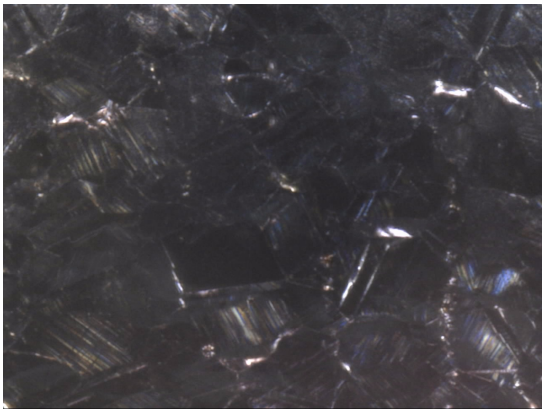

(c) 56LH-1-OP: Pre-charged sample at -1050 mV Ag/AgCl in saltwater at 120% of YS

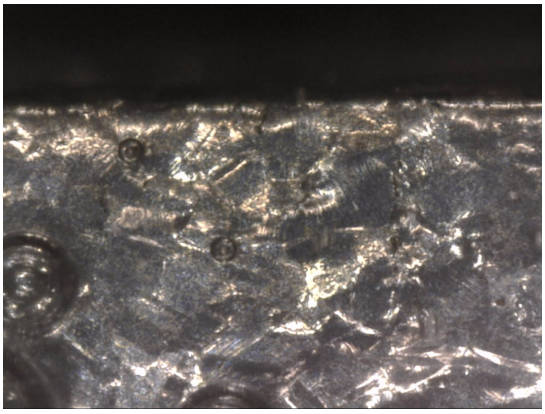

(d) 56LH-1-OP: Pre-charged sample at -1050 mV Ag/AgCl in saltwater at 132% of YS

(e) 56LH-1-OP: Pre-charged sample at -1050 mV Ag/AgCl in saltwater at 124% of YS

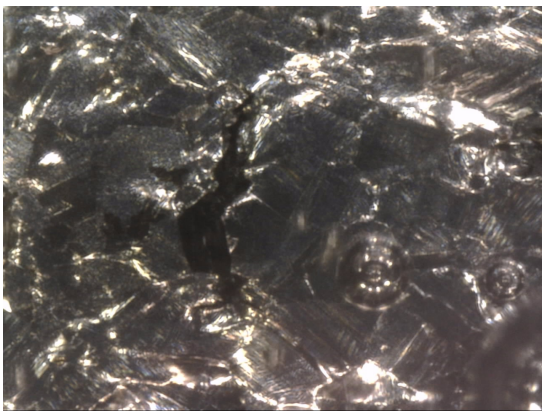

(f) 56LH-1-OP: Pre-charged sample at -1050 mV Ag/AgCl in saltwater at 132% of YS

Figure 43: Pictures taken from the 56LH-1-OP samples pre-charged with hydrogen.

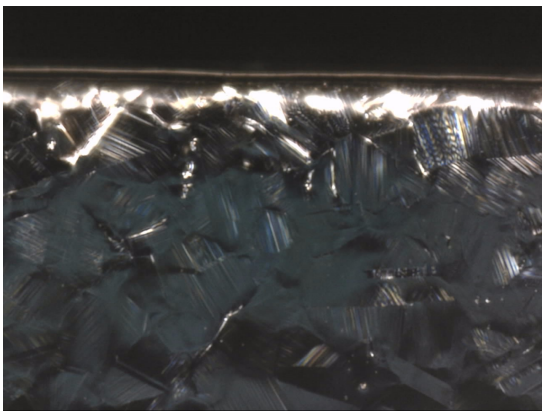

(a) 56LH-1-OP: Hydrogen free sample in air at 116% of YS

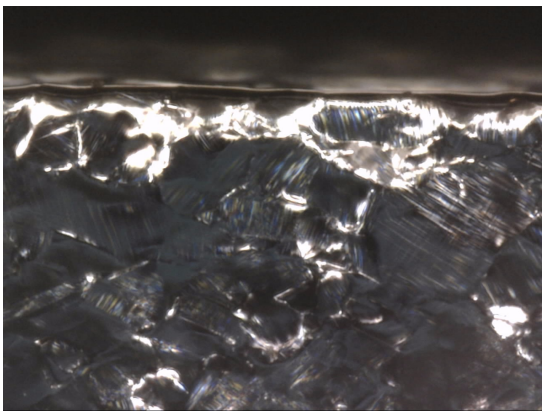

(b) 56LH-1-OP: Hydrogen free sample in air at 128% of YS

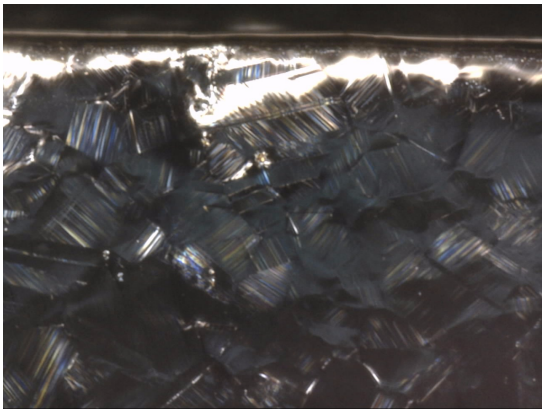

(c) 56LH-1-OP: Hydrogen free sample in air at 120% of YS

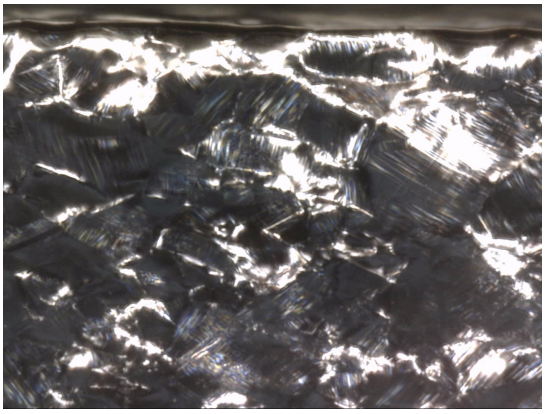

(d) 56LH-1-OP: Hydrogen free sample in air at 132% of YS

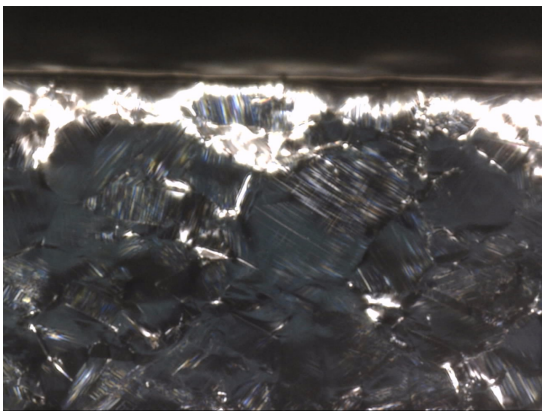

(e) 56LH-1-OP: Hydrogen free sample in air at 124% of YS

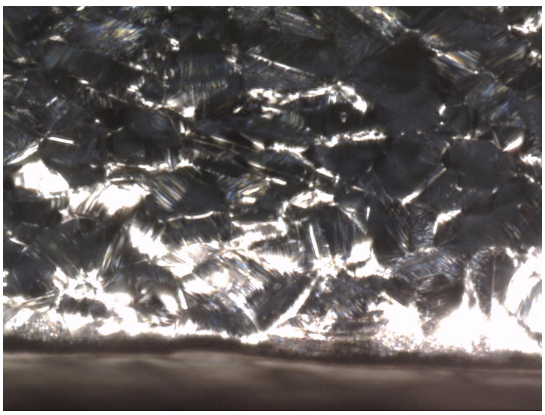

(f) 56LH-1-OP: Hydrogen free sample in air at 132% of YS

Figure 44: Pictures taken from the 56LH-1-OP reference samples.

6.10.2 56LH-1-Piece-1

The images obtained from the pre-charged and hydrogen free samples from alloy 56LH-1-Piece-1 are shown in figure 45a - 45f and 46a - 46f respectively. This alloy has a much more ductile behavior than the 56LH-1-OP and a larger YS - UTS stress interval measured by % YS. The pre-charged samples fractured at 140 - 150% of YS, whereas the hydrogen free reference samples reached the maximum load cell elongation (ϵ_{max}) at 152% without fracturing. Crack initiation in the pre-charged samples started at 136% - 140% of YS, which is fairly close to the average fracture strength of the pre-charged samples. Figure 45f shows a small crack initiated at 140% of YS. It should be noted that the crack-like features seen in figure 45b and 45d are twins, not actual cracks.

Figure 46a - 46f show the microstructure observed in the hydrogen free reference samples. The reference samples showed no sign of crack initiations and reached ϵ_{max} without fracturing.

Alloy 56LH-1-Piece-1 is the most ductile of the Inconel-718 variants tested in this master. Furthermore, secondary cracks are only observed close to fracture stress of the pre-charged samples. Hydrogen bubble were also seen evolving from these crack openings. Since the secondary cracks first started to initiate close to the fracture strength of the pre-charged samples, the resistance to secondary cracking in this alloy appears to be better than that of 56LH-1-OP.

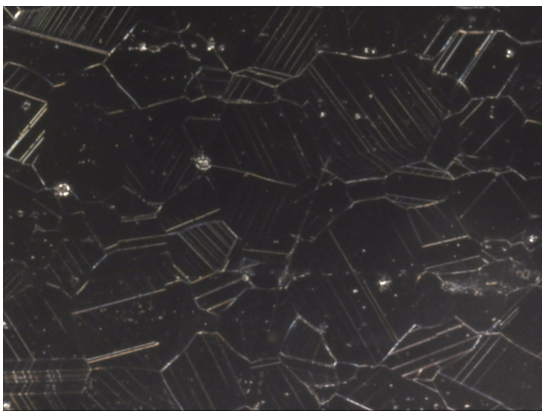

(a) 56LH-1-Piece-1: Pre-charged sample at -1050 mV Ag/AgCl in saltwater at 116% of YS

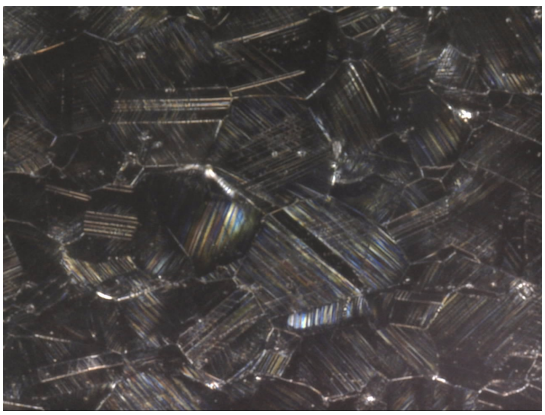

(b) 56LH-1-Piece-1: Pre-charged sample at -1050 mV Ag/AgCl in saltwater at 128 of YS

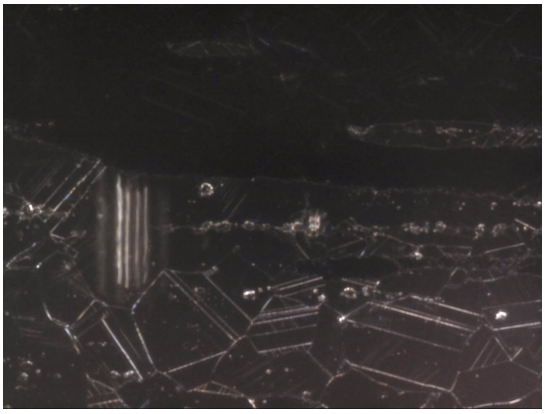

(c) 56LH-1-Piece-1: Pre-charged sample at -1050 mV Ag/AgCl in saltwater at 120% of YS

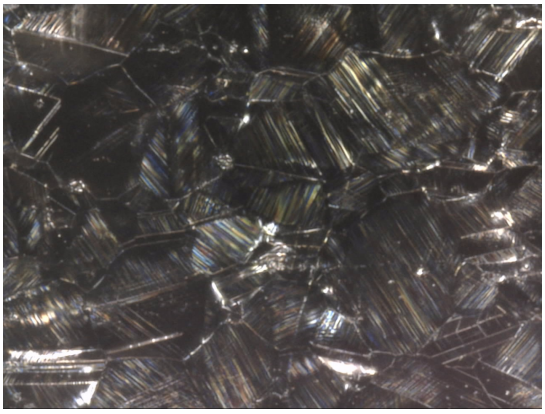

(d) 56LH-1-Piece-1: Pre-charged sample at -1050 mV Ag/AgCl in saltwater at 132% of YS

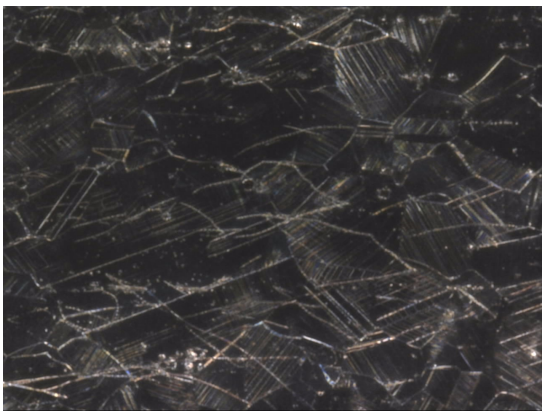

(e) 56LH-1-Piece-1: Pre-charged sample at -1050 mV Ag/AgCl in saltwater at 124% of YS

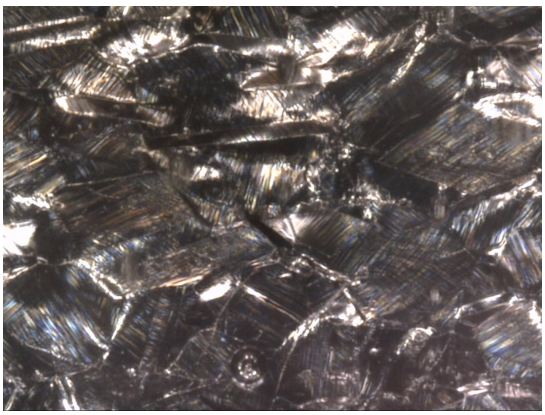

(f) 56LH-1-Piece-1: Pre-charged sample at -1050 mV Ag/AgCl in saltwater at 140% of YS

Figure 45: Pictures taken from the 56LH-1-Piece-1 samples pre-charged with hydrogen.

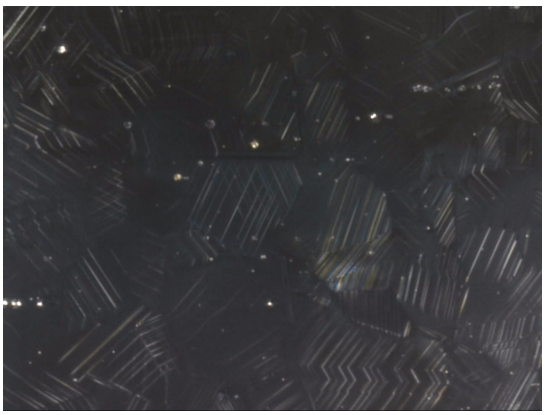

(a) 56LH-1-Piece-1: Hydrogen free sample in air at 120% of YS

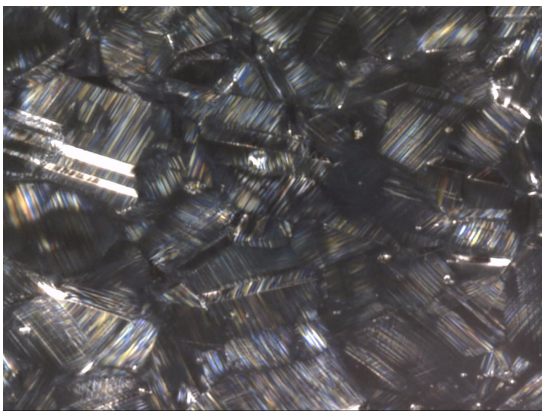

(b) 56LH-1-Piece-1: Hydrogen free sample in air at 136% of YS

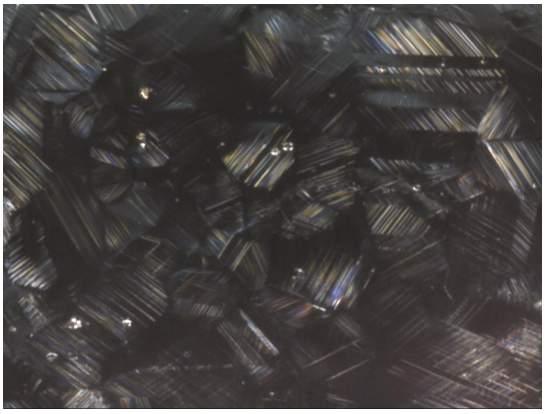

(c) 56LH-1-Piece-1: Hydrogen free sample in air at 128% of YS

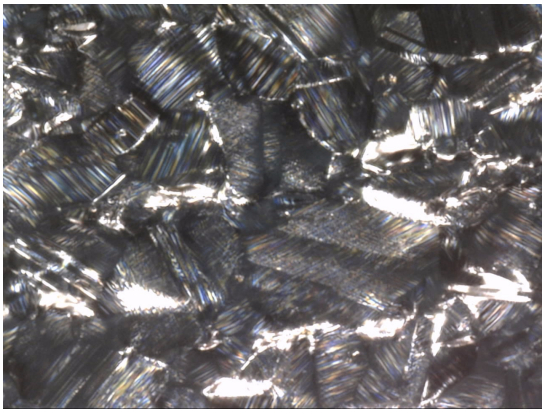

(d) 56LH-1-Piece-1: Hydrogen free sample in air at 144% of YS

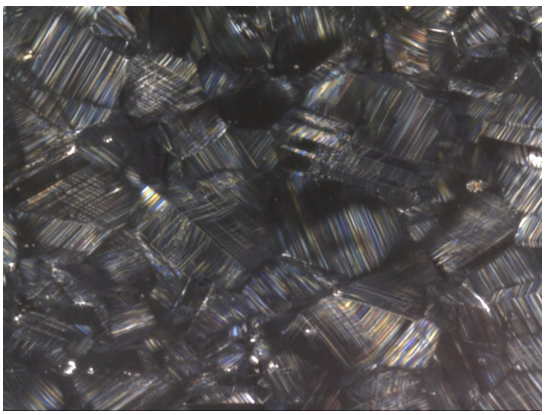

(e) 56LH-1-Piece-1: Hydrogen free sample in air at 132% of YS

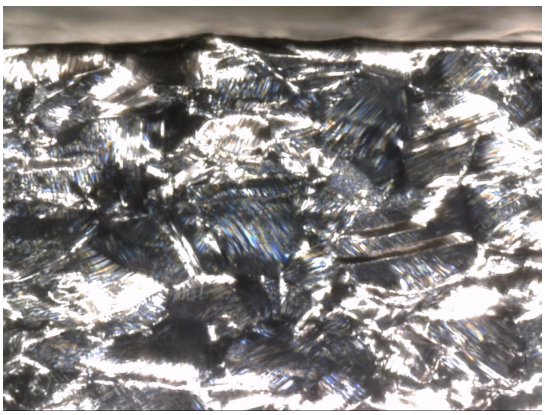

(f) 56LH-1-Piece-1: Hydrogen free sample in air at 148% of YS

Figure 46: Pictures taken from the 56LH-1-OP reference samples.

6.10.3 56LH-1-Piece-2

The images obtained from the pre-charged samples from alloy 56LH-1-Piece-2 are shown to the left in figure 47a, c and e while the hydrogen free reference samples are shown on the right in figure 47b, d and f. Both the pre-charged and the hydrogen free samples from this alloy exhibited very limited amount of secondary cracking, even when the stress was close to fracture. One occasional small secondary crack was observed and filmed. This video clip is included in the electronic attachment. No secondary cracks were observed in the reference samples.

Very little secondary cracking was observed in the pre-charged samples from this alloy. This does not mean that the alloy is more resistant to hydrogen embrittlement though, as obvious from the RA and ϵ losses presented earlier.

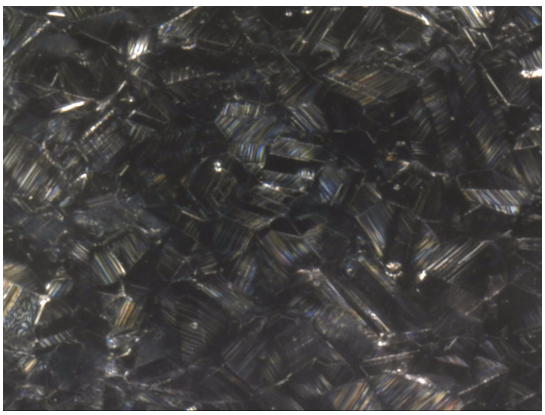

(a) 56LH-1-Piece-2: Pre-charged sample at -1050 mV Ag/AgCl in saltwater at 108% of YS

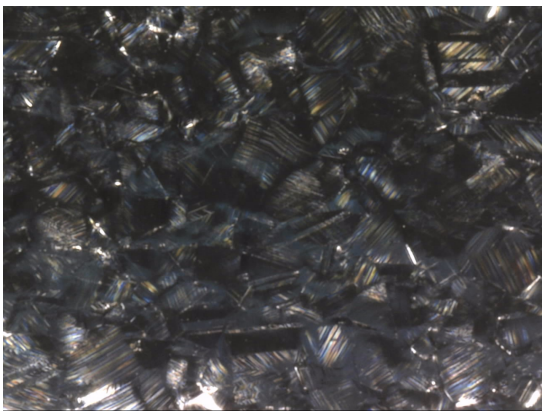

(b) 56LH-1-Piece-2: Hydrogen free sample in air at 108% of YS

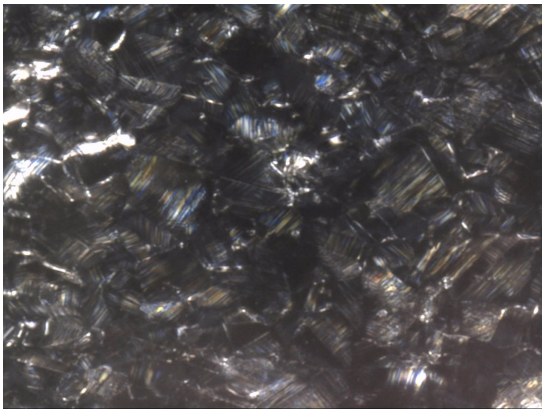

(c) 56LH-1-Piece-2: Pre-charged sample at -1050 mV Ag/AgCl in saltwater at 112% of YS

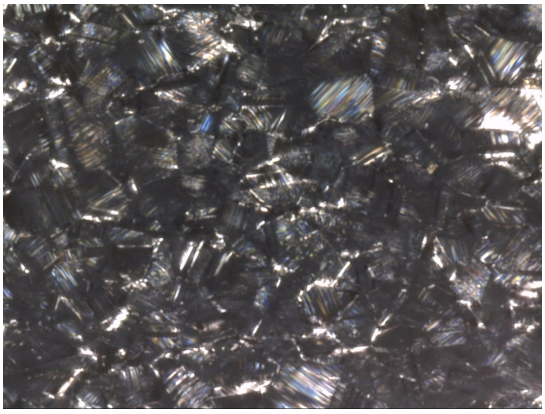

(d) 56LH-1-Piece-2: Hydrogen free sample in air at 112% of YS

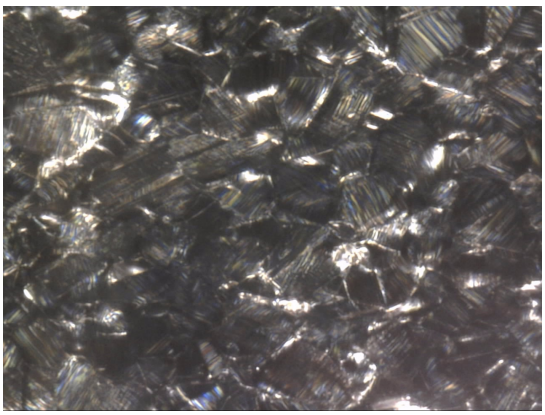

(e) 56LH-1-Piece-2: Pre-charged sample at -1050 mV Ag/AgCl in saltwater at 116% of YS

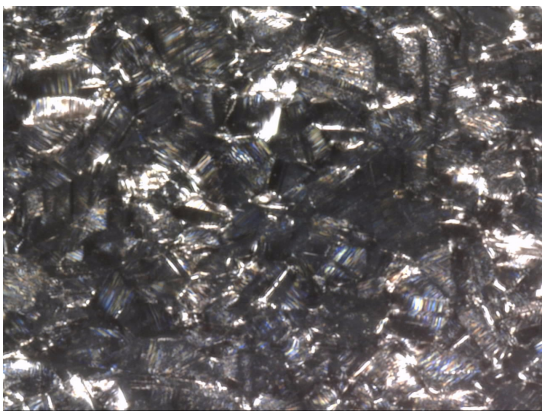

(f) 56LH-1-Piece-2: Hydrogen free sample in air at 116% of YS

Figure 47: Pictures taken from the 56LH-1-Piece-2 pre-charged samples (on the left) and reference samples (on the right)

6.10.4 P3A01-1900

The images obtained from the pre-charged and hydrogen free samples from alloy P3A01-1900 are shown in figure 48a - 48f and 49a - 49f respectively. Figure 48c shows a bubble of hydrogen evolving from the sample surface, possibly at a particle or some local roughness. This picture was taken at 112% of YS. Figure 48e show the same area at 116% of YS, where a large crack have initiated. Hydrogen is still evolving from the interior of the crack (not shown in the picture). Figure 48b shows a surface crack formed at the edge at 116% of YS. Nearby secondary cracks have formed around this crack as well. This large crack turned out to be the critical crack resulting in failure. Figure 48d and 48f show the crack at 116% of YS after 15 and 30 minutes respectively.

The hydrogen free reference sample displayed in figure 49a - 49f showed no cracks, even at 120% of YS. The sample fractured at 124% of YS, and even then, no secondary cracks were observed in the SEM ("Secondary cracks observed in SEM" subsection).

This alloy is by far the alloy variant which showed largest amount of secondary cracking as a resulting of hydrogen pre-charging. This is interesting as the alloy showed the same ductility loss as 56LH-1-OP which have the same microstructure. The large degree of hydrogen effected secondary cracking may be a result of the low C/N content: C and N normally segregate at the GB. When these species are as good as absent, there my be more sites for hydrogen atoms to occupy at the GB, leading to increased hydrogen assisted secondary cracking at the GB's.

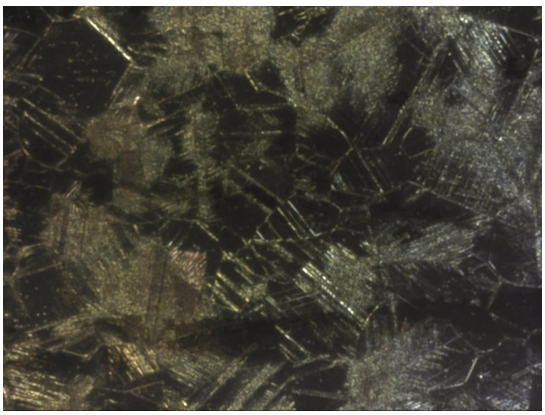

(a) P3A01-1900: Pre-charged sample at -1050 mV Ag/AgCl in saltwater at 108% of YS

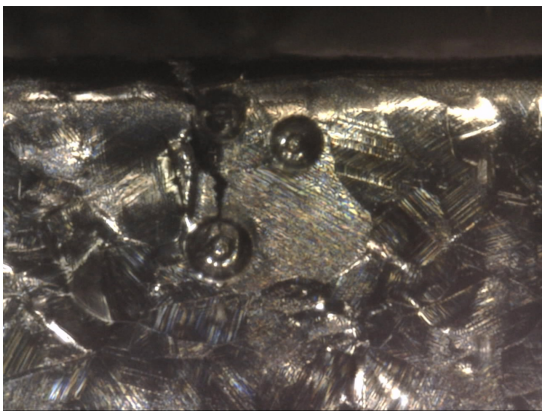

(b) P3A01-1900: Pre-charged sample at -1050 mV Ag/AgCl in saltwater at 116% of YS

(c) P3A01-1900: Pre-charged sample at -1050 mV Ag/AgCl in saltwater at 112% of YS

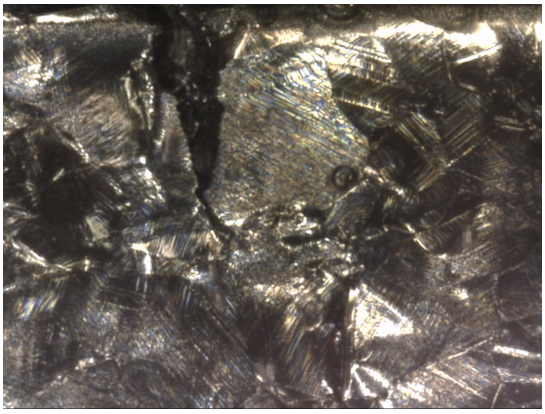

(d) P3A01-1900: Pre-charged sample at -1050 mV Ag/AgCl in saltwater at 116% of YS

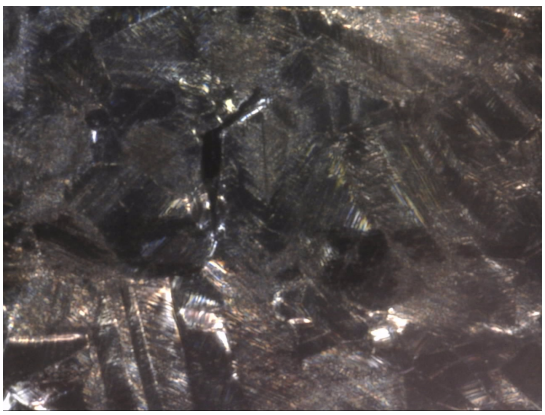

(e) P3A01-1900: Pre-charged sample at -1050 mV Ag/AgCl in saltwater at 116% of YS

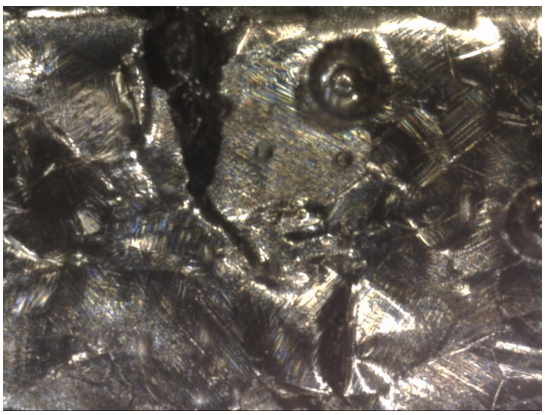

(f) P3A01-1900: Pre-charged sample at -1050 mV Ag/AgCl in saltwater at 116% of YS

Figure 48: Pictures taken from the P3A01-1900 samples pre-charged with hydrogen.

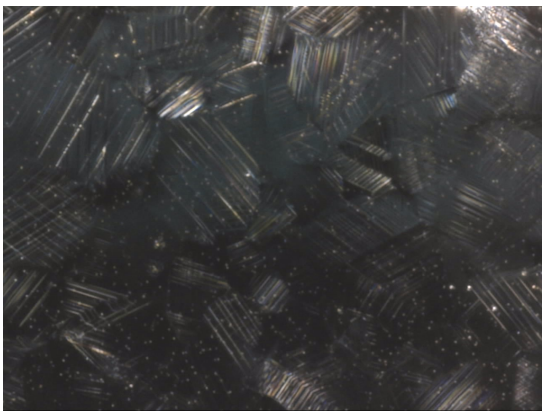

(a) P3A01-1900: Hydrogen free sample in air at 108% of YS

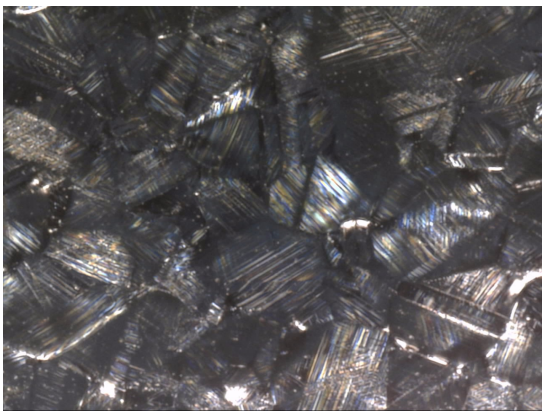

(b) P3A01-1900: Hydrogen free sample in air at 116% of YS

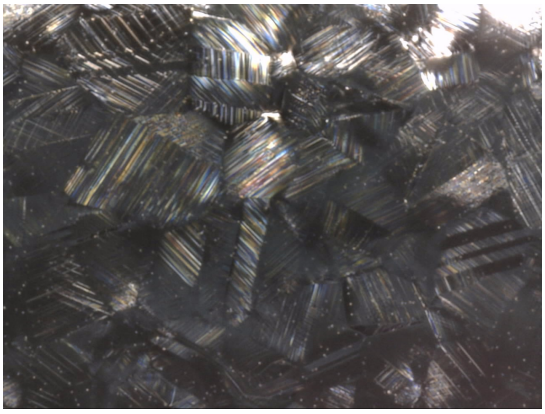

(c) P3A01-1900: Hydrogen free sample in air at 112% of YS

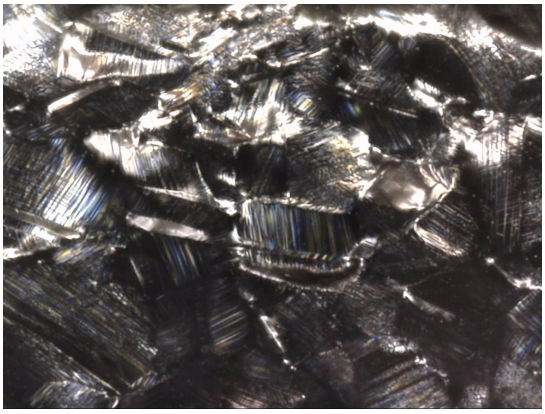

(d) P3A01-1900: Hydrogen free sample in air at 120% of YS

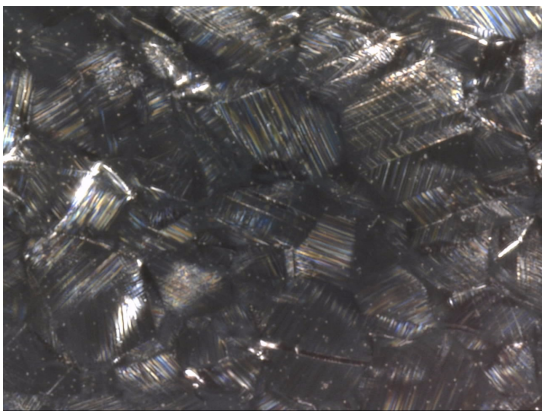

(e) P3A01-1900: Hydrogen free sample in air at 116% of YS

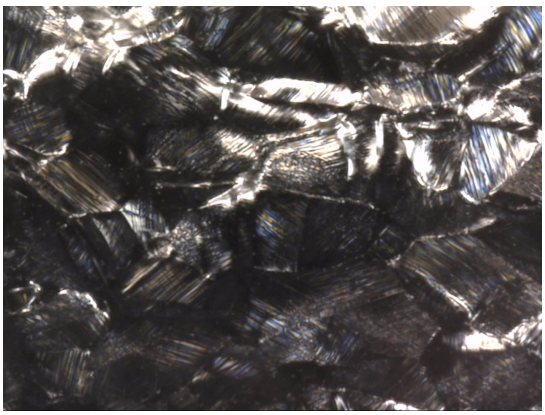

(f) P3A01-1900: Hydrogen free sample in air at 120% of YS

Figure 49: Pictures taken from the P3A01-1900 reference samples.

6.10.5 P3A01-1850A

The images obtained from the pre-charged and hydrogen free samples from alloy P3A01-1850A alloy are shown in figure 50a - 50f and 51a - 51f respectively. Because of the ultra fine grain size in this alloy, cracks were not possible to observe. It is therefore uncertain how the hydrogen free and pre-charged samples compare. The visible hydrogen evolution at various sites nevertheless increased at the highest stress levels, which may indicate that small cracks have been initiated. An example of this is shown in figure 50b where a large hydrogen bubble is forming on some sort of crack, particle or irregularity.

6.10.6 P3A01-1800

The same results was found for the P3A01-1800 alloy, which has an almost identical microstructure as P3A01-1850A. The images obtained from the pre-charged and hydrogen free samples from alloy P3A01-1850A alloy are shown in figure 52a - 52d and 53a - 53b respectively. Not much can be seen from the pictures, due to the fine grain size.

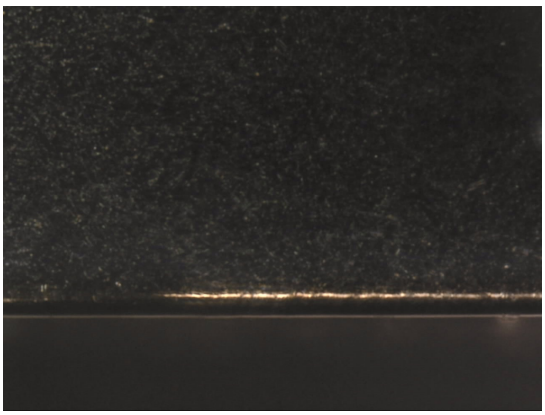

(a) P3A01-1850A: Pre-charged sample at -1050 mV Ag/AgCl in saltwater at 104% of YS

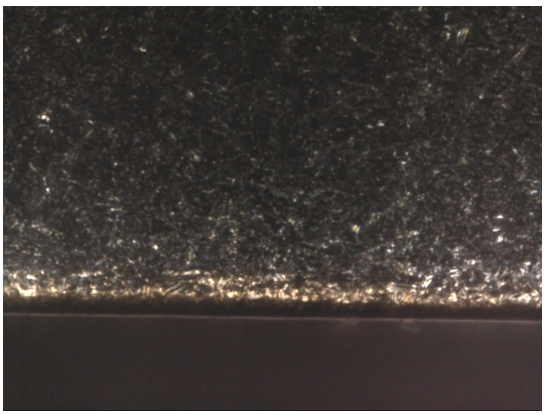

(b) P3A01-1850A: Pre-charged sample at -1050 mV Ag/AgCl in saltwater at 112 of YS

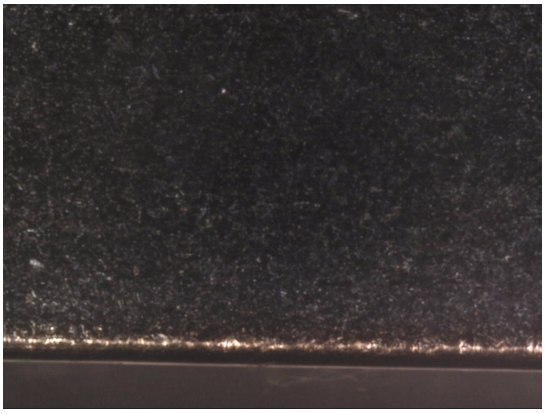

(c) P3A01-1850A: Pre-charged sample at -1050 mV Ag/AgCl in saltwater at 108% of YS

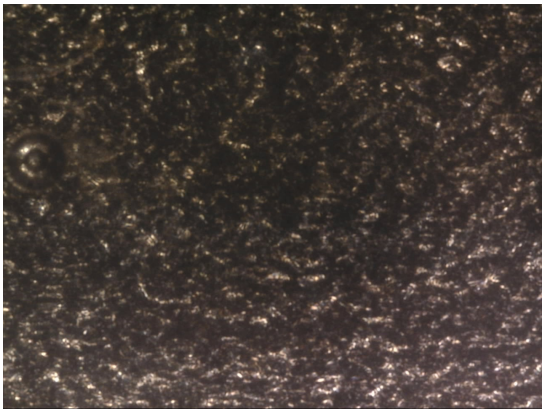

(d) P3A01-1850A: Pre-charged sample at -1050 mV Ag/AgCl in saltwater at 116% of YS

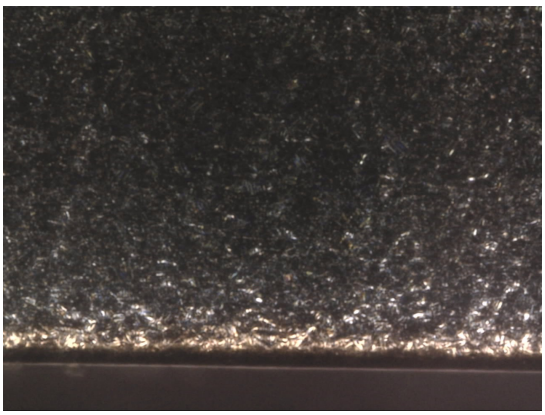

(e) P3A01-1850A: Pre-charged sample at -1050 mV Ag/AgCl in saltwater at 116% of YS

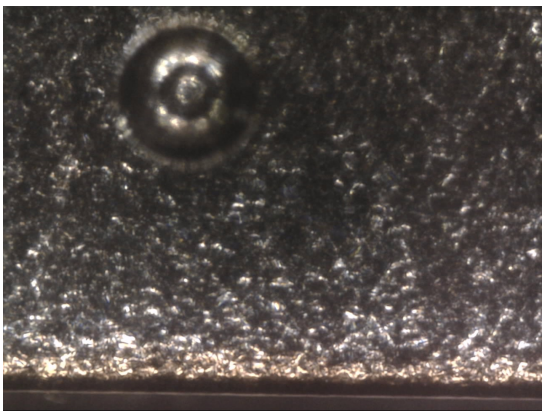

(f) P3A01-1850A: Pre-charged sample at -1050 mV Ag/AgCl in saltwater at 116% of YS

Figure 50: Pictures taken from the P3A01-1850A samples pre-charged with hydrogen.

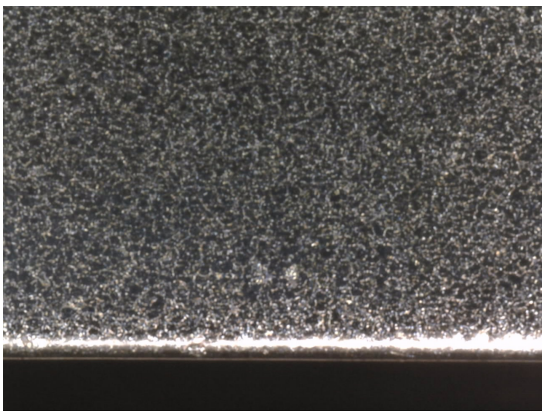

(a) P3A01-1850A: Hydrogen free sample in air at 108% of YS

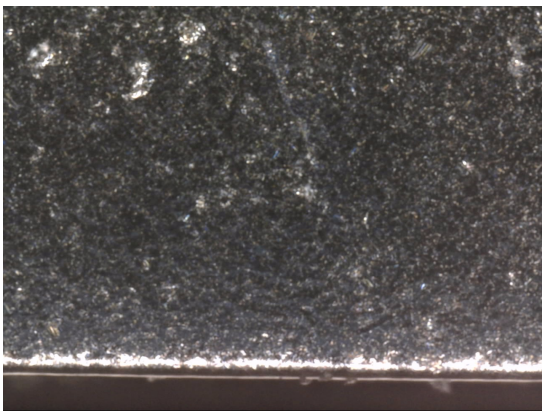

(b) P3A01-1850A: Hydrogen free sample in air at 116% of YS

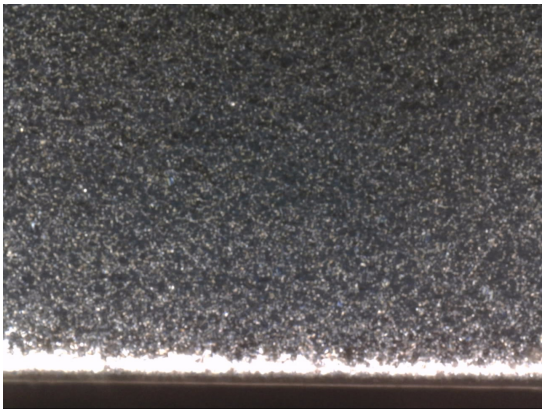

(c) P3A01-1850A: Hydrogen free sample in air at 112% of YS

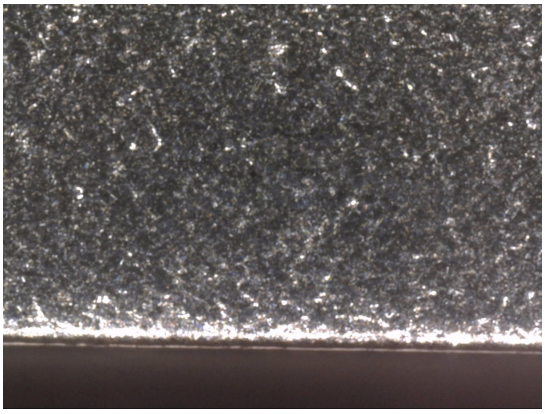

(d) P3A01-1850A: Hydrogen free sample in air at 120% of YS

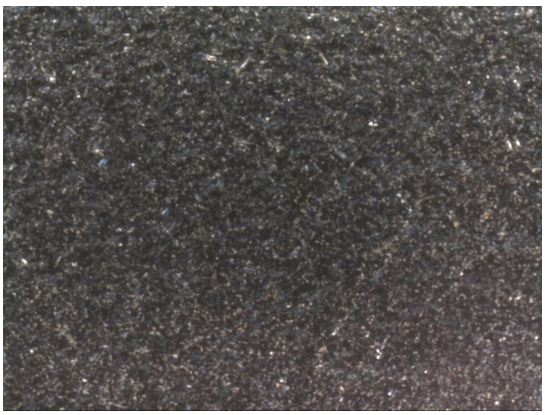

(e) P3A01-1850A: Hydrogen free sample in air at 116% of YS

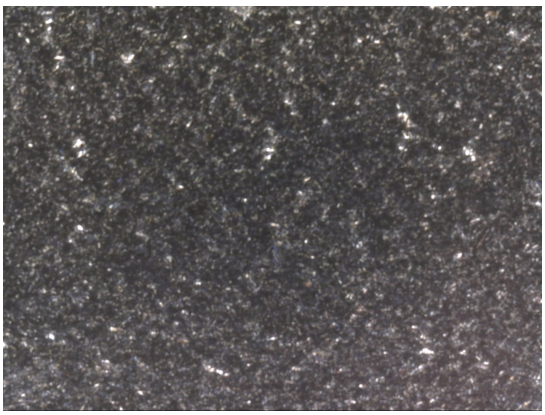

(f) P3A01-1850A: Hydrogen free sample in air at 120% of YS

Figure 51: Pictures taken from the P3A01-1850A reference samples.

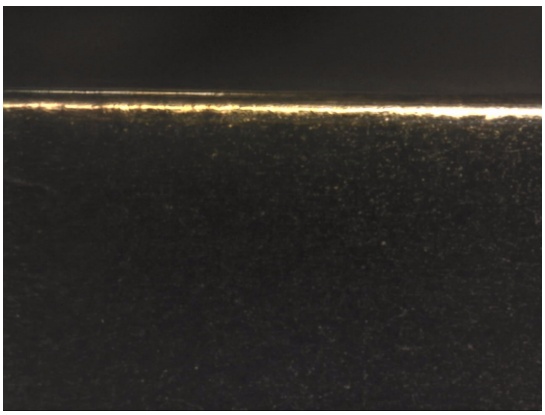

(a) P3A01-1800: Pre-charged sample at -1050 mV Ag/AgCl in saltwater at 104% of YS

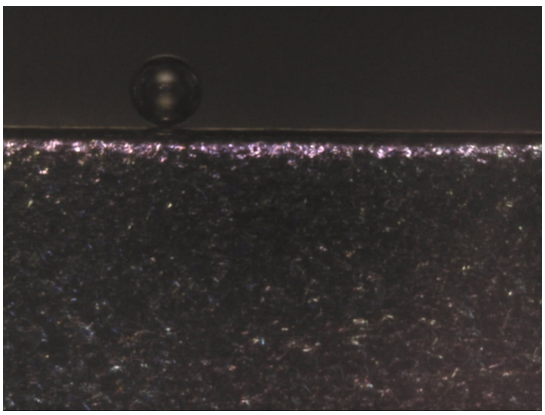

(b) P3A01-1800: Pre-charged sample at -1050 mV Ag/AgCl in saltwater at 112 of YS

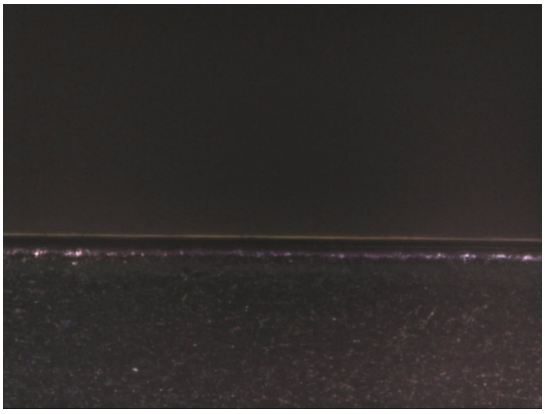

(c) P3A01-1800: Pre-charged sample at -1050 mV Ag/AgCl in saltwater at 108% of YS

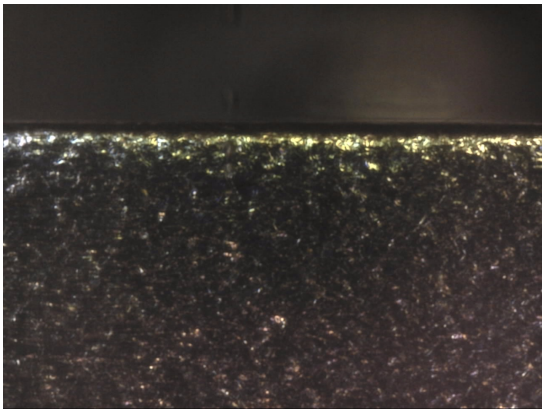

(d) P3A01-1800: Pre-charged sample at -1050 mV Ag/AgCl in saltwater at 116% of YS

Figure 52: Pictures taken from the P3A01-1800 samples pre-charged with hydrogen.

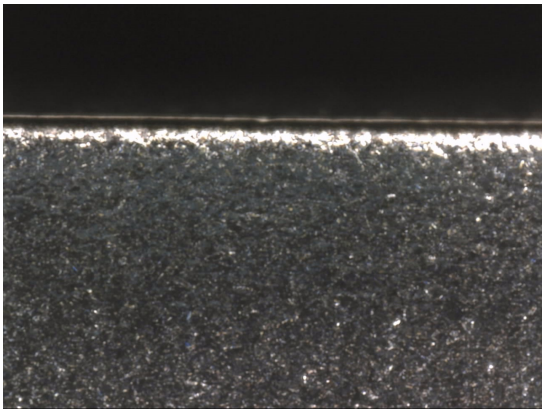

(a) P3A01-1800: Hydrogen free sample in air at 116% of YS

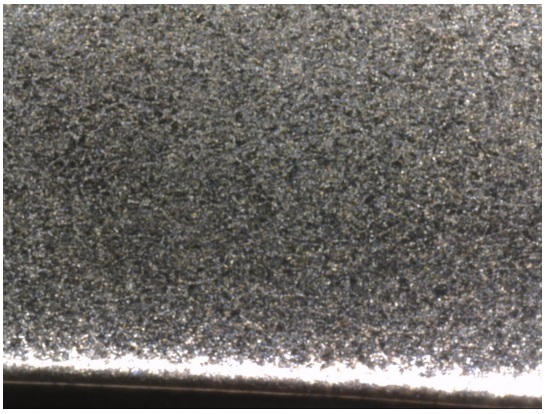

(b) P3A01-1800: Hydrogen free sample in air at 116% of YS

Figure 53: Pictures taken from the P3A01-1800 reference samples.

6.11 Fracture surfaces imaged in SEM

6.11.1 56LH-1-OP

Figure 54 shows an image of the fracture surface resulting from a pre-charged sample from 56LH-1-OP. The central areas of the fracture surface are dominated by ductile fractures. The ductile fracture is evident from the dimpled surface with occasional broken particles, which indicates fracture from MVC. The upper and lower right areas in the picture show some brittle features, with both IG and ductile fractures. Figure 55 shows a higher magnification image of this IG fracture area. The IG fractures mode close to the surface can be seen clearly here, as the "rocky" texture is a typical indicator of IG fractures. This texture occurs when the fracture propagates along the GBs, leaving entire grain facets exposed on the fracture surface.

Moving further away from the surface, the fracture mode shifts from completely IG over to a mixture of brittle and ductile features. Figure 56 shows an image taken from a fracture area consisting of both ductile and IG features. This fracture area is characterized by a mix of "rocky" and dimpled textures. The ductile fracture seen in the centre of all the 56LH-1-OP samples tested is displayed in figure 57. In this image the fracture area is scattered with small ripples and dimples, indicating plastic deformation prior to fracture. Some larger voids containing fractured particles are also observed. These features are strong evidence of ductile fracture occurring according to MVC.

In this mechanism micro voids initiates at the interface of hard secondary particles like MC-carbides or δ-particles during deformation. Fracture occurs when these micro voids start to grow and coalesce. The triaxial stress created between the voids pulls and elongates the matrix into the dimpled fracture surface seen. The ductile fracture displayed in figure 57 is characteristic of the ductile fracture observed in the centre of all the alloys examined in this study, both with and without hydrogen.

All the pre-charged 56LH-1-OP samples exhibited brittle IG fractures around the edge of the fracture surface, and ductile fracture in the central regions. This is to be expected as hydrogen is only able to diffuse a limited distance into the sample during pre-charging. The hydrogen free reference samples from 56LH-1-OP did not show any brittle features and all showed a completely ductile fracture surface scattered with dimples.

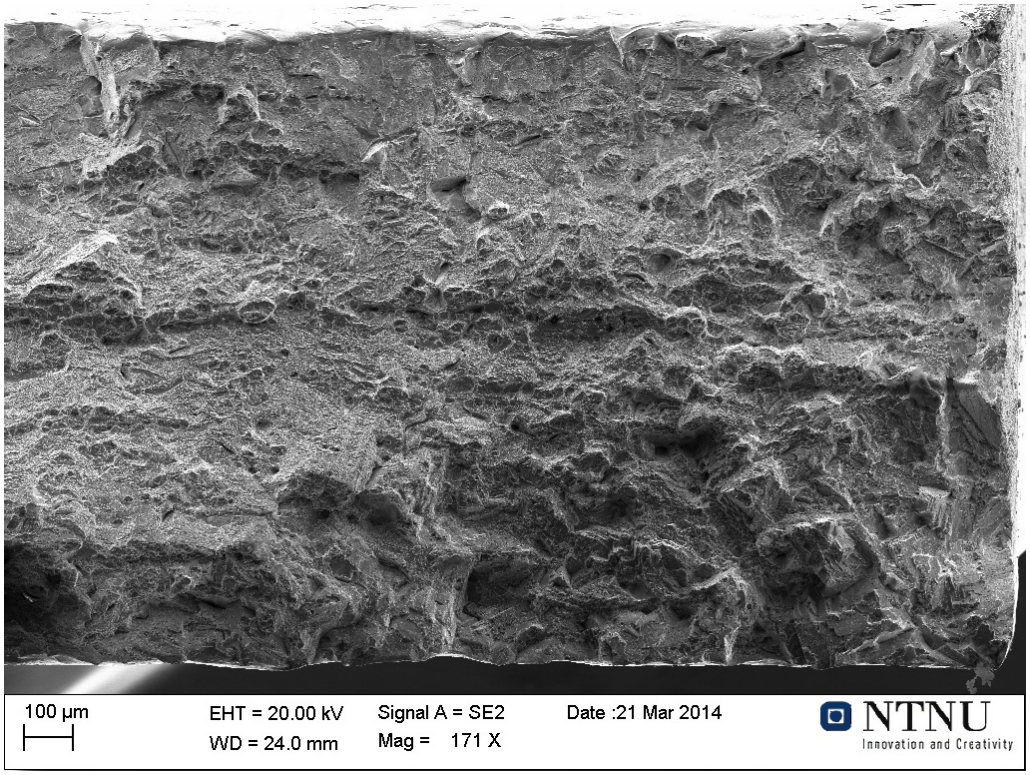

Figure 54: SEM image (171X) taken from 56LH-1-OP Sample-2 pre-charged with hydrogen. Ductile fracture is seen in the centre while the edge exhibits IG fracture.

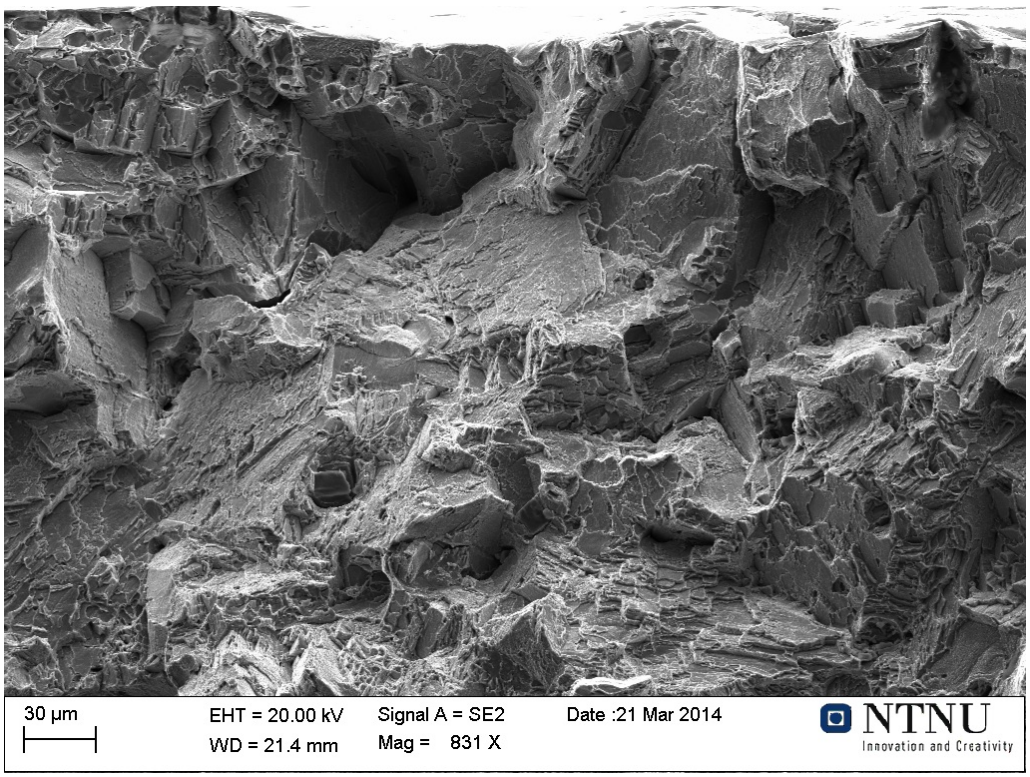

Figure 55: SEM image (831X) taken from 56LH-1-OP Sample-1 pre-charged with hydrogen. The IG fracture at the edge is seen clearly from the "rocky" features.

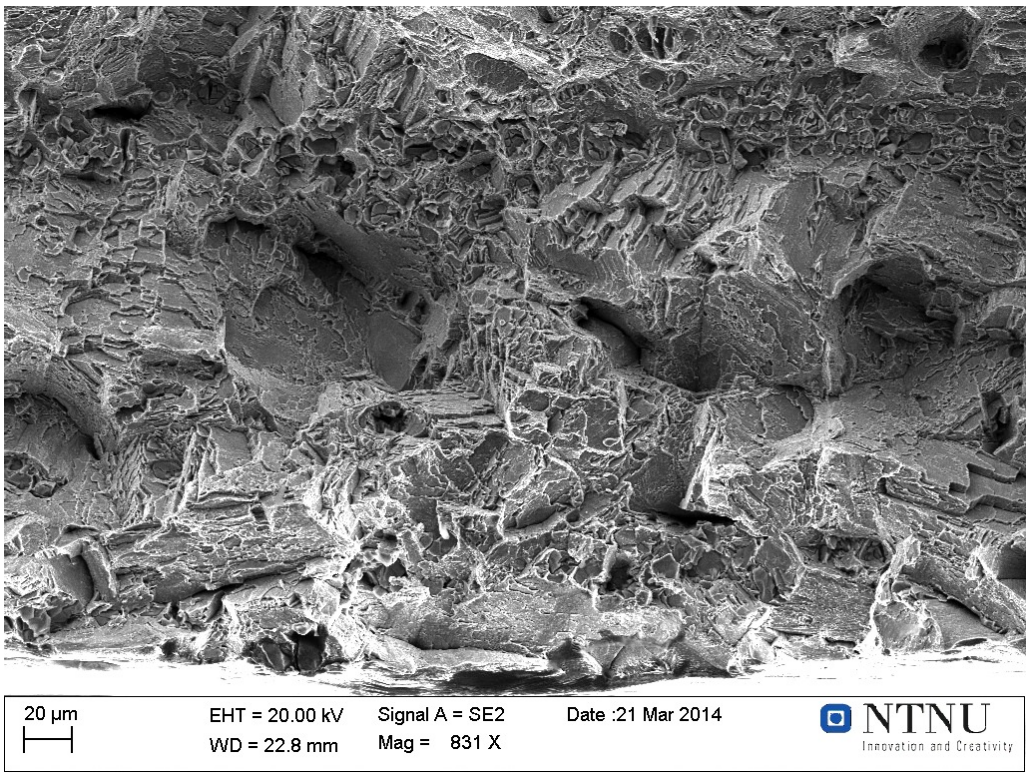

Figure 56: SEM image (831X) taken from 56LH-1-OP Sample-3 pre-charged with hydrogen. The image shows a mixture of IG and ductile features.

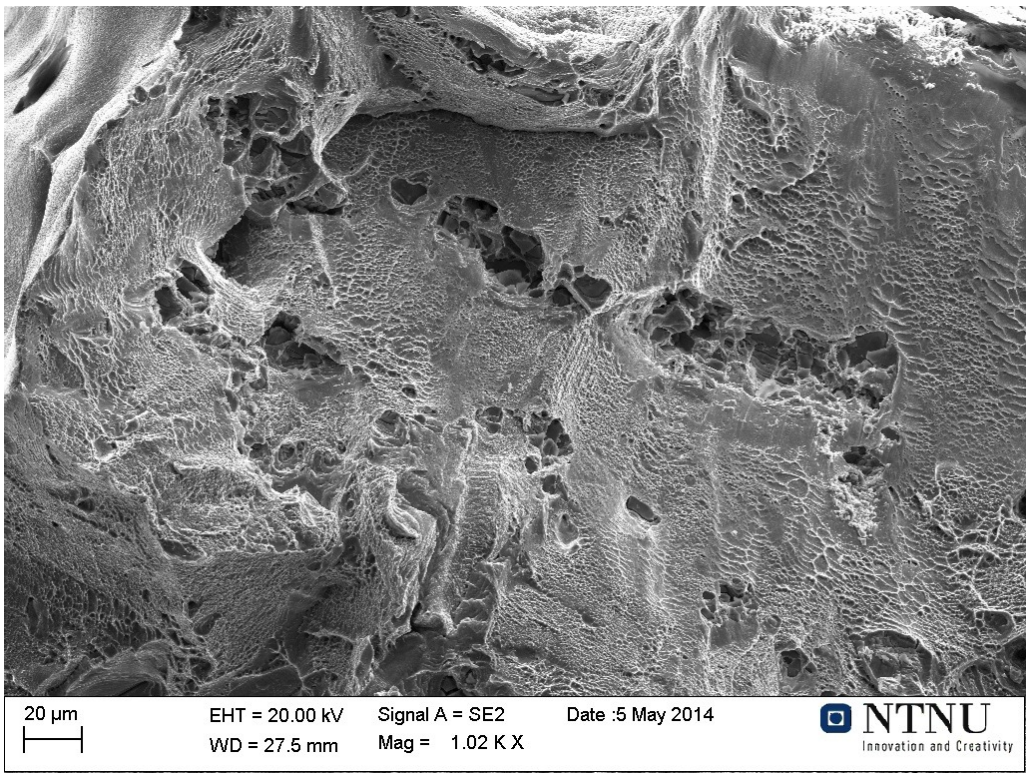

Figure 57: SEM image (1020X) taken from 56LH-1-OP Sample-4 pre-charged with hydrogen. The picture is taken from the centre of the sample. A dimpled fracture surface with occasional broken particles left in the larger micro voids.

6.11.2 56LH-1-Piece-1

The fracture resulting from one of the 56LH-1-Piece-1 samples pre-charged with hydrogen is shown in figure 58. The areas close to the edge seen in the top of the picture exhibit an IG fracture, characterized by its "rocky" texture. The central areas still exhibit a ductile fracture with dimples and micro voids, similar to the ductile fracture presented for 56LH-1-OP in figure 57. The brittle IG area is shown in figure 59. A large facet can be seen resulting from a large grain fracturing along its GB. The hydrogen free reference samples from this alloy exhibited a completely ductile fracture, similar to the fracture surface displayed in figure 57.

In summary, all the features describes from the SEM images taken from 56LH-1-OP can also be found in 56LH-1-Piece-1. This is not surprising as the the two alloys have similar composition and grain size. The 56LH-1-Piece-1 contains some δ-particles, but these are course, far apart and are not located along GBs. They are therefore not expected to a have a large effect on the hydrogen embrittlement.

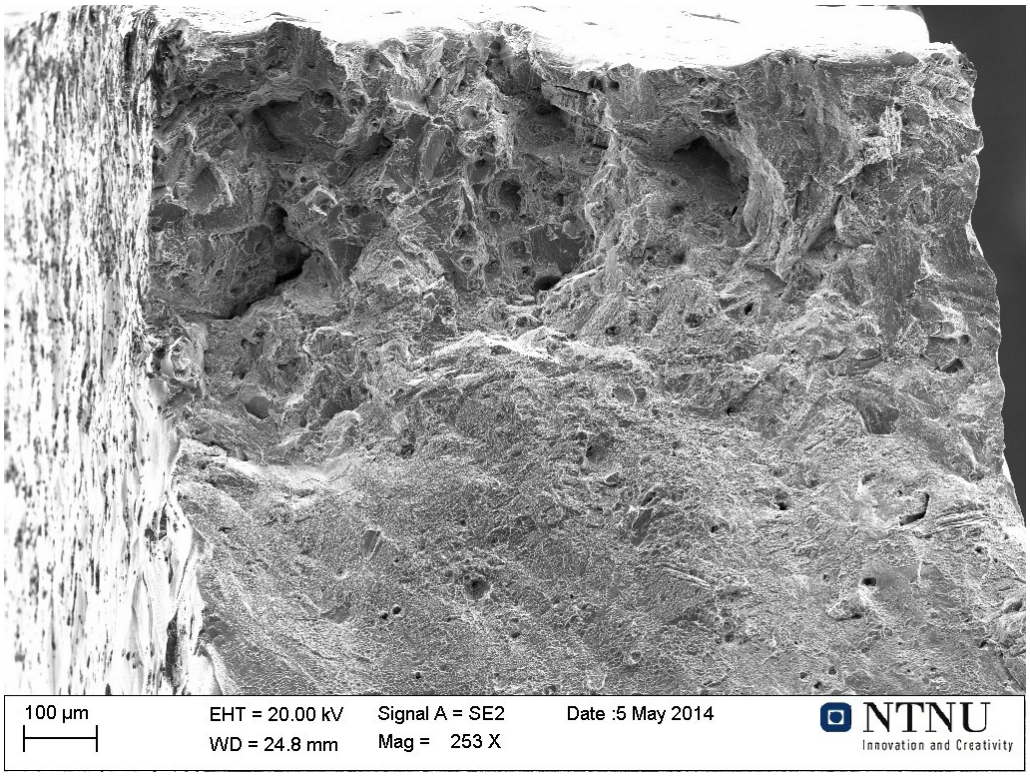

Figure 58: SEM image (253X) taken from 56LH-1-Piece-1 Sample-5 pre-charged with hydrogen. The central areas show ductile behavior, while mixed ductile and IG fractures can be seen close to the edges.

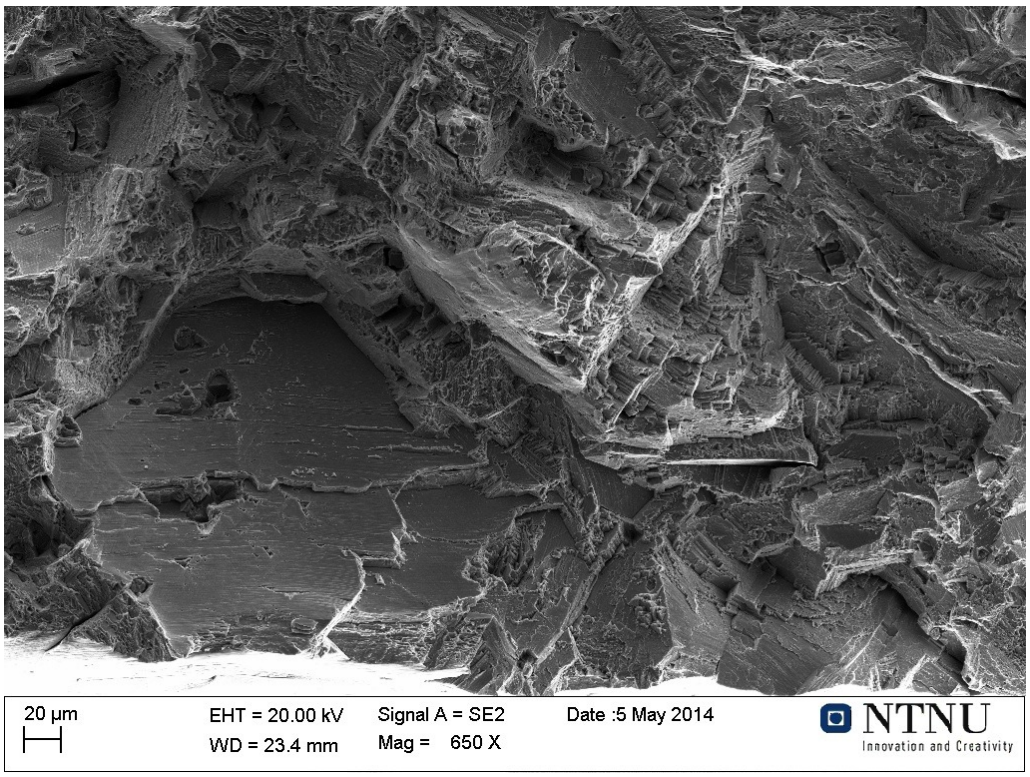

Figure 59: SEM image (650X) taken from 56LH-1-Piece-1 Sample-5 pre-charged with hydrogen. A completely IG fracture can be seen close to the edge, as a large grain has fractured along its grain boundary leaving the facet seen in the image

6.11.3 56LH-1-Piece-2

The fracture surface resulting from one of the pre-charged samples from 56LH-1-Piece-2 (Sample-1) is shown in figure 60. The left area close to the edge exhibits a completely IG fracture. The central area is dominated by ductile behavior, seen as dimpled textures from MVC. A higher magnification image is displayed in figure 61, showing the IG area identified. The facets and "rocky" textures indicate an IG fracture mode. The hydrogen free reference samples from alloy 56LH-1-Piece-2 showed a completely ductile fracture of the type presented previously in figure 57. The grain size in this alloy is slightly finer then the grain size in the two preceding alloys examined, but it contain a similar amount and distribution of δ-particles as the 56LH-1-Piece-1 alloy.

In summary, the embrittlement effect seen in 56LH-1-Piece-2 is similar to the embrittlement seen in ally 56LH-1-OP and 56LH-1-Piece-1. As the 56LH-1-Piece-2 only have a slightly finer grain size this is not surprising, since the microstructure and composition is otherwise the same.

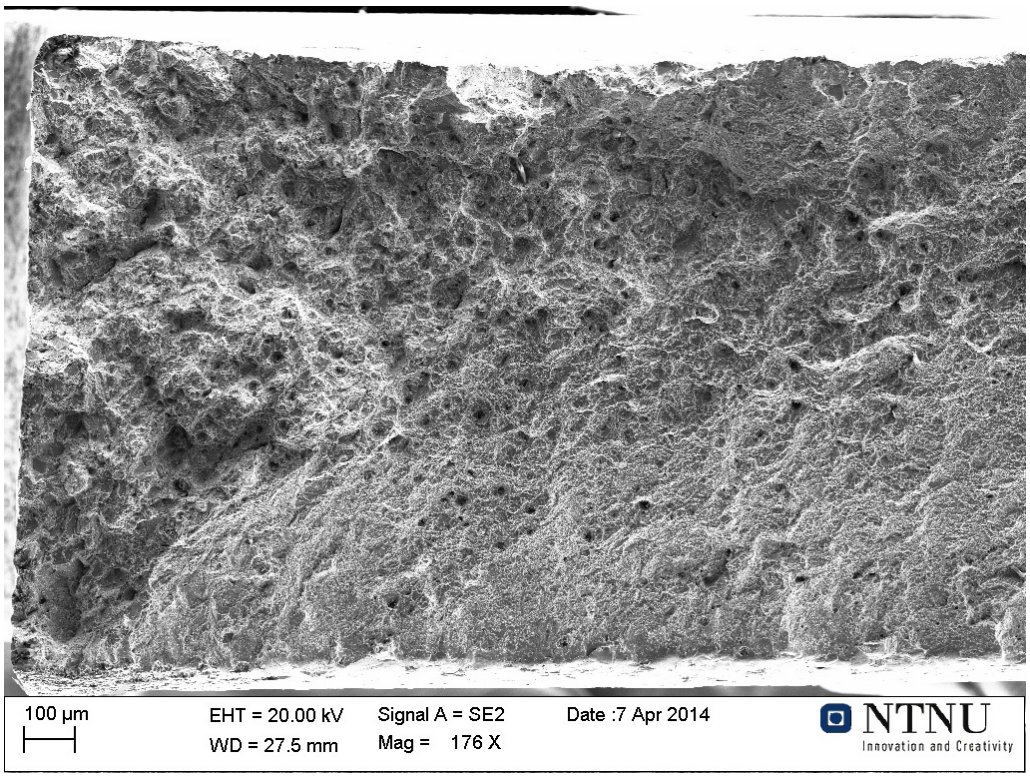

Figure 60: SEM image (176X) taken from 56LH-1-Piece-2 Sample-1 pre-charged with hydrogen. An IG fracture area can be seen to the left.

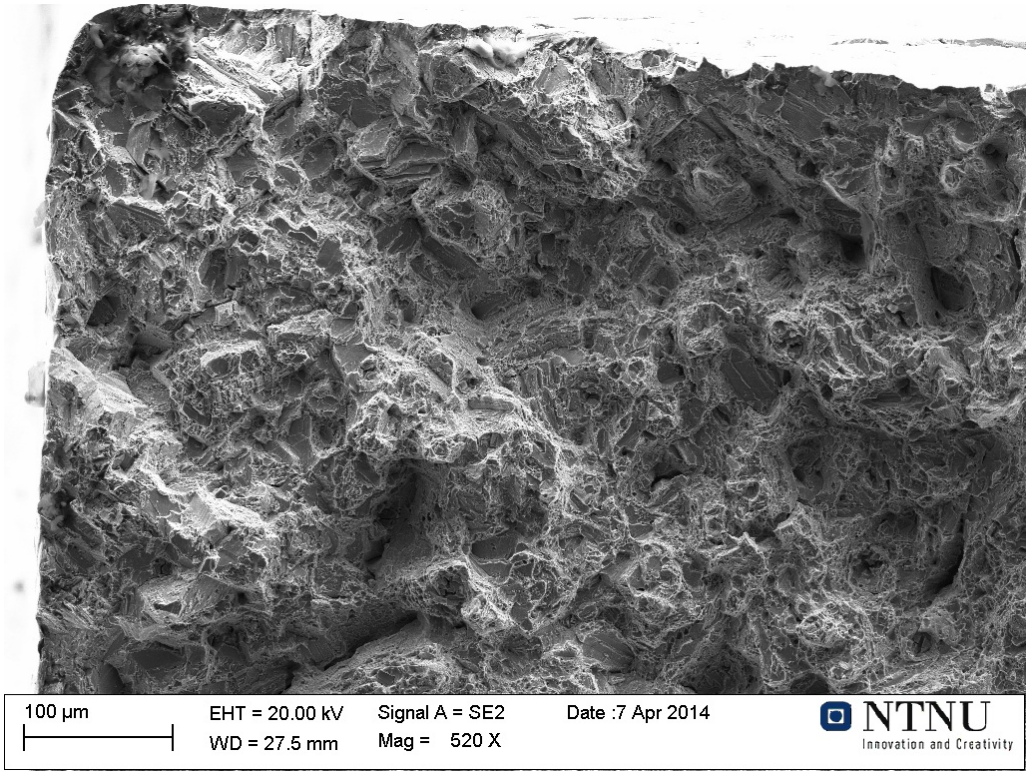

Figure 61: SEM image (520X) taken from 56LH-1-Piece-2 Sample-1 pre-charged with hydrogen. The image shows the IG fracture are close to the edge.

6.11.4 P3A01-1900

The fracture resulting from one of the pre-charged samples from P3A01-1900 (Sample-2) is shown in figure 62. The upper right area exhibits an IG fracture, with its facets and "rocky" features. The central areas of the fracture surface is dominated with dimpled fractures, characterized by a dimpled texture. A higher magnification image of the IG area is shown in figure 63, displaying the "rocky" texture more clearly. In contrast to the previous alloys presented, a significant proportion of the fracture areas from this alloy consisted of a mixture of IG fracture and extensive ductile slipping. One such area is displayed in figure 64, showing a fracture surface with significant embrittlement, yet with limited amounts of ductility even on the apparently brittle facets. A higher magnification image of this area is shown in figure 65, where the slip planes can be seen from the step-wise texture. The hydrogen free reference samples from this alloy exhibited a completely ductile fracture, similar to the fracture surface displayed in figure 57.

In summary, alloy P3A01-1900 also exhibits hydrogen embrittlement, as evident from the IG fracture areas around the edge. The fraction of embrittled area is also roughly the same as in the previously presented alloys. The alloy separates itself, as extensive slipping along discrete crystallographic planes appears to occur together with the IG fractures in the hydrogen effected areas. This might be a result of the reduced carbon and nitrogen content in this alloy. These interstitial elements are very effective dislocation pinners, and interfere with slip systems during deformation. Their absence may therefore be what enables extensive slipping along discrete crystallographic planes in this alloy.

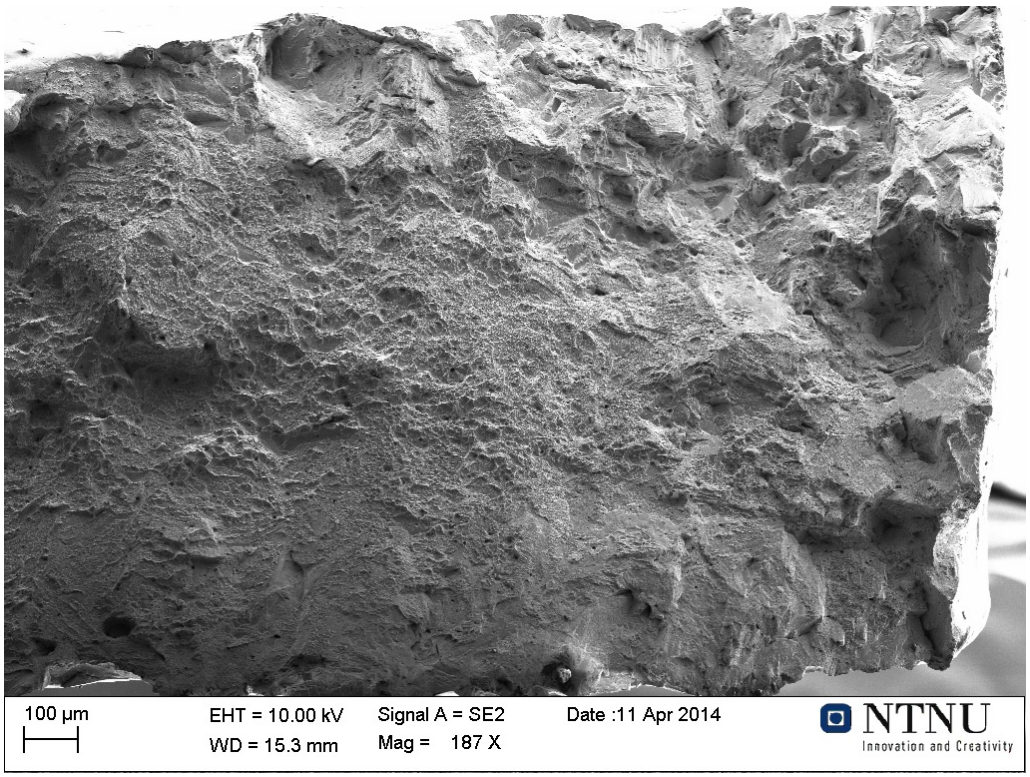

Figure 62: SEM image (187X) taken from P3A01-1900 Sample-2 pre-charged with hydrogen. IG features can be seen close to the edge.

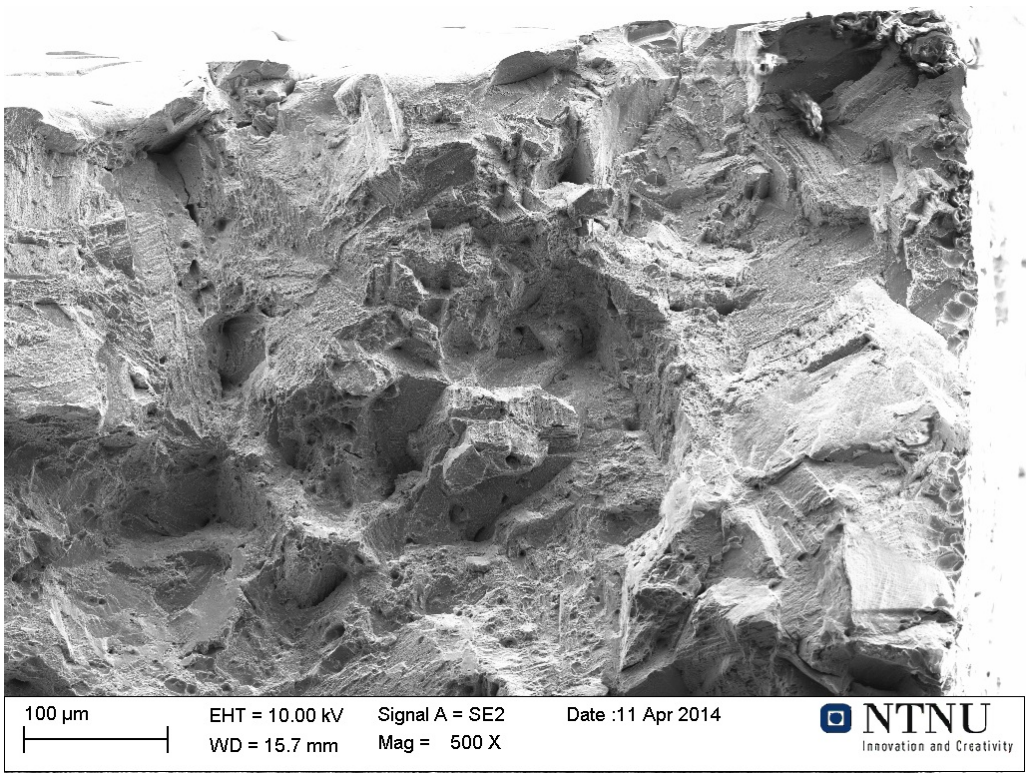

Figure 63: SEM image (500X) taken from P3A01-1900 Sample-2 pre-charged with hydrogen. IG features are seen from the "rocky" textures.

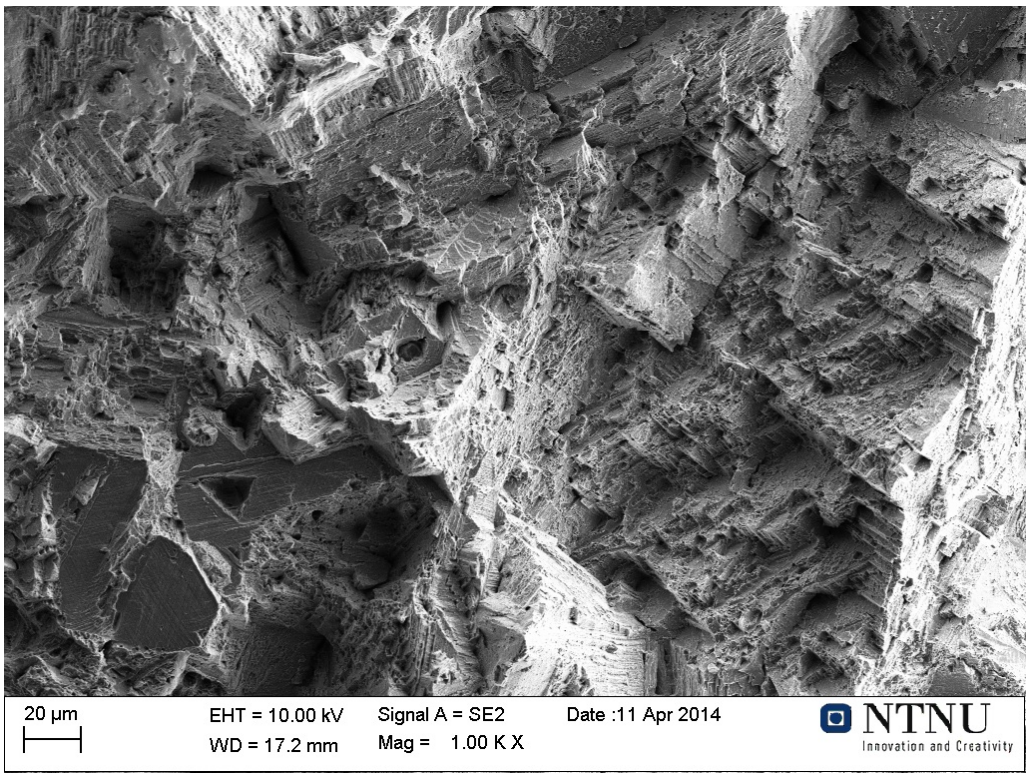

Figure 64: SEM image (1000X) taken from P3A01-1900 Sample-4 pre-charged with hydrogen. A mixture of IG fracture and extensive slipping can be seen.

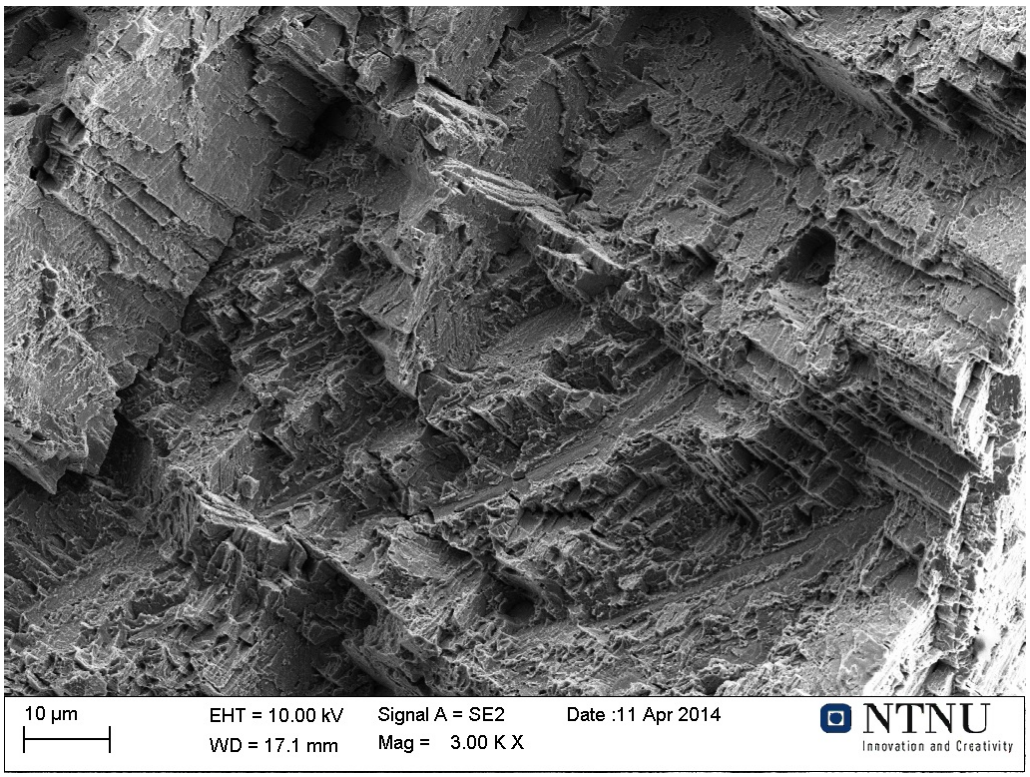

Figure 65: SEM image (3000X) taken from P3A01-1900 Sample-4 pre-charged with hydrogen. The slip planes can be seen from the "step-wise" texture.

6.11.5 P3A01-1850A

The fracture area resulting from one of the pre-charged samples from P3A01-1850A (Sample-2) is shown in figure 66. The image shows an IG fracture area in the lower part of the image, extending up towards the center of the fractured sample. Ductile areas are seen on the left and upper right areas. The IG fracture zone is seen extending a long way towards the centre of the fractured sample. Medium and higher magnification images of this IG fracture area are displayed in figure 67 and 68. The first picture shows the distinctive "rocky" texture that is typically observed from IG fractures. The second pictures shows a higher magnification of this area. Since the grains in alloy P3A01-1850A and P3A01-1800 are very small compared to the other alloys, the IG fracture areas can easily be mistaken for ductile dimples. Even the high magnification picture in figure 68 shows some resemblance of a ductile fracture surface. A true ductile fracture surface from P3A01-1850A is included in figure 69 for comparison. This picture also shows the broken particles left in some of the dimples, strong indicators of MVC. Comparing these image to the brittle zone shown in figure 68 suggests that the fracture surface in figure 68 could be a mixture of IG and ductile fractures. The central areas of the pre-charged samples and all the reference samples from P3A01-1850A exhibited ductile fractures like the one presented in figure 69.

In summary, alloy P3A01-1850A also shows embrittlement as a result of hydrogen pre-charging. Furthermore, the IG fractures seen in this alloy also extends much further into the fracture surface. This is believed to the result of the ultra fine grain size in this alloy, which enhances hydrogen diffusion along the GBs during pre-charging. This alloy also displays a very sharp shift from ductile to brittle fracture at the ductile - brittle transition. This can be a result of the numerous δ-particles scattered along the GBs in this alloy. These particles are associated with increased hydrogen embrittlement [26, 35, 36].

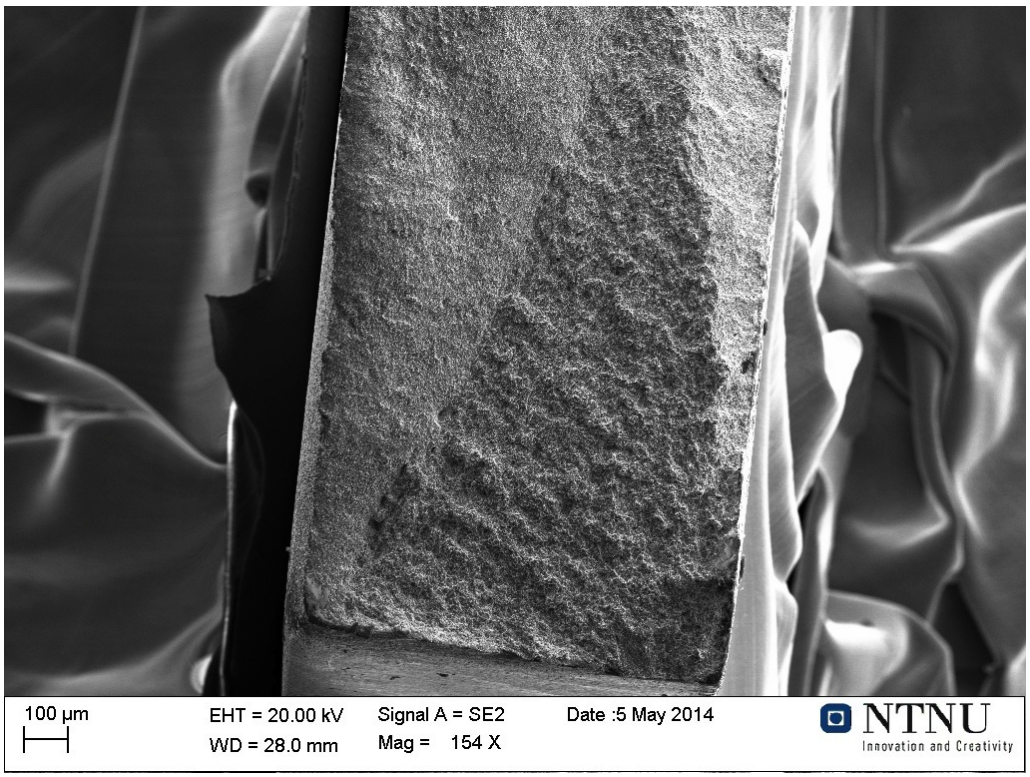

Figure 66: SEM image (154X) taken from P3A01-1850A Sample-4 pre-charged with hydrogen. An IG fracture area is seen extending from the bottom.

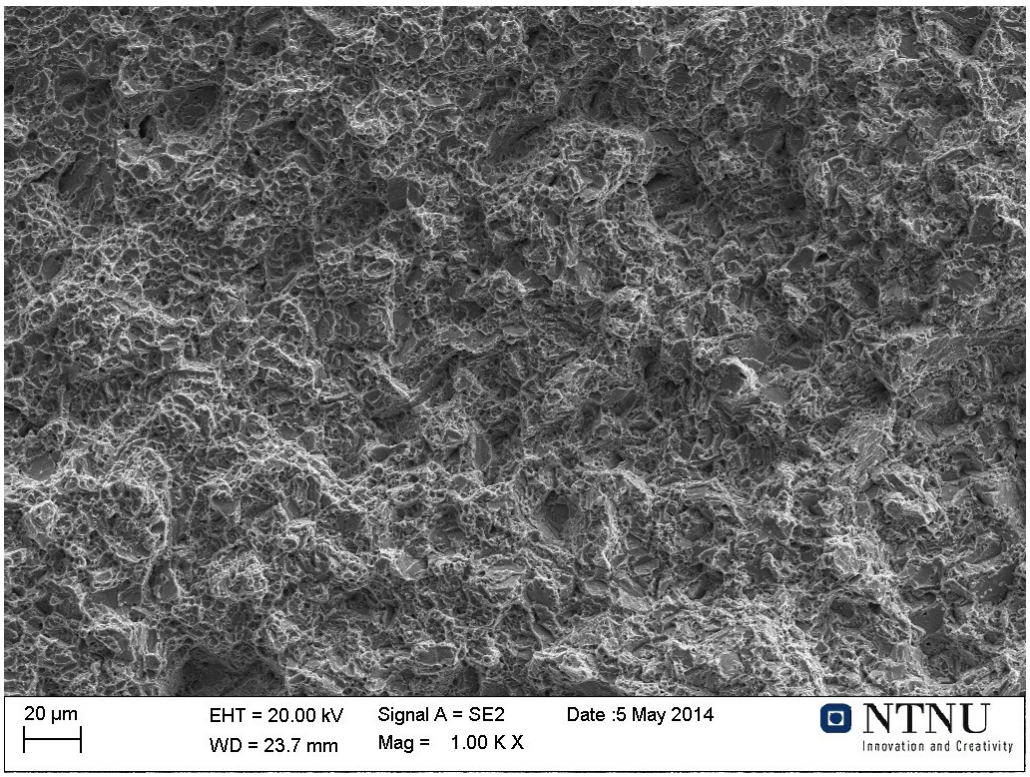

Figure 67: SEM image (1000X) taken from P3A01-1850A Sample-3 pre-charged with hydrogen. An image taken from the "rocky" IG fracture area.

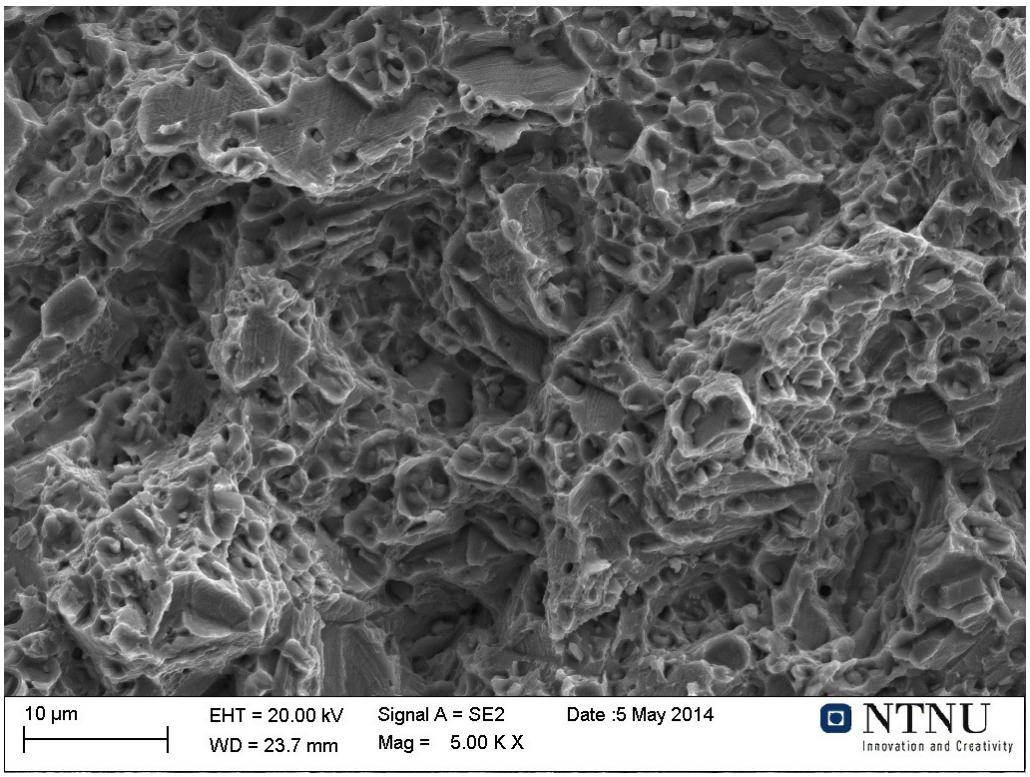

Figure 68: SEM image (5000X) taken from P3A01-1850A Sample-3 pre-charged with hydrogen. The IG area appears to be a mixture of IG and ductile features.

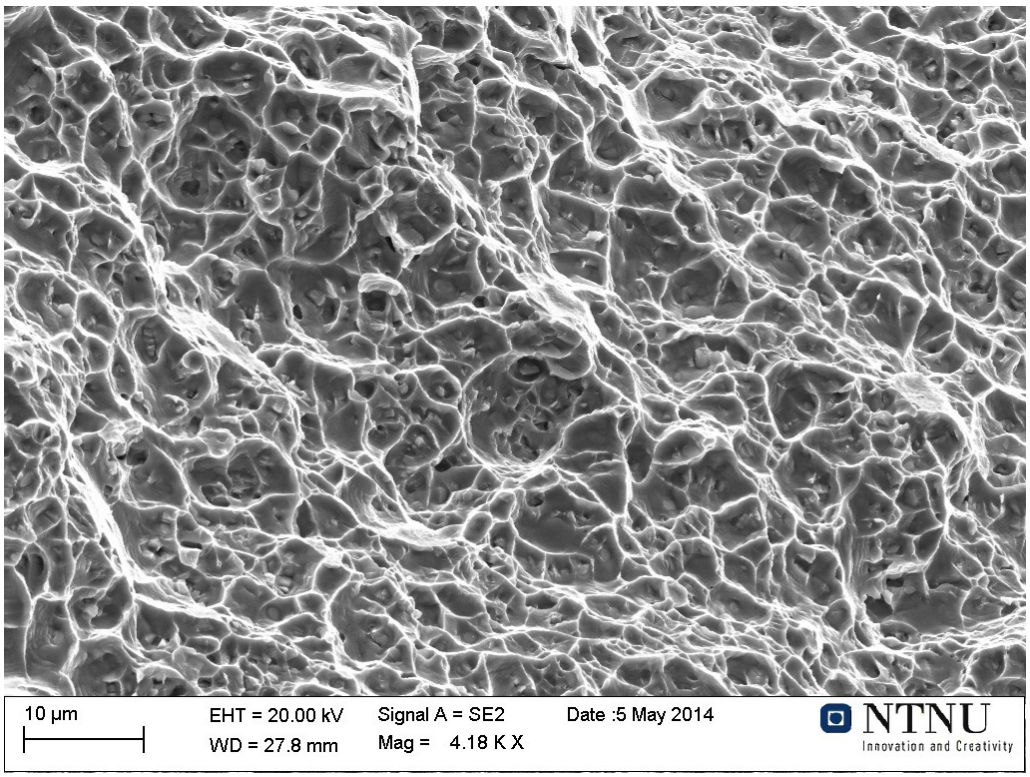

Figure 69: SEM image (4180X) taken from P3A01-1850A Sample-3 pre-charged with hydrogen. A completely ductile fracture from the central area is seen.

6.11.6 P3A01-1800

The fracture surface resulting from a pre-charged sample from P3A01-1800 (Sample-2) is shown in figure 70. With its ultra fine grain size, also this alloy shows the same very distinct areas of IG fractures. Higher magnification images of the IG fracture areas in P3A01-1800 are shown in figure 71 and 72. The fracture surfaces seen in these pictures are almost perfect textbook examples of IG fractures, with sharp faceted structures resulting from fracture along the GBs. When comparing the IG fracture seen in P3A01-1800 in figure 72 with the IG area observed in P3A01-1850A in figure 68, it appears that the P3A01-1800 alloy is even more embrittled than the P3A01-1850A alloy. The ductile fracture areas in both the pre-charged and hydrogen free samples of P3A01-1800 were completely ductile, and similar to the fracture surface presented in figure 69.

Just as the P3A01-1850A alloy did, the P3A01-1800 alloy showed a sharp transition from ductile to brittle IG fracture. The IG fracture depth is deep in this alloy as well, exceeding 1mm measured the left side in figure 70. The reasons for these features are the same as those proposed for P3A01-1850A, since their microstructures are the same.

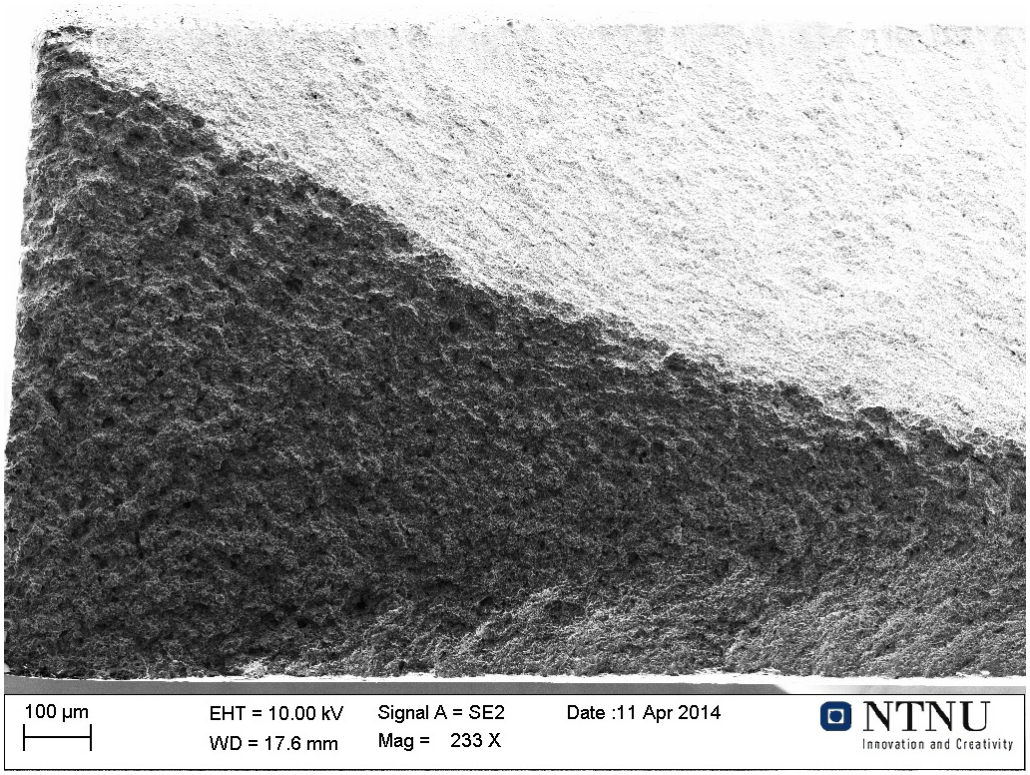

Figure 70: SEM image (233X) taken from P3A01-1800 Sample-2 pre-charged with hydrogen. An IG fracture area is seen to the left.

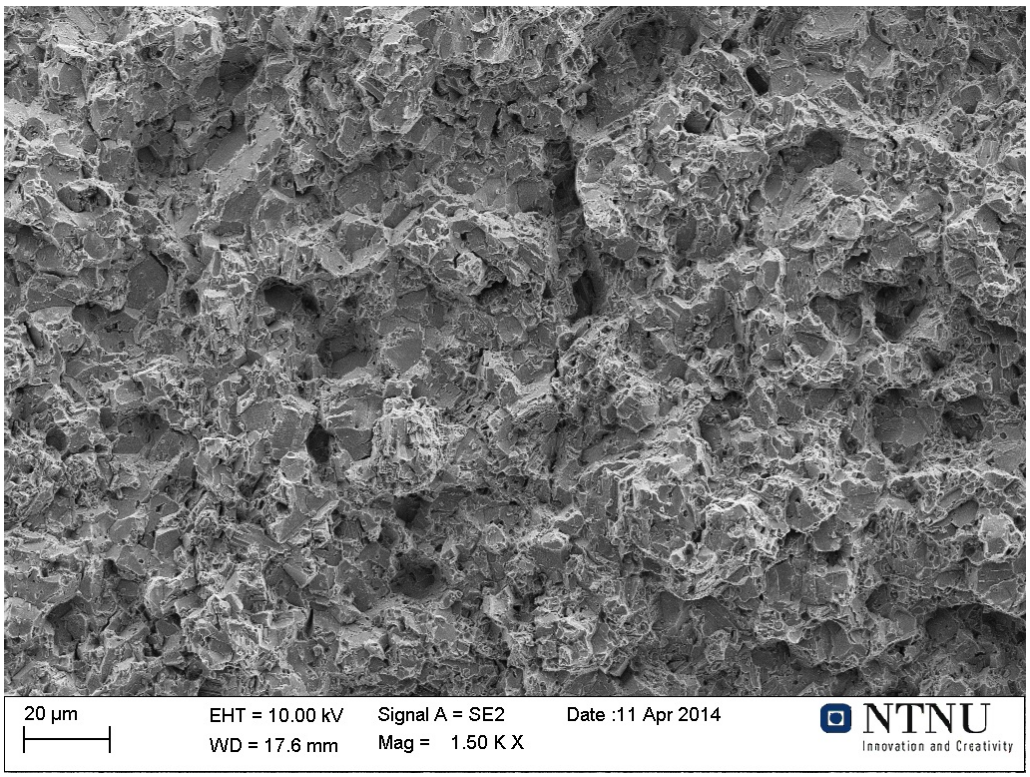

Figure 71: SEM image (1500X) taken from P3A01-1800 Sample-2 pre-charged with hydrogen. The IG fracture surface is identified form its "rocky" texture.

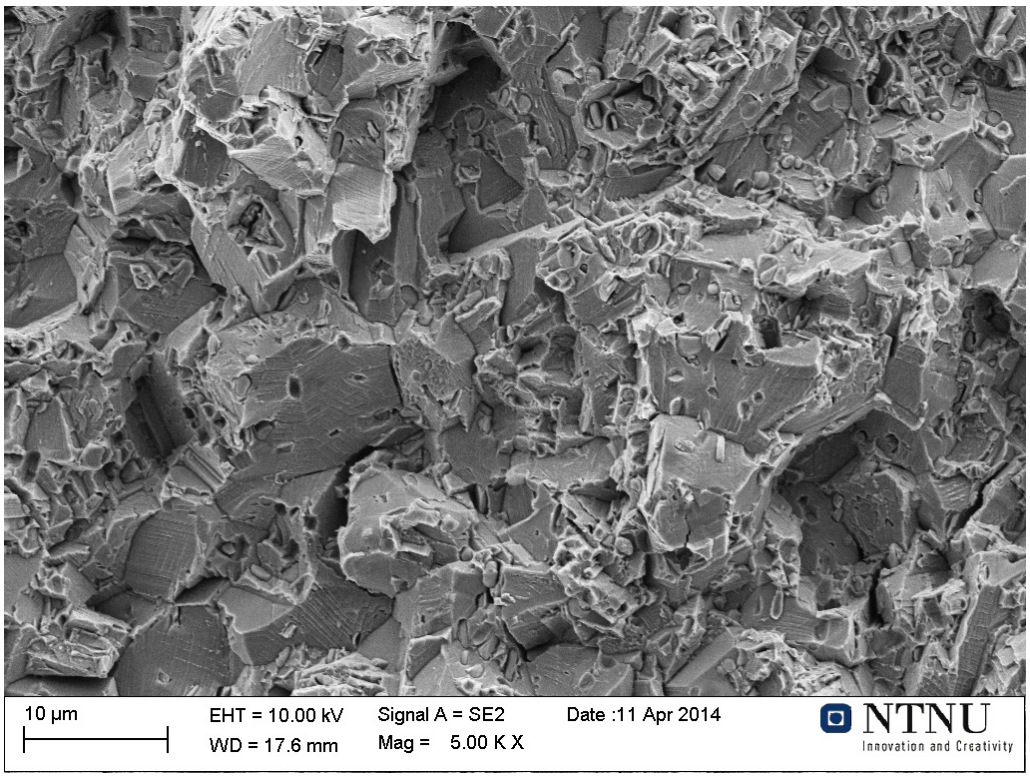

Figure 72: SEM image (5000X) taken from P3A01-1800 Sample-2 pre-charged with hydrogen. Under higher magnification, the IG fracture area is an almost perfect textbook example of an IG fracture, with sharp facets resulting from fracture along the GBs.

6.12 Depth if IG fracture

The depth of IG [38] fracture was examined in all of the fracture surfaces resulting from the pre-charged samples. On each sample the maximum IG depth was measured from all 4 sides of the sample. The depth of IG fracture in each samples was then defined as the average value of the non zero IG depths. In this way only the areas with IG fracture were included the IG depth statistics. Zero values resulting from IG free edges on the fracture surfaces are then excluded, and thereby prevented from causing an artificially high variance in the statistics. All the hydrogen effected fracture surfaces contained edges completely free of IG fractures. Adding zero values resulting from these areas were therefore not considered to contribute in any constructive way to the statistical image formed. The resulting IG depths measured are summarized in table 18. The results are also plotted in figure 73 together with the ASTM number measured in each alloy. The standard deviation measured in the samples are market through the error bars. The ASTM numbers are plotted on a secondary axis. Only the two extra samples from 56LH-1-Piece-1 are included in these statistics, since sample 1-4 did not show any IG fracture areas.

The significantly higher IG depths observed in the fine grained P3A01-1850A and P3A01-1800 alloys, indicate that these alloys have a much greater permeability with respect to hydrogen. This is probably the result of increased GB diffusion of hydrogen during pre-charging due to the ultra fine grain sizes in these alloys. This is supported by the almost perfect correlation between IG depth and the ASTM grain size number G seen in figure 73.

Table 18: Non-zero IG depths measured from the hydrogen effected fracture surfaces.

Sample nr:	56LH-1-OP	56LH-1-Piece-1	56LH-1-Piece-2	P3A01-1900	P3A01-1850A	P3A01-1800
1	294μm	308μm	550μm	273μm	1500μm	1481μm
2	333μm	355μm	302μm	303μm	1304μm	1889μm
3	264μm	-	575μm	203μm	1113μm	1296μm
4	424μm	-	271μm	-	1556μm	1526μm
Average	**326**μm	**331**μm	**397**μm	**260**μm	**1317**μm	**1548**μm
SD	**172**μm	**172**μm	**184**μm	**126**μm	**435**μm	**248**μm

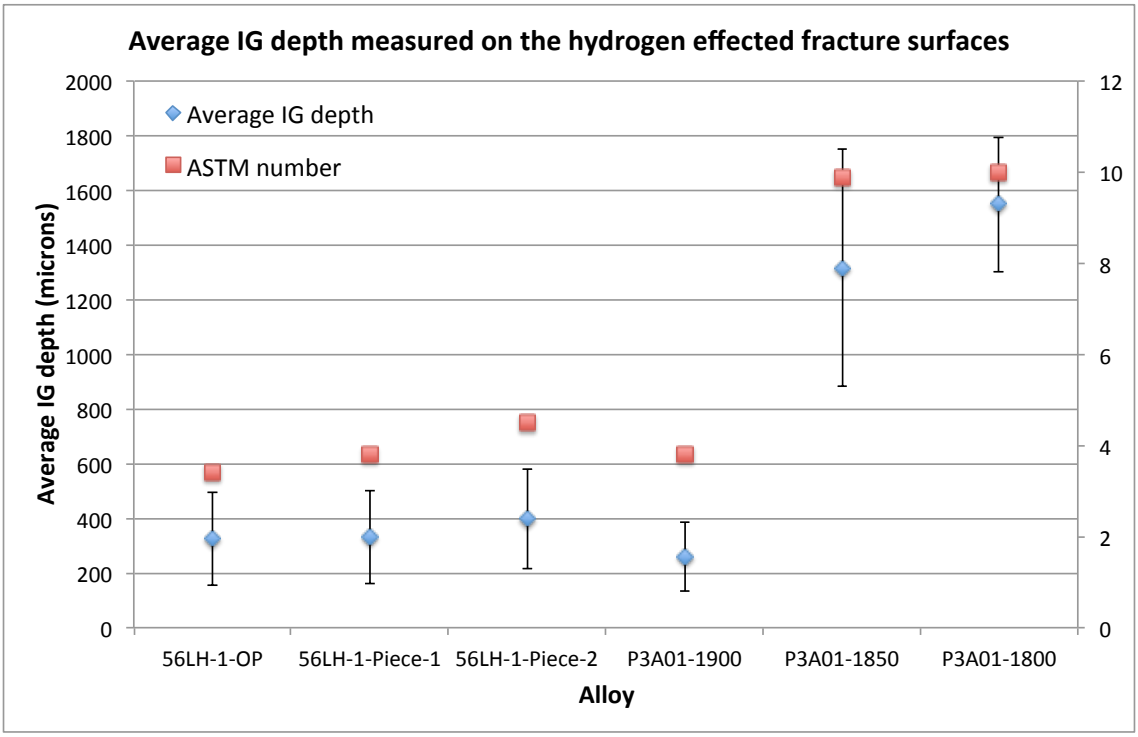

Figure 73: The average IG depth in μm from samples pre-charged with hydrogen (blue). The ASTM number is plotted on a secondary axis (red).

6.13 Secondary cracks examined in SEM

Fractured samples from both pre-charged and hydrogen free samples were examined for secondary cracks in SEM. Images obtained from the pre-charged and hydrogen free samples are displayed in figure 75a-75f and 74a-74f respectively. The difference in secondary cracking seen in the pre-charged samples relative to the reference samples can be seen clearly, as no cracks were found in the reference samples while all the fractured pre-charged samples contained secondary cracks. Most of the cracks identified had lengths of similar magnitude as the grain size in each alloy. Longer cracks were found in the course 56LH-1-OP, 56LH-1-Piece-1 and P3A01-1900 variants. The largest secondary cracks were found in the P3A01-1900 variant, where cracks exceeding 1mm were identified. The fine grained P3A01-1800/1850A variants contained fewer and much smaller secondary cracks, seen from the high magnification in figure 75f and 75d.

The secondary crack examinations show that hydrogen not only reduces the fracture strength and ductility, but that it also causes the initiation of numerous secondary cracks prior to fracture. This was also indicated by the in-situ OM picture presented earlier. Since secondary cracks may initiate and grow at lower stress levels than the fracture stress recorded in this thesis, they pose a potential threat to the integrity of an Inconel-718 component subjected to CP at high stresses.

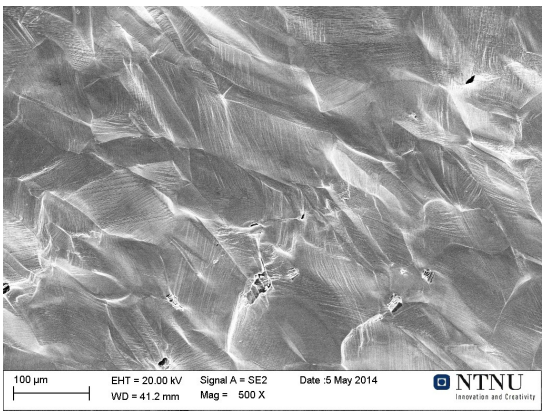

(a) 56LH-1-OP reference sample: SEM image (500x), no secondary cracks can be seen on the surface of the fractured sample.

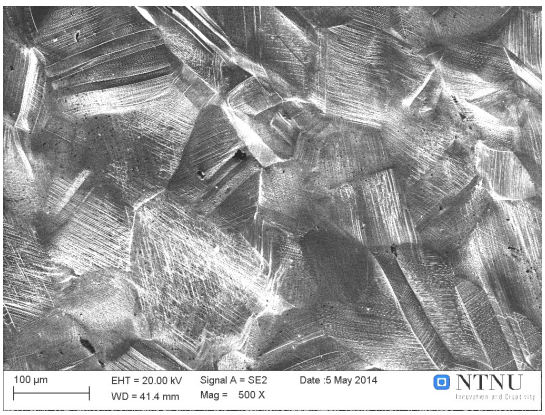

(b) P3A01-1900 reference sample: SEM image (500x), no secondary cracks are seen on the surface of the fractured sample.

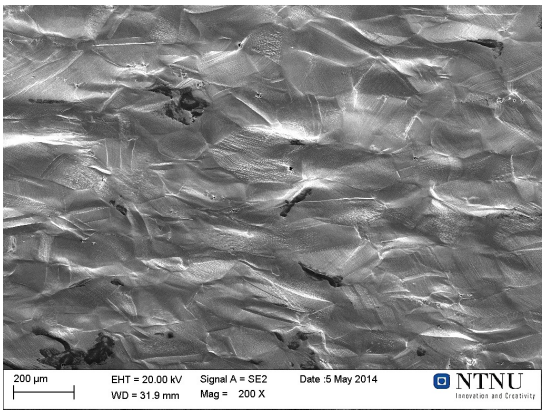

(c) 56LH-1-Piece-1 reference sample: SEM image (200x), no secondary cracks can been seen on the surface of the fractured sample.

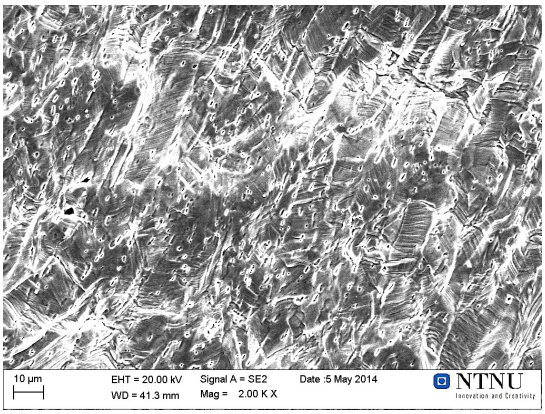

(d) P3A01-1850 reference sample: SEM image (2000x), no secondary cracks can been seen on the surface of the fractured sample.

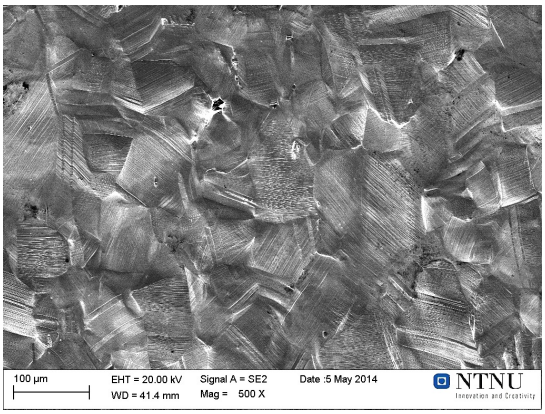

(e) 56LH-1-Piece-2 reference sample: SEM image (500x), little or no secondary cracks can been seen on the surface of the fractured sample.

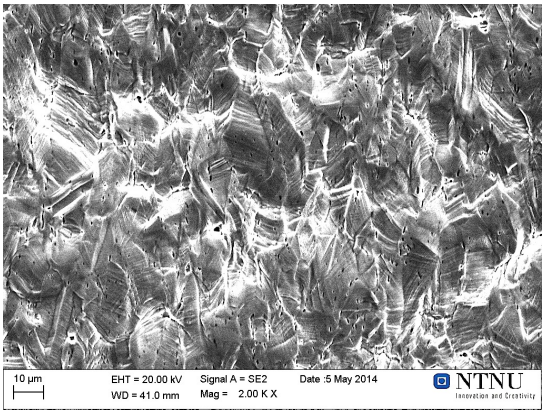

(f) P3A01-1800 reference sample: SEM image (500x), little or no secondary cracks can be seen on the surface of the fractured sample.

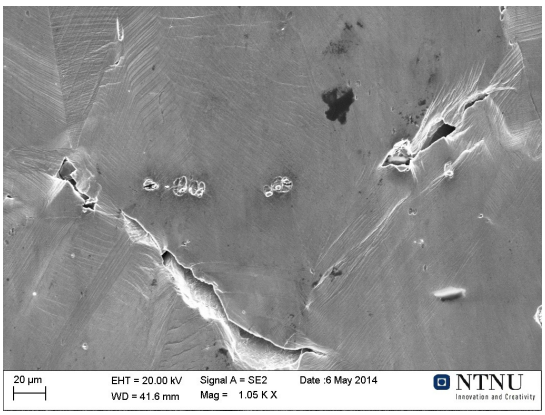

(a) 56LH-1-OP pre-charged sample: SEM image (1050X) showing inter granular secondary cracks.

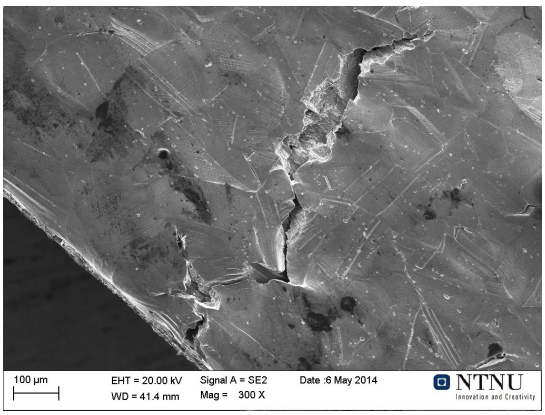

(b) P3A01-1900 pre-charged sample: SEM image (250X) showing inter granular secondary cracks.

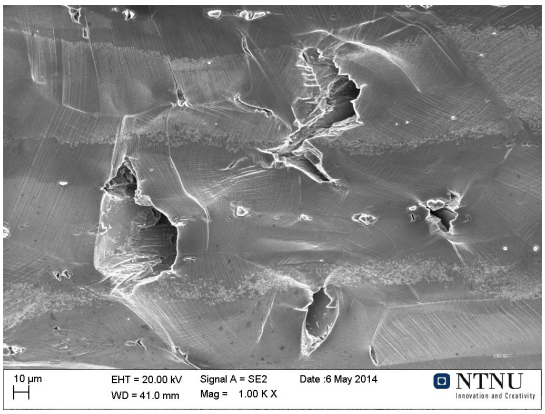

(c) 56LH-1-Piece-1 pre-charged sample: SEM image (1000X) showing inter granular secondary cracks.

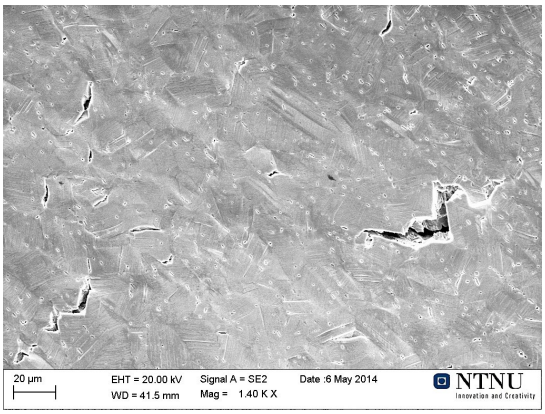

(d) P3A01-1850 pre-charged sample: SEM image (1400X) showing inter granular secondary cracks.

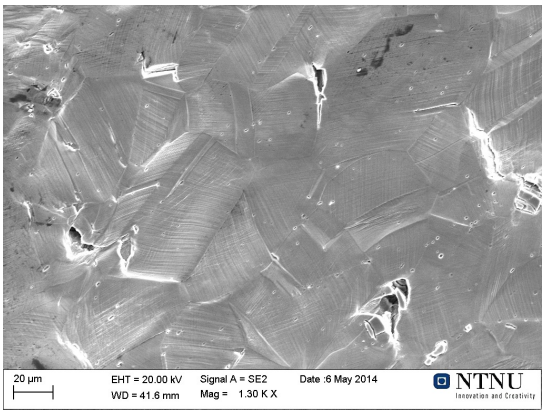

(e) 56LH-1-Piece-2 pre-charged sample: SEM image (1300X) showing inter granular secondary cracks.

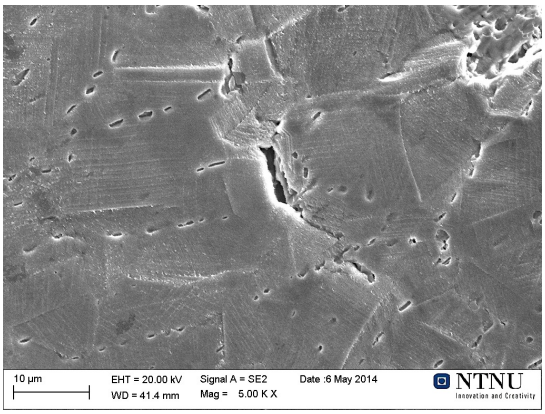

(f) P3A01-1800 pre-charged sample: SEM image (5000X) showing inter granular secondary cracks.

6.14 Hydrogen melt extraction analysis

After tensile testing, the pre-charged samples were stored in a freezer at -19°C. One sample from each alloy was selected for hydrogen melt extraction analysis at SINTEF. The purpose of these analysis was to explore wether the increased embrittlement in some of the microstructures were a result of more hydrogen absorption, or if the same amount of hydrogen weakened the microstructures more. The results from the hydrogen melt extraction tests are summarised in table 19. The values are also displayed graphically in figure 76.

For all the alloys except 56LH-1-Piece-1, the hydrogen concentrations seems to correlate nicely with the losses in ductility presented earlier. This indicates that the extra susceptibility seen in the fine-grained alloys may have more to do with the extra GB diffusion in these alloys than with the microstructures themselves.

All the samples pre-charged in this study were pre-charged as 4 samples in each pre-charging chamber. The 56LH-1-Piece-1 sample analysed was however one of the two extra samples from this alloy. These were pre-charged as 2 samples together in a pre-charging chamber. This might explain higher value measured in this sample.

Table 19: Hydrogen concentration in Wppm measured by hydrogen melt extraction at SINTEF

Alloy	56LH-1-OP	56LH-1-Piece-1	56LH-1-Piece-2	P3A01-1900	P3A01-1850A	P3A01-1800
Wppm	7.18	17.52	12.83	9.42	11.56	16.41

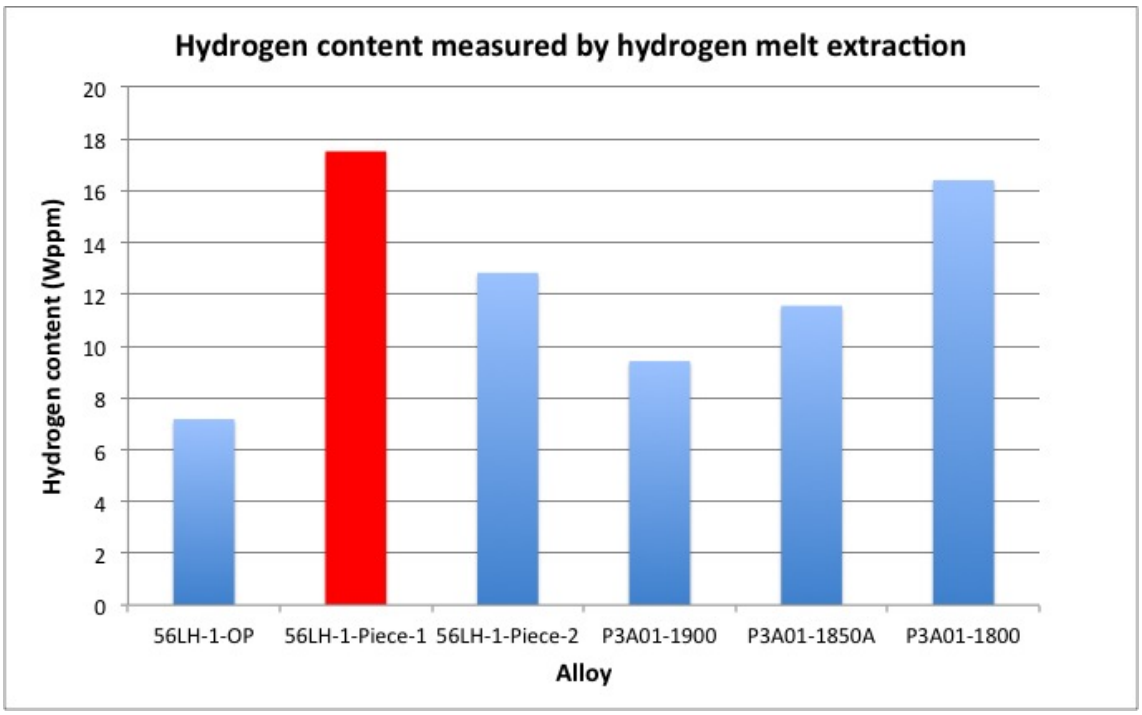

Figure 76: Graphical illustration of the Hydrogen Melt Extraction results. The value measured from the 56LH-1-Piece-1 sample has been marked in red, since the higher value is believed to be the result of the pre-charging conditions and not the microstructure itself.

7 Discussion

7.1 The effect of hydrogen on the mechanical properties of Inconel-718

All the pre-charged Inconel-718 samples showed a drop in the fracture stress of approximately 5-7% of YS, corresponding to a drop of in the range 50 - 100Mpa. This is only a moderate drop in fracture stress, as all the fracture stresses recorded were far above YS. No significant trend was observed between the alloy variants with respect to loss of fracture strengths. It should be noted that the polished samples used in this study means that the fracture stresses obtained are artificially high relative to samples with a more realistic roughness. The slow diffusion of hydrogen in Inconel-718 meant that only a portion of the sample cross sections were embrittled. Because of these points, the fracture strength of Inconel-718 may potentially drop even further if the samples had been saturated with hydrogen and a more realistic roughness had been introduced.

The embrittlement of Inconel-718 was seen best form the losses of elongation and RA. While only moderate drops in fracture strengths were recorded, losss of elongation and RA as high as 70% were observed in the alloys 56LH-1-Piece-2, P3A01-1850A and P3A01-1800. The losses in ductility showed a clear correlation with the grain sizes in the alloy variants. Finer grains were correlated with increased loss of elongation and RA. It was believed that the increased embrittlements seen in these alloys was the result of more GB diffusion of hydrogen occurring in these alloys during the pre-charging step. This was confirmed by the hydrogen melt extraction analysis. On the other hand it was observed that far less secondary cracking occurred in the pre-charged fine grained variants. This could be related to the fact that fine grained microstructures initially have a better fracture toughness, which resist the initiation of secondary crack better.

The effect of grain size on HISC in Inconel-718 therefore appears to be twofold; while finer grains results in better fracture toughness and less initiation of cracks, it also allows for increased GB diffusion of hydrogen. From the SEM observations of the fractured samples and the following IG depth measurements, it was shown that large areas of IG fracture can result from the increased GB diffusion of hydrogen. In the end, there is not much help in a better resistance to secondary cracking if a component fractures without plastic deformation during an overload as a result of IG fracture. The fine grained alloys examined in this study should therefore be avoided in components exposed to CP over longer periods of time.

Despite the moderate drop in fracture stress, the course grained variants 56LH-1-OP and 56LH-1-Piece-1 both fracture far above YS and with a substantial amount of plastic deformation prior to fracture. This means that these alloy are still far better choices than many stainless steel alternatives for components exposed to harsh environments and subjected to CP. As long as the component is not loaded above YS (or kept below, say 80% of YS as a precaution) and severe stress intensifiers are avoided in the design, hydrogen embrittlement should not be a problem. The problem arises however if a component is accidentally overloaded after years of service, or if stress intensifiers are present to raise the stress higher than the YS locally. Hydrogen embrittlement should then be considered as a potential threat to the component.

Since cold creep is effectively a form of plastic deformation, it can be argued that dislocation movement resulting from cold creep could assist hydrogen transport and embrittlement according to the HELP mechanism. The accidental overload discussed in the "Other tensile results" subsection gave some hint that cold creep may be an important contributing factor to HISC in Inconel-718. If HISC fractures can be prevented by shakedown treatments prior to installation, it would certainly be worth looking into.

7.2 The effect of hydrogen on the cracking and fracture behaviour of Inconel-718

All the pre-charged samples showed areas of IG fracture, while all the reference samples fractured in a completely ductile manner. The IG fracture areas were observed close to the edges were the hydrogen concentration is expected to be largest. IG fractures are caused by the hydrogen atoms segregated at the GBs, since the seggregated hydrogen atoms results in localized plasticity and early fracture according to the HELP mechanism.

In the pre-charged samples, extensive secondary cracking also occurred. These cracks initiated at stress levels lower than the fracture stresses measured. The secondary cracks were observed in the in-situ optical microscope pictures and from the secondary cracks observed in SEM. Most of the secondary cracks examined were IG, but some cracks also initiated at secondary particles. In-situ time-lapse videos were obtained, showing cracks propagating to failure during CP in seawater. These videos demonstrate how hydrogen evolves from the newly formed crack tips, potentially causing more embrittlement. The amount of secondary cracking was largest in the course grained alloys, while very little secondary cracks were observed in the fine grained P3A01-1850A and P3A1-1800 variants. This was attributed to the higher intrinsic fracture toughness expected in fine grained microstructures.

Alloy P3A01-1900 (High Nb, low C/N) was compared with the commercial grade 56LH-1-OP (standard composition) to examined the effect of the high Nb low C/N content. Unusually large secondary cracks were observed in the fractured P3A01-1900 samples which had been pre-charged. This alloy had the largest secondary cracks by far, with multiple secondary cracks exceeding 1mm. The secondary cracks observed in the 56LH-1-OP alloy was no where close to these lengths, with typical lengths of 100, 200 and 300μm. The increased amount of secondary cracking in P3A01-1900 was attributed to the absence of C and N at the GBs: These interstitial

elements will often be segregated at the GBs, and can occupy sites where hydrogen otherwise would have been located. The absence of C and N therefore leaves more room for hydrogen atoms which can result in more secondary cracks. Despite the large secondary cracks, alloy P3A01-1900 did not behave any different than 56LH-1-OP with respect to loss of fracture strength, RA and elongation. This suggests that the effect of the high Nb low C/N composition is only minor.

7.3 Further work

Since the relationship between cold creep and hydrogen embrittlement in Inconel-718 has not been examined yet, it would be a natural topic for future work. To establish this relationship is important since cold creep can occur slightly below YS as well. The accidental overload of one of the 56LH-1-OP gave some hint that an overload shakedown can be one possible approach to achieve better HISC resistance in Inconel-718. This is an interesting concept which should be investigated and documented, as it provides a potential way to reduce the embrittlement resulting from hydrogen in Inconel-718.

Because of the slow diffusivity in Inconel-718, time becomes an important factor. It can therefore be difficult to access wether the Inconel-718 is safe against HISC or not. In order to develop a more complete understanding of the HISC susceptibility of Inconel-718, more comprehensive modelling tools are needed. A hydrogen transport model of a stressed Inconel-718 component could be one place to start. This model should incorporate the diffusion of hydrogen in a stress gradient field as well as the transportation of hydrogen atoms by dislocation movements resulting from cold creep. Once the concentration profile resulting from a given load, geometry, temperature and time can be predicted accurately, it can be combined by the K_{Ic} - H[Wppm] relationship established by Hicks [25] to calculate the distribution of local fracture toughnesses. This distribution can then be in fracture mechanic models to assess the integrity and reliability of the Inconel-718 component.

The goals described require a lot of experimental and theoretical work to be accomplished. The diffusion model will have to be fitted to experimental data from hydrogen diffusion in stress gradients, and the surface fugacity of hydrogen at various galvanic potentials also has to be determined. Such a model will nevertheless be a valuable tool, as it can be used predict the HISC susceptibility of an Inconel-718 component subjected to CP.

8 Conclusion

- Hydrogen embrittlement occurred in all the Inconel-718 variants tested. The embrittlement was seen from the IG fracture surfaces examined in the SEM.
- Hydrogen embrittlement resulted in a moderate loss in fracture stress corresponding to around 5-7% of YS. This number may increase if the pre-charging time is increased or if a surface roughness is introduced.
- Finer grains were correlated with higher ductility losses in the presence of hydrogen. RA_{loss} and ϵ_{loss} values as high as 70% were measured from the fine grain variants 56LH-1-Piece-2, P3A01-1850A and P3A01-1800.
- The severe embrittlement of the fine grained microstructures were attributed to increased GB diffusion of hydrogen during pre-charing. This was confirmed by the hydrogen melt extraction analysis.
- Secondary cracking were observed in the pre-charged samples from all the Inconel-718 variants. These cracks typically initiated at 8-12% YS below the final fracture stress and were mostly IG type cracks.
- Little effect of reduced C/N and increased Nb content was observed on the loss of fracture strength, RA and elongation. The high Nb low C/N P3A01-1900 alloy did however show much larger secondary cracks, which may be linked to the absence of C/N and the GBs.
- In-situ time lapse videos of crack propagation during CP in saltwater were obtained. The videos show the the evolution of hydrogen from the propagating crack as it progresses to failure.
- Suggestions for further work are: Establishment of the relationship between HISC and cold creep in Inconel-718, the construction of a hydrogen transport model which incorporates both the diffusion of hydrogen in a stress field and hydrogen transport through cold creep.

References

[1] Kjetil Andersen. Hisc in super duplex stainless steel. Master's thesis, Norwegian University of Science and Technology NTNU, 2013.

[2] Saied Azadian, Liu-Ying Wei, and Richard Warren. Delta phase precipitation in inconel 718. *Materials Characterization*, 53(1):7–16, 2004.

[3] J. Bauschinger. "ueber die verandarung der elasticitategrenze and dea elastitiatamoduls verschiadener metalle". *Zivilingenieur*, 27:289–348, 1881.

[4] S. Bechtle, M. Kumar, B. P. Somerday, M. E. Launey, and R. O. Ritchie. Grain-boundary engineering markedly reduces susceptibility to intergranular hydrogen embrittlement in metallic materials. *Acta Materialia*, 57(14):4148–4157, 2009.

[5] H. K. Birnbaum and P. Sofronis. Hydrogen-enhanced localized plasticitya mechanism for hydrogen-related fracture. *Materials Science and Engineering: A*, 176(12):191–202, 1994.

[6] R. D. Calder, T. S. Elleman, and K. Verghese. Grain boundary diffusion of tritium in 304- and 316-stainless steels. *Journal of Nuclear Materials*, 46(1):46–52, 1973.

[7] John J. Schirra Robert H. Caless and Robert W. Hatala. The effect of laves phase on the mechanical properties of wrought and cast+hip inconel-718. *TMS*, Superalloys 718, 625, and various derivatives.:375–388, 1991.

[8] Bonis M Cassagne T and Duret C. Understanding field failures of alloy 718 forging materials in hp/ht wells. In *Eurocorr2008*, 2008.

[9] CEN. Materials for use in h_2s-containing environments in oil and gas production. part 3: Cracking resistant cras (corrosion resistant alloys) and other alloys, 2009.

[10] C. E. Coleman and D. Hardie. The hydrogen embrittlement of -zirconium, a review. *Journal of the Less Common Metals*, 11(3):168–185, 1966.

[11] Gran Sjberg Cornu and Daniel. Hydrogen embrittlement of cast alloy 718, effects of homogenization, grain size and δ - phase. *TMS*, Superalloy 718, 625, 706 and various derivatives - 2001:12, 2001.

[12] D. L. Dull and L. Raymond. Surface cracking of inconel 718 during cathodic charging. *Metallurgical Transactions*, 4(6):1635–1637, 1973.

[13] Zhongyun Fan. The grain size dependence of ductile fracture toughness of polycrystalline metals and alloys. *Materials Science and Engineering: A*, 191(12):73 – 83, 1995.

[14] P. J. Ferreira, I. M. Robertson, and H. K. Birnbaum. Hydrogen effects on the interaction between dislocations. *Acta Materialia*, 46(5):1749–1757, 1998.

[15] D. Fournier and A. Pineau. Low cycle fatigue behavior of inconel 718 at 298 k and 823 k. *Metallurgical Transactions A*, 8(7):1095–1105, 1977.

[16] L. Fournier, D. Delafosse, and T. Magnin. Cathodic hydrogen embrittlement in alloy 718. *Materials Science and Engineering: A*, 269(12):111–119, 1999.

[17] F.P.Cone. Observation of the development of delta phase in in718 alloy. *TMS*, Superalloy 718, 625, 706 and various derivatives - 2001:10, 2001.

[18] M. Srinivas G. Appa Rao, Mehendra Kumar and D.S. Sarma. Effect of solution treatment temperature on the microstructure and tensile properties of p/m (hip) processed superalloy inconel 718. *TMS*, Superalloy 718, 625, 706 and various derivatives - 2001:12, 2001.

[19] V.A. Valitov O.A. Kaibyshev Sh. Kh. Mukhtarov B.P Bewlay M.F.X Gigliotti. Processing and properties of microcrystalline, submicrocrystalline and nanocrystalline alloy 718. *TMS*, Superalloy 718, 625, 706 and various derivatives - 2001, 2001.

[20] Carlos Ruiz Abel OObabueki Kathy Gillespie. Evaluation of the microstructure and mechanical properties of delta processed alloy 718. *TMS*, Superalloys - 1992:10, 1992.

[21] Ulrike Habel. Microstructure and mechanical properties of hip pm 718. *TMS*, Superalloy 718, 625 and various derivatives - 1991, 1991.

[22] E. O. Hall. The deformation and ageing of mild steel: III discussion of results. *Proc. Phys. Soc.*, 643:747–752, 1951.

[23] Jianhong He, Seiji Fukuyama, Kiyoshi Yokogawa, and Akihiko Kimura. Effect of hydrogen on deformation structure of inconel 718. *Materials Transactions, JIM*, 35(10):689–694, 1994.

[24] P. D. Hicks and C. J. Altstetter. Internal hydrogen effects on tensile properties of iron- and nickel-base superalloys. *Metallurgical Transactions A*, 21(1):365–372, 1990.

[25] P. D. Hicks and C. J. Altstetter. Hydrogen-enhanced cracking of superalloys. *Metallurgical Transactions A*, 23(1):237–249, 1992.

[26] Akio Hirose, Yoshihiro Arita, Yasumasa Nakanishi, and Kojiro F. Kobayashi. Decrease in hydrogen embrittlement sensitivity of inconel 718 by laser surface softening. *Materials Science and Engineering: A*, 219(1–2):71–79, 1996.

[27] ASTM International. Standard test method for determining average grain size. pages 1–27, 2012.

[28] NACE international. Laboratory testing of metals for resistance to sulfide stress cracking and stress corrosion cracking in h_2s environments, 1996.

[29] L.A. Jackman J.L. Russell, M.L.Lasonde. Microstructural development and thermal response of delta processed billet and bar for alloy 718. *TMS*, Superalloy 718, 625, 706 and various derivatives - 2005:10, 2005.

[30] Ulf Kiviskk. Relation of room temperature creep and microhardness to microstructure and {HISC}. *Materials Science and Engineering: A*, 527(2930):7684 – 7688, 2010.

[31] S. Koike and T. Suzuki. An electron microscopic study of hydrogen embrittlement in vanadium ii. *Acta Metallurgica*, 29(3):553–565, 1981.

[32] R. G Thompson M. C. Koopman and B. H. King. Grain boundary chemestry of alloy 718-type alloys. *TMS*, Superalloys 718, 625 and various derivatives - 1991:18, 1991.

[33] Roy Johnsen Brd Nyhus Stig Wstberg Gro . Lauvstad. New improved method for hisc testing of stainless steels under cathodic protection. In *Corrosion Conference and Expo CORROSION 2007*, March 2007.

[34] Hwa-Teng Lee and Wen-Hsin Hou. Development of fine-grained structure and the mechanical properties of nickel-based superalloy 718. *Materials Science and Engineering: A*, 555(0):13 – 20, 2012.

[35] Liufa Liu, Katsumi Tanaka, Akio Hirose, and Kojiro F. Kobayashi. Effects of precipitation phases on the hydrogen embrittlement sensitivity of inconel 718. *Science and Technology of Advanced Materials*, 3(4):335–344, 2002.

[36] Liufa Liu, Chunquan Zhai, Chen Lu, Wenjiang Ding, Akio Hirose, and Kojiro F. Kobayashi. Study of the effect of δ phase on hydrogen embrittlement of inconel 718 by notch tensile tests. *Corrosion Science*, 47(2):355–367, 2005.

[37] S. P. Lynch. Metallographic contributions to understanding mechanisms of environmentally assisted cracking. *Metallography*, 23(2):147–171, 1989.

[38] Stan P Lynch. Mechanisms of intergranular fracture. In *Materials Science Forum*, volume 46, pages 1–24. Trans Tech Publ, 1991.

[39] A. Mitchell. Melting processes and solidification in alloys 718-625. *TMS*, Superalloys 718, 625 and various derivatives - 1991:13, 1991.

[40] E. Nes, N. Ryum, and O. Hunderi. On the zener drag. *Acta Metallurgica*, 33(1):11 – 22, 1985.

[41] Bjrn-Andreas Hugaas Odd Hauks-Eide and Espen Heier. Effect of plastic deformation on hydrogen induced cracking (hisc) in duplex stainless steel. In *Corrosion Conference and Expo CORROSION 2007*, March 2007.

[42] R. A. Oriani and P. H. Josephic. Testing of the decohesion theory of hydrogen-induced crack propagation. *Scripta Metallurgica*, 6(8):681–688, 1972.

[43] R. A. Oriani and P. H. Josephic. Equilibrium aspects of hydrogen-induced cracking of steels. *Acta Metallurgica*, 22(9):1065–1074, 1974.

[44] N. J. Petch. The cleavage strength of polycrystals. *J. Iron Steel Inst.*, 173:25–28, 1953.

[45] B. G. Pound. Hydrogen trapping in precipitation-hardened alloys. *Acta Metallurgica et Materialia*, 38(12):2373–2381, 1990.

[46] Armida Oradei Radavich and J. F. A current t-t-t diagram for wrought alloy 718. *TMS*, Superalloys 718, 625 and various derivatives:11, 1991.

[47] I. M. Robertson. The effect of hydrogen on dislocation dynamics. *Engineering Fracture Mechanics*, 64(5):649–673, 1999.

[48] I. M. Robertson, T. Tabata, W. Wei, F. Heubaum, and H. K. Birnbaum. Hydrogen embrittlement and grain boundary fracture. *Scripta Metallurgica*, 18(8):841–846, 1984.

[49] W. M. Robertson. Hydrogen permeation and diffusion in inconel 718 and incoloy 903. *Metallurgical Transactions A*, 8(11):1709–1712, 1977.

[50] R.J. Siddall. Comparison of the atributes of vim + esr. *TMS*, Superalloys 718, 625 and various derivatives - 1991:13, 1991.

[51] C. Slama and M. Abdellaoui. Structural characterization of the aged inconel 718. *Journal of Alloys and Compounds*, 306(12):277 – 284, 2000.

[52] P. Sofronis and I. M. Robertson. Atomistic scale experimental observations and micromechanical/continuum models for the effect of hydrogen on the mechanical behavior of metals. *Urbana*, 51:61801, 2001.

[53] M. Sundararaman, P. Mukhopadhyay, and S. Banerjee. Deformation behaviour of strengthened inconel 718. *Acta Metallurgica*, 36(4):847 – 864, 1988.

[54] T. Tsuru and R. M. Latanision. Grain boundary transport of hydrogen in nickel. *Scripta Metallurgica*, 16(5):575–578, 1982.

[55] Viggo Tvergaard. Material failure by void growth to coalescence. volume 27 of *Advances in Applied Mechanics*, pages 83 – 151. Elsevier, 1989.

[56] AntonJ West and MacIntyreR Louthan. Dislocation transport and hydrogen embrittlement. *Metallurgical Transactions A*, 10(11):1675–1682, 1979.

[57] J. Yao and S. A. Meguid. Hydrogen diffusion and intergranular cracking in nickel. *International Journal of Hydrogen Energy*, 22(1011):1021–1026, 1997.

[58] Yuan Yao, Xiaolu Pang, and Kewei Gao. Investigation on hydrogen induced cracking behaviors of ni-base alloy. *International Journal of Hydrogen Energy*, 36(9):5729–5738, 2011.

[59] Seiji Fukuyama Yokagawa and Kiyoshi. Effect of heat treatment on hydrogen enviornment embrittlement of alloy 718. *TMS*, Superalloy 718, 625, 706 and verious derivatives - 1994:10, 1994.

[60] C. Zener. Fracturing of metals. *ASM*, page 3, 1948.

A PC - Chamber design

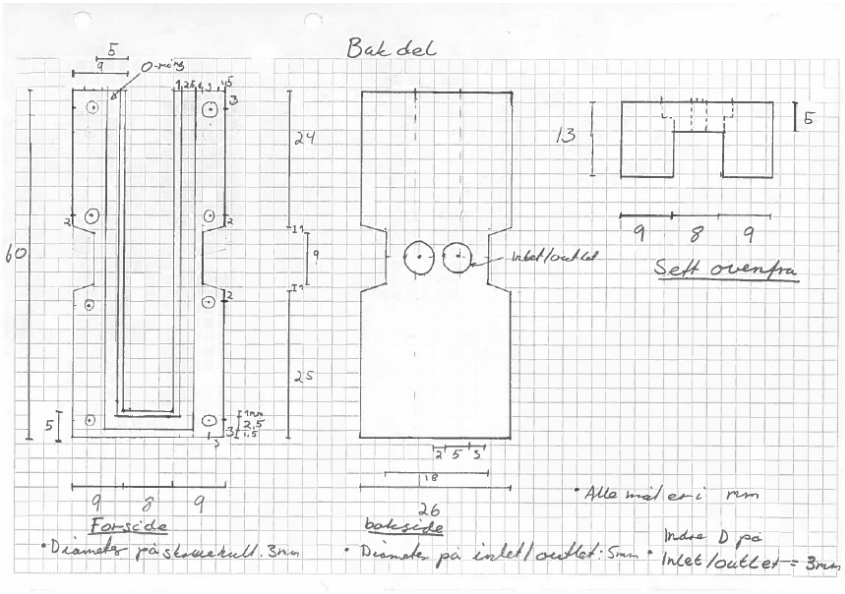

Figure 77: Design sketch, showing the backside of the electrolyte chamber

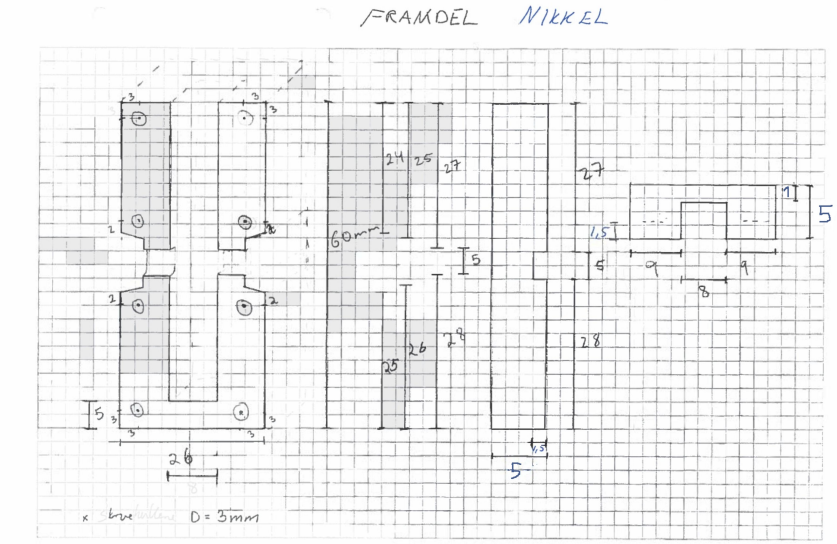

Figure 78: Design sketch, showing the front side of the electrolyte chamber

B Stress - strain curves received from ATI metals

SAMPLE FOLLOWER SHEET

100074 hmf 9-16-05

Stamp and Cut Samples as Follows

M.O.T. ~~100174~~
Project Number
Date

Sizes	Stamp	Cut
<1" x 8"	Single	None
>1" x 7"	Double	Two Halves
>6" < 12"	Double	Two Halves
>12" < 18"	Triple	One Half and Two Quarters
≥18"	Quadruple	To Yield Slices <6" in any Direction

Deck Seq.	Dept.	Oper.	M.I.	Prod. Code

NOTE WEIGHTS PER T.I.SPR: No sample or sample section may weigh more than 20 lbs. max for heat treat; 50 lbs. max for saw in lab.

TO BE COMPLETED BY ORIGINATOR

Alloy 135 Size R08 Heat Number See SFS
Specification(s) Heat Treat
DDR no. (if applicable)

Mech Lab

1. Please run seven RTT's.
2. Return broken tensiles.
3. Call Trey Prince x7130 to pick up.

Batch: EAS-100074 Heat: See SFS Sub Id: 100026213

ample ID	Dir/Loc	Task	Piece ID	P/F
00053958	L	RTT		A
00053960	L	RTT		A
00053961	L	RTT		A
00053962	L	RTT		A
00053963	L	RTT		A
00053964	L	RTT		A

Batch: EAS-100074
Heat: See SFS Ingot:
Chem Spec: 999 PC:
Size Desc:
Customer:
Sample Plan: SFS
Comments:
Ship Date:

Batch: EAS-100074 Heat: See SFS Sub Id: 100026213

ample ID	Dir/Loc	Task	Piece ID	P/F
00053965	L	RTT		A

(H:\WORD\TREY SAMPLE FOLLOWER SHEET-8-11-05.DOC)

Results for Certification: No xx Copies To:
Originator: Trey Prince

QF-315-120 rev. 16 (8/11/2005) Page 1 of 1

Figure 79: Tensile test data received from ATI

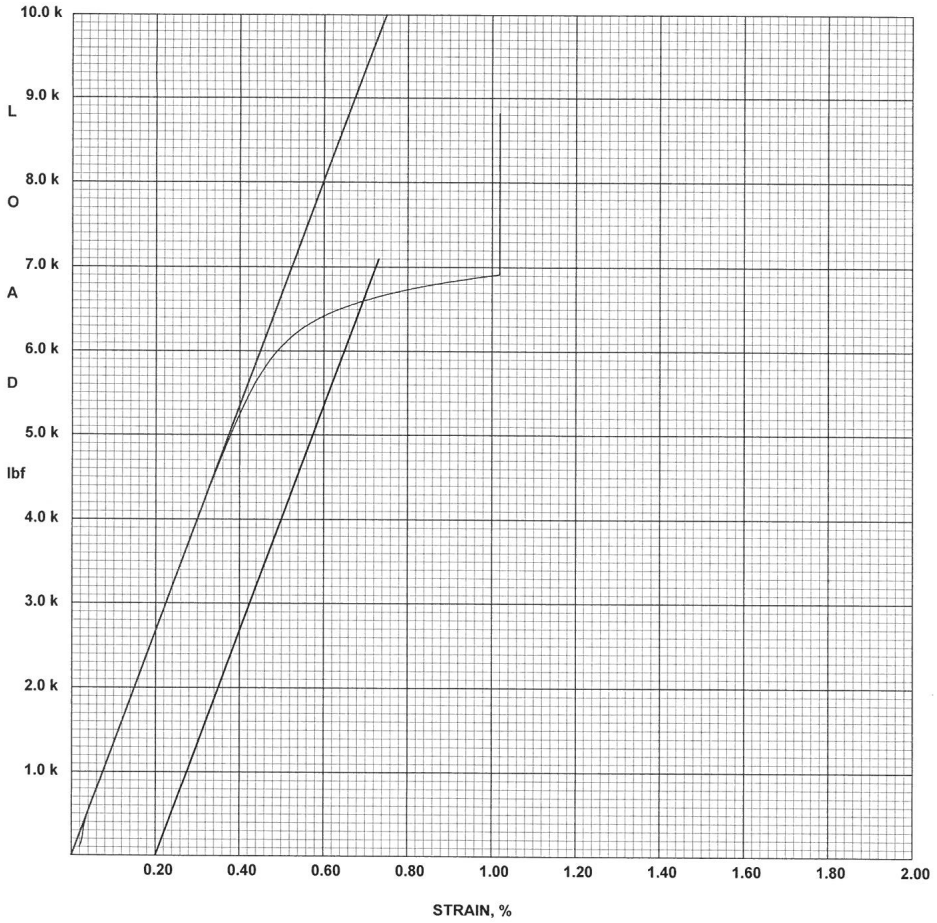

Allvac
2020 Ashcraft Avenue
Monroe, NC 28110

.005 in/in/min, .05 in/min (1.4 Red.Length)

Mill Order No.:	100074
Task ID:	200053958
Test Temperature:	ROOM
Dir/Loc:	I
Comments:	7180P
Extensometer:	142354 9
Strain Rate %:	.005
Crosshead Speed:	.05
Technician:	DBR2136
Box No.:	616
Initial Gage Length, in:	0.998
Reduced Section,in:	1.39
Initial Diameter, in:	0.2521
Ultimate, lbf:	8820
.2% Yield, lbf:	6596.9
Final Gage Length, in:	1.2845
Final Diameter, in:	0.1985
Ultimate, ksi:	176.7
.2% Yield, ksi:	132.16
EL, %:	28.7
RA, %:	38
Modulus, Mpsi:	26.8
Fail Loc:	Center Area
Frac Desc:	Ductile
Pass/Fail:	A

Sep 12, 2013 9:26:40 AM
SN: 203673-R3 V7.02.08

Figure 80: Tensile test data received from ATI

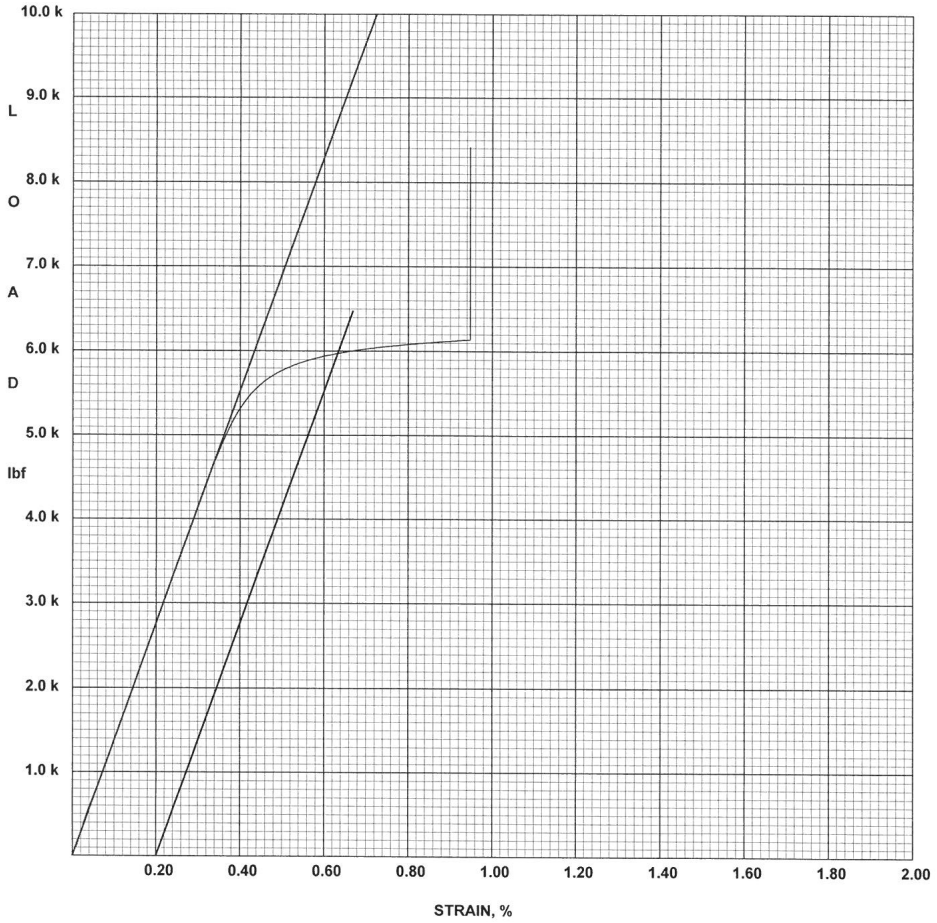

Allvac
2020 Ashcraft Avenue
Monroe, NC 28110

.005 in/in/min, .05 in/min (1.4 Red.Length)

Mill Order No.:	100074
Task ID:	200053964
Test Temperature:	ROOM
Dir/Loc:	L
Comments:	56LH-1 A
Extensometer:	142354 9
Strain Rate %:	.005
Crosshead Speed:	.05
Technician:	DBR2136
Box No.:	616
Initial Gage Length, in:	0.998
Reduced Section,in:	1.40
Initial Diameter, in:	0.2524
Ultimate, lbf:	8412.3
.2% Yield, lbf:	5973.3
Final Gage Length, in:	1.4395
Final Diameter, in:	0.164
Ultimate, ksi:	168.13
.2% Yield, ksi:	119.38
EL, %:	44.2
RA, %:	57.8
Modulus, Mpsi:	27.6
Fail Loc:	Center Area
Frac Desc:	Ductile
Pass/Fail:	A

Sep 12, 2013 10:30:02 AM
SN: 203673-R3 V7.02.08

Figure 81: Tensile test data received from ATI

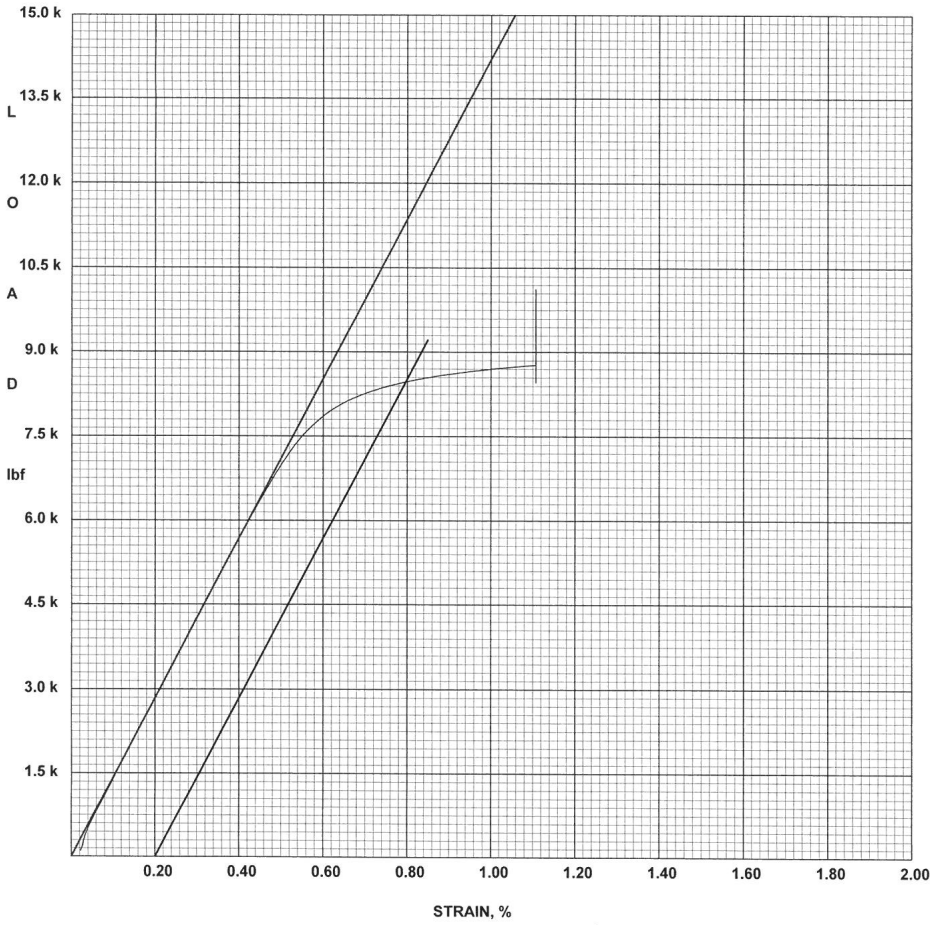

Allvac
2020 Ashcraft Avenue
Monroe, NC 28110

.005 in/in/min, .05 in/min (1.4 Red.Length)

Mill Order No.:	100074
Task ID:	200053965
Test Temperature:	ROOM
Dir/Loc:	L
Comments:	56LH-1 C
Extensometer:	142354 9
Strain Rate %:	.005
Crosshead Speed:	.05
Technician:	DBR2136
Box No.:	616
Initial Gage Length, in:	0.998
Reduced Section,in:	1.397
Initial Diameter, in:	0.2528
Ultimate, lbf:	10122.1
.2% Yield, lbf:	8467.3
Final Gage Length, in:	1.298
Final Diameter, in:	0.1785
Ultimate, ksi:	201.7
.2% Yield, ksi:	168.69
EL, %:	30.1
RA, %:	50.1
Modulus, Mpsi:	28.3
Fail Loc:	Center Area
Frac Desc:	Ductile
Pass/Fail:	A

Sep 12, 2013 11:00:41 AM
SN: 203673-R3 V7.02.08

Figure 82: Tensile test data received from ATI

Figure 83: Tensile test data received from ATI

Figure 84: Tensile test data received from ATI

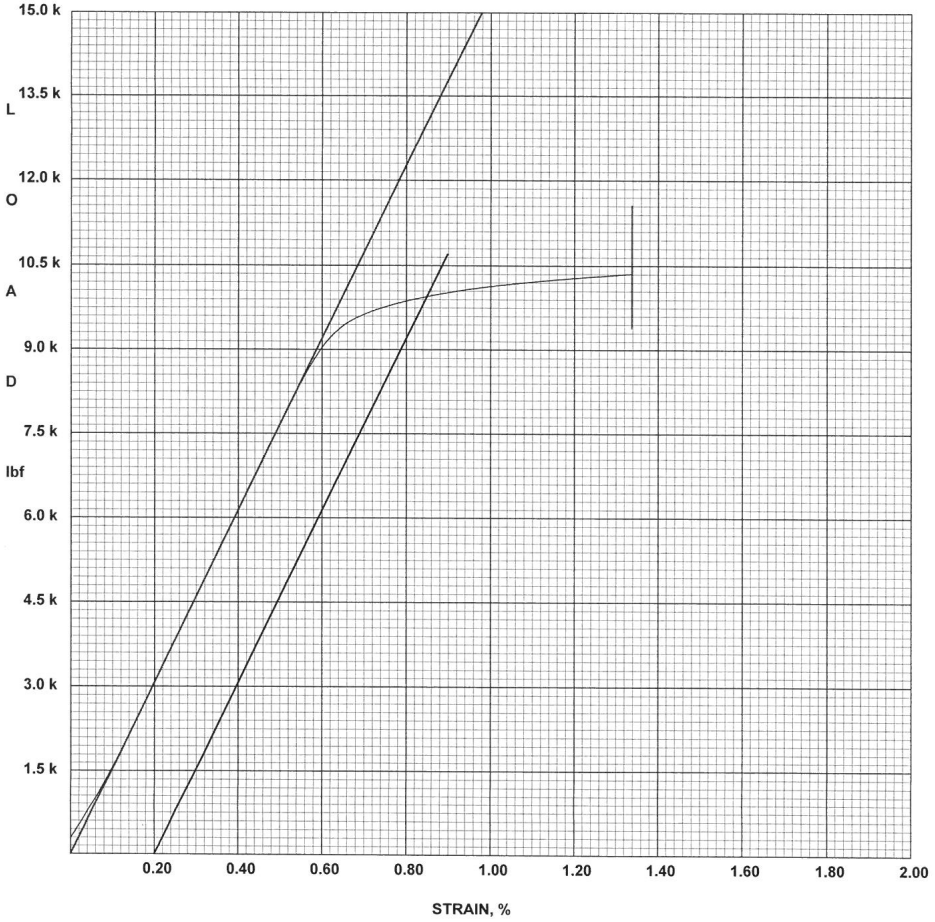

Allvac
2020 Ashcraft Avenue
Monroe, NC 28110

.005 in/in/min, .05 in/min (1.4 Red.Length)

Mill Order No.:	100074
Task ID:	200053960
Test Temperature:	ROOM
Dir/Loc:	L
Comments:	P3A01 1800
Extensometer:	142354 9
Strain Rate %:	.005
Crosshead Speed:	.05
Technician:	DBR2136
Box No.:	616
Initial Gage Length, in:	0.998
Reduced Section,in:	1.399
Initial Diameter, in:	0.2538
Ultimate, lbf:	11562.7
.2% Yield, lbf:	9950.9
Final Gage Length, in:	1.262
Final Diameter, in:	0.184
Ultimate, ksi:	228.6
.2% Yield, ksi:	196.69
EL, %:	26.5
RA, %:	47.4
Modulus, Mpsi:	30.3
Fail Loc:	Center Area
Frac Desc:	Ductile
Pass/Fail:	A

Sep 12, 2013 9:46:16 AM
SN: 203673-R3 V7.02.08

Figure 85: Tensile test data received from ATI